

Particle Image Velocimetry applied to waves with Surface Active Films



John Pullen

A thesis submitted in fulfilment of the requirements

for the degree of Doctor of Philosophy

to the

University of Edinburgh

1998

Abstract

The technique of Digital Particle Image Velocimetry (DPIV) and the related technique of Particle Tracking Velocimetry (PTV) are described.

These techniques were extended and applied by the author to the study of surface active chemical films on the mechanics of capillary-gravity waves.

The two custom-made facilities for these studies are described along with specialised image processing software developed by the author.

Finally, results from a series of experiments are presented which detail the damping of wind waves by surface active films, measurements of wind induced surface drift and the alteration of surface particle trajectories. Results from all three experiments were compared with current theoretical predictions.

Acknowledgements

I would like to thank Mum and Dad, Mike, Rosie, Fergus, Kirsten and Karen for their constant support and encouragement.

None of the work would have been possible without the assistance and endless pots of money supplied by my supervisor, Clive Greated. Thank you also to Frank Morris for fixing everything when I broke it and Andy Downie for making the things for me to break.

I am also indebted to Stevie, for just being "Stevie", Peter for keeping me fit, Brian for dragging me half way round the world, Tim for endless sources of technical knowledge and office humour, Paul Mitchell for keeping the "Most Sarcastic Person" title off my shoulders and the odd computing tip, John Scott and Al Arnott for keeping Bic Red Pens in business, all my friends at the Fimbush Point Field Centre for their constant distraction and many, many others...

And finally, thank you to The Department of Physics and Astronomy, EPSRC and The Defence Research Agency for funding the whole affair.

Declaration

I declare that this thesis was composed by myself and that the work contained therein is my own, except where explicitly stated otherwise in the text.

Table of Contents

Abstract	i
Acknowledgements	ii
Declaration	iii
List of Figures	viii
Chapter 1 Introduction	1
1.1 Subject Background	1
1.2 Chemistry of surface active films	4
1.3 General Theory of Wave Motion	5
1.4 Growth of Capillary-Gravity Waves	6
1.5 Damping of capillary-gravity waves by films	7
1.5.1 Prevention of waves forming	7
1.5.2 Damping of existing waves	8
1.6 Digital Particle Image Velocimetry (DPIV)	15
Chapter 2 Experimental Facilities	16
2.1 Summary	16
2.2 The Wind-wave flume	16
2.2.1 Introduction	16

2.2.2	Design Criteria	17
2.2.3	Aerodynamic Considerations	20
2.2.4	Experimental Arrangements in the Wind-Wave Flume	23
2.3	Mini Tank	31
2.3.1	Introduction	31
2.3.2	Weir Tank	33
Chapter 3 Experimental Techniques		34
3.1	Summary	34
3.2	Flow Visualisation	34
3.3	Particle Image Velocimetry (PIV)	36
3.3.1	Introduction	36
3.3.2	Experimental Setup	36
3.3.3	PIV Development	37
3.3.4	Developments in Seeding and Illumination	37
3.3.5	Image Capture Development	42
3.3.6	Post Processing Development	45
3.3.7	Digital Particle Image Velocimetry (DPIV)	51
3.3.8	Sources of Errors in DPIV	51
3.3.9	Optimisation of PIV Parameters	59
3.3.10	Future of PIV Development	59
3.3.11	DPIV applied to surface film studies	60
3.4	Particle Tracking Velocimetry (PTV)	62
3.4.1	Introduction	62
3.4.2	Actual Implementation of PTV software	64
3.4.3	Future of PTV Development	67
3.4.4	PTV applied to surface film studies	69

Chapter 4 Image Processing	71
4.1 Summary	71
4.2 Geometric Correction	71
4.3 Production of Simulated Images	73
4.4 Ellipse Parameter Extraction by Pseudo Randomised Hough Transform (RHT)	73
4.4.1 Introduction	73
4.4.2 Images with more than one line	75
4.4.3 RHT applied to ellipse detection	77
4.4.4 Actual Implementation	79
4.4.5 Errors in ellipse calculation	82
4.4.6 Description of title	90
Chapter 5 Results 1 - Effect of Surface Films on Wind Generated Waves	93
5.1 Summary	93
5.2 Introduction	93
5.3 General Characteristics of Laboratory Wind Generated Waves . .	94
5.3.1 DPIV Measurements	95
5.3.2 Wave Gauge Measurements	102
5.4 Damping of Wind Generated Waves by Hand Soap	105
5.4.1 DPIV investigation of wind wave damping	105
5.4.2 Wave Gauge investigation of wind wave damping	110
5.5 Effect of surface films in the surf zone	115
Chapter 6 Results 2 - Effect of Surface Films on Small Paddle Generated Waves	118

6.1	Summary	118
6.2	DPIV Measurements of wave damping	118
6.3	Surface particle trajectory measurements	122
6.4	Effect of wave motion on surface tension	128
Chapter 7 Conclusions		132
7.1	Summary of Main Results	132
7.2	Suggestions for Future Work	133
Appendix A Chemical Constituents of Chemical Films		136
Appendix B Papers Published & Conferences Attended		137
Bibliography		139

List of Figures

1.1	Synthetic Aperture Radar (SAR) image of sea surface	2
1.2	Sunlint image of sea surface	3
1.3	Chemistry of surface active films	4
1.4	Wave velocity as a function of wavelength	6
1.5	Longitudinal wave motion	9
1.6	Damping ratio as a function of wavelength	12
1.7	Surface profile and surface particle trajectories for various values of beta - waves traveling left to right	13
1.8	Alteration to horizontal velocity component by film	14
2.1	Schematic of wind wave facility	18
2.2	Photograph of wind wave facility	21
2.3	Schematic of Pitot-Static Tube	24
2.4	Wind Profiles	25
2.5	Non-intrusive laser slopometer	28
2.6	Conductive wavegauge	28
2.7	Linear response of wave gauges to immersion depth	29
2.8	Spectral analysis of wind waves	30
2.9	Wave gauges operating correctly	30
2.10	Crosscorrelation of Two Wave Gauges	32

2.11 Schematic of Mini Tank Facility	33
2.12 Schematic of Mini Tank Facility with weir	33
3.1 Basic flow visualisation setup	37
3.2 Response of particle to oscillating flow	40
3.3 Scanning beam illumination system	41
3.4 2-CCD array system	44
3.5 Simplified multiply exposed single frame image	46
3.6 Example of 2D Autocorrelation function	47
3.7 Double exposure of each particle	50
3.8 Analysis by Autocorrelation - No post processing applied	50
3.9 Simplified single exposed multiple frame image	50
3.10 Image from 1st Exposure	52
3.11 Image from 2nd Exposure	52
3.12 Example of 2D Cross Correlation Function	52
3.13 Analysis of Image by Crosscorrelation - No post processing applied	52
3.14 Ideal and real displacement functions	55
3.15 Actual displacement functions modified by \mathcal{F}	56
3.16 Effect of different interrogation window sizes on the function, \mathcal{F} . Cross in circle denotes crosscorrelation function	57
3.17 Example of DPIV analysis of wind generated waves	61
3.18 Possible ambiguity in velocity derived from PIV images	63
3.19 Typical Multiple Exposure Image - Single Camera	64
3.20 Exact location of particle	65
3.21 Calculated velocity vectors	66
3.22 Simulated Poiseuille flow with calculated vectors	67
3.23 Comparison of theoretical and calculated velocities	67

4.1	Simulated Image	73
4.2	Line in image space	74
4.3	Point (x1,y1) mapped to line in transform space	74
4.4	Points (x1,y1) and (x2,y2) mapped to lines in transform space . .	74
4.5	Input to Hough Transform	75
4.6	Standard Hough Transform	76
4.7	Randomised Hough Transform	77
4.8	Centre lies on line $M_{AB}I_{AB}$	78
4.9	Centre lies at intersection of $M_{AB}I_{AB}$ & $M_{BC}I_{BC}$	78
4.10	Ellipse is actually discrete points	80
4.11	Triplet set with fitted quadratic	81
4.12	Histogram of pre-filtered ellipse parameters	83
4.13	Ellipse fitted to points	84
4.14	Error in calculated tangent gradient. Legend indicates angular separation between points (degrees)	85
4.15	Calculated tangent gradient	86
4.16	Expected tangent gradient	87
4.17	x-coordinates identical at high tangent gradient	87
4.18	Comparison of Calculated centre coordinates with actual coordi- nates (- - -)	88
4.19	Percentage error in calculated coordinates	89
4.20	Comparison of calculated ellipse parameters with actual parame- ters (- - -)	91
4.21	Percentage error in ellipse parameters	92
5.1	Location of wave gauges and PIV Measurement Zones	94
5.2	Typical Vector and Vorticity Map - 3.5m	97

5.3	Typical Vector and Vorticity Map - 4m	98
5.4	Typical Vector and Vorticity Map - 5m	99
5.5	Typical Vector and Vorticity Map - 6m	100
5.6	RMS Vertical Velocity with exponential fit (- - -). Wind Speed 5.36ms ⁻¹	102
5.7	RMS Horizontal Velocity with exponential fit (- - -). Wind Speed 5.36ms ⁻¹	103
5.8	Spectral components before the film is applied. Wind Speed 5.36ms ⁻¹	104
5.9	Comparison of Phillips Theory (- - -) and experimental results . .	104
5.10	RMS V_x - 3.5m	107
5.11	RMS V_y - 3.5m	107
5.12	RMS V_x - 4m	107
5.13	RMS V_y - 4m	107
5.14	RMS V_x - 5m	108
5.15	RMS V_y - 5m	108
5.16	RMS V_x - 6m	108
5.17	RMS V_y - 6m	108
5.18	8s after film added	109
5.19	10s after film added	109
5.20	13s after film added	109
5.21	14s after film added	109
5.22	15s after film added	109
5.23	4 Minute record of wave amplitude at Gauge 1	110
5.24	4 Minute record of wave amplitude at Gauge 2	111
5.25	4 Minute record of wave amplitude at Gauge 3	111
5.26	4 Minute record of wave amplitude at Gauge 4	112

5.27	Damping of Maximum Wave Amplitude	113
5.28	Growth of Maximum Wave Amplitude	114
5.29	Peak spectral component as film enters measurement zones	116
5.30	Peak spectral component as film leaves measurement zones	116
6.1	Shear Profile	120
6.2	Typical PIV Image	121
6.3	Typical Velocity Vector Map	121
6.4	Damping of Horizontal Velocity by Film	122
6.5	Damping of Vertical Velocity by Film	123
6.6	Surface and Sub-Surface Particle Trajectories - Hand Soap	124
6.7	Particles often do not return to their original starting point	127
6.8	Clean Water - clockwise rotation	128
6.9	Soap - clockwise rotation	128
6.10	Light Oil	128
6.11	Cling film	128
6.12	Surface and Sub-Surface Particle Trajectories - Inextensible Film	129
6.13	Maximum Horizontal Displacement	130
6.14	Oil drop at wave crest	130
6.15	Oil drop at wave trough	131
6.16	Change in oil drop diameter	131

Chapter 1

Introduction

1.1 Subject Background

The calming effect of films of oil on the surface of the sea has been known about since the days of Aristotle and Plutarch, see Scott's historical bibliography [79]. Indeed, it was the experience of early seafarers that led to the the common phrase "*To pour oil on troubled waters*".

Since being brought to the attention of the scientific community in 1774 by Benjamin Franklin's "*teaspoon of oil on Clapham Pond*" experiment [21], his basic theory has been developed and extended by several researchers. The most notable of these were Rayleigh (1890) [75], Lamb (1895) [49] and Levich (1940) [55], with the current theory being established by Dorrestein in 1951 [74]. This theoretical work was backed up by the experiments of Davies and Vose [10]. Since then only minor modifications to the basic theory have been presented, the most important being Lucassen-Reynders and Lucassen (1969) [59] who introduced concept of the longitudinal surface wave. A full account of the development of the theory of wave damping by films can be found in Scott [78].

Recently, numerous laboratory [36, 77] and field studies [68, 83, 18] have shown that even monolayers of certain oils and detergents, so-called surface-active materials, on the surface of water can have a significant effect on the initiation

and propagation of surface waves.

The general result of these surface films is to increase damping and prevent wave formation. The practical significance of this effect is that, in the open ocean, films of surface active material, which are formed naturally due to oceanic and biological processes and supplemented in coastal regions by anthropogenic contamination, can result in an alteration to the centimetre and metre scale sea surface roughness.

Active sea-surface remote sensing techniques such as Synthetic Aperture Radar (SAR) rely on the amount of microwave backscatter from waves at Bragg wavelengths (around 3-30cm). Thus an understanding of any physical process which effects such waves is essential to the correct interpretation of these images. Figure 1.1¹ is an example of an SAR image of the German coast showing clearly coastal contamination in the acquired image.

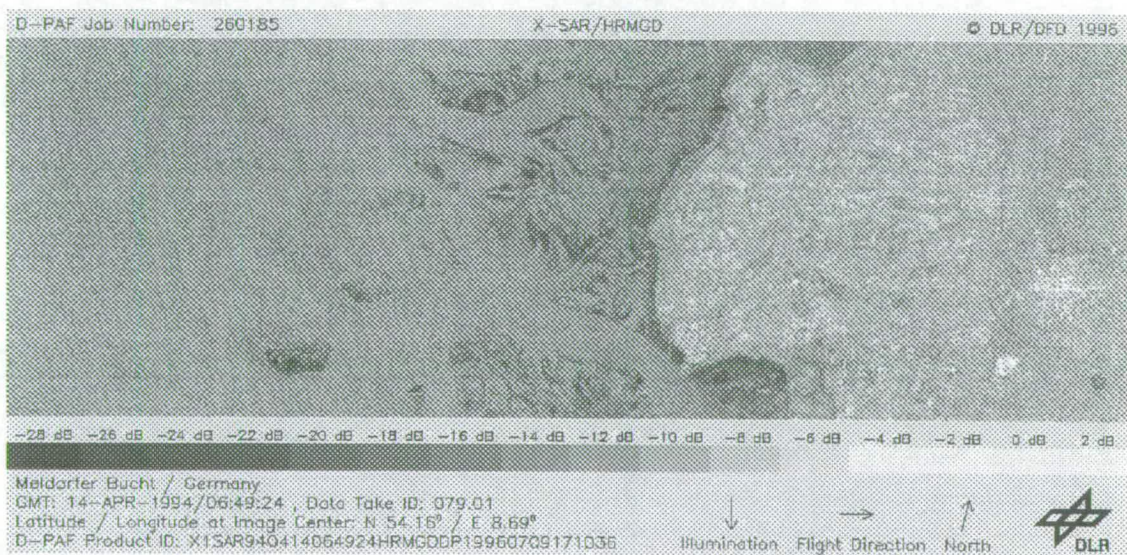


Figure 1.1: Synthetic Aperture Radar (SAR) image of sea surface

Similarly, figure 1.2², a sunglint image of the sea surface taken by the Space

¹Courtesy DLR, Germany

²Courtesy NASA, Lyndon B. Johnson Space Centre, Houston

Shuttle, clearly shows the presence of such slicks. With this passive method of imaging the sun's reflection is normally a disk, the diameter of which increases with surface roughness.³ Within the disk a brighter image indicates a smooth surface. Outwith the disk the brighter areas of the image relate to rough patches (such as the ship's wake). Thus the lower slick covered region indicates an area of relative calm. Additionally, the fine structure of the slick indicates how this feature can also be used to infer details relating to surface motions.



Figure 1.2: Sunlint image of sea surface

Thus a wealth of information relating to ocean dynamics, wind speed, air-sea transfer of gases, pollution monitoring and control and observations of biological activity are available from correctly interpreted images. As previously stated however, in order to achieve this it is necessary to have a proper understanding of the effect of surface active contamination on the basic mechanics of wind

³If the surface was (optically) flat, the diameter of the reflection would be the same size as the specular image of the sun.

generated waves.

Furthermore, in order to produce accurate models of movement and spreading of oil and chemicals spills at sea, such as EUROSPILL [17], it is essential that they are based on the actual physical mechanics of film covered surfaces.

1.2 Chemistry of surface active films

Chemicals which reduce surface tension are generally termed **Surface Active**. These naturally occurring and man-made chemicals generally contain a hydrophilic group which is adsorbed at the water surface and a hydrophobic group which orients itself away from the surface. O-H interaction can also lead to a partial ordering of the sub-surface water molecules as shown in figure 1.3⁴.

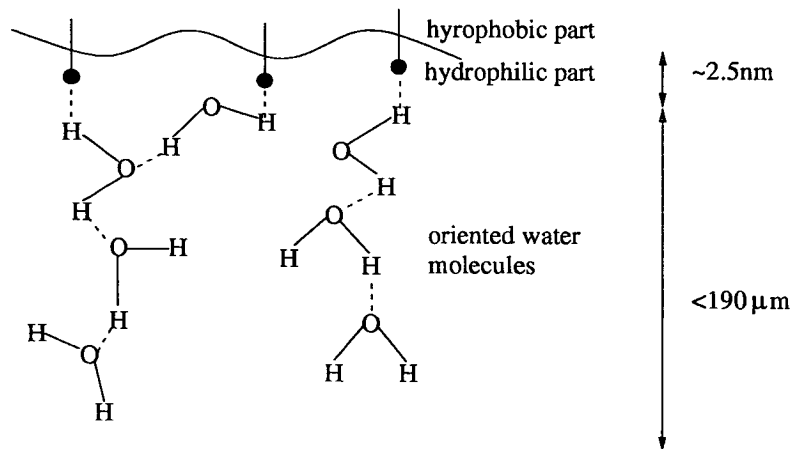


Figure 1.3: Chemistry of surface active films

Several studies have been performed to characterise the chemistry of the top microlayer of the sea surface to gain an insight into naturally occurring surface active material [56]. According to Huhnerfuss [38], surface active materials used for field and laboratory studies should possess the following properties:

- Liquid - so they spread easily and in particular a fluid mono-molecular film

⁴From Huhnerfuss[38]

to enable rapid spontaneous spreading.

- Non-volatile - to reduce evaporation losses
- Non-toxic

Generally for field studies it is desirable to have films which have low water solubility. This allows several hours of data collection before the effect of the film begins to wear off. However, for these studies it was desirable for the films to have high water solubility in order that many experimental runs could be performed without the need to constantly clean the wave tank.

1.3 General Theory of Wave Motion

The motion of waves on a free surface with no film is governed by the restoring forces of gravity and surface tension. The orbital frequency ω of such waves is given by the first-order dispersion relation [49];

$$\omega^2 = \left(gk + \frac{\sigma k^3}{\rho} \right) \tanh kh , \quad (1.1)$$

where g is the acceleration due to gravity, k the wavenumber ($2\pi / \text{wavelength}$), σ the surface tension, ρ the water density and h the water depth. This relationship has been tested by Scott [80] in the 25-250mm range and found to be accurate.

Assuming deep water (such that $\tanh kh \rightarrow 1$), a plot of phase velocity, V ($= \omega/k$), figure 1.4, indicates the existence of a minimum phase velocity of around 0.23ms^{-1} . Waves to the left of the dotted line (wavelength approx. 17mm) are commonly called *capillary waves*. As can be deduced from equation 1.1, surface tension is the predominant restoring force, the effect of which steadily decreases as

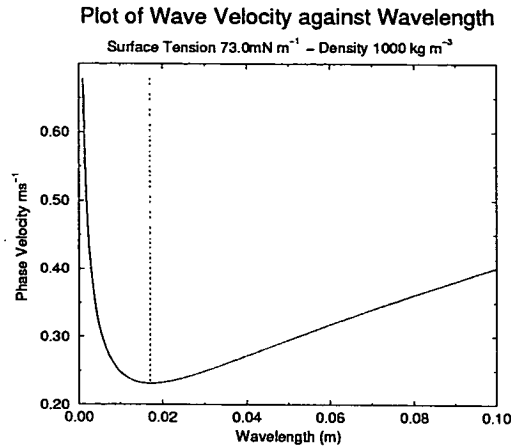


Figure 1.4: Wave velocity as a function of wavelength

wavelength increases until the waves are essentially purely *gravity waves*. Waves in the cm region, where both forces play a part are often named *capillary-gravity waves*. These waves are of similar wavelength to that used in microwave remote sensing equipment and hence are the only waves considered in these studies.

1.4 Growth of Capillary-Gravity Waves

To fully understand wave damping it is essential that we have a basic understanding of the growth mechanisms of capillary-gravity waves and in particular short, wind-induced waves.

When wind blows on an initially flat water surface, the resulting unstable shear-flow generates small ripples which propagate downwind.

Van Gastel *et. al* [89] in their quasi-analytical model found the minimum wind speed (frictional) capable of generating waves to be 0.05ms^{-1} . Kahma and Donelan [41] found in their laboratory experiments that a centre-line wind velocity of $1.6 - 3.3\text{ms}^{-1}$ was necessary to generate perceptible waves. They also found that this *critical wind velocity* increased as the water temperature decreased.

The interaction of these ripples with each other and the continued extraction

of energy from the wind results in growth of amplitude and wavelength until the waves reach a size such that new ripples are observed on the backs of these longer waves. It is generally accepted [14] that this process continues until the phase velocity of the longest waves is equal to the wind speed.

1.5 Damping of capillary-gravity waves by films

Surface films appear to have two obvious effects on the mechanics of capillary-gravity waves;

- Prevent waves forming (in the case of wind generated waves)
- Damp existing waves

Although as Dorrestein [74] pointed out, these are different manifestations of the same phenomenon, for the purposes of the theory described here and the results presented in later chapters, we shall deal with them separately.

1.5.1 Prevention of waves forming

According to Gottifredi and Jameson [22], the film acts to stabilise the water surface by increasing the critical wind speed (by up to a factor of 10 depending on the film). Thus at relatively low wind speeds, ripple growth is significantly reduced and can result in no waves being generated at all. This was verified by Scott [77] who found no evidence of a critical wind velocity on a pure surface but a substantial reduction in wind wave growth (at low wind speeds) on a contaminated surface.

Creamer and Wright [9] extended this idea with their theory that all wavelengths are associated with a particular growth rate. The effect of a surface film is to alter these growth rates such that the only wavelengths with significant growth rates are not physically present.

Substance	Surface Tension mNm^{-1}
Water	72.8
Oleyl alcohol	32
Methyl palmitate	19
Sorbitan monooleate	41

Table 1.1: Surface Tension of various monolayers

A consequence of suppressed ripple growth is the reduction in energy transfer from the wind to the waves due to the aerodynamically smoother surface. It is this feature that lead historical mariners to subscribe to the theory of *wave oiling*, whereby olive oil or fish oil was poured on the sea surface in the hope that potentially lethal breaking waves would be inhibited - hence the phrase: *To pour oil on troubled waters*.

1.5.2 Damping of existing waves

Any surface active film will act to reduce the surface tension[81], table 1.1⁵, and so from equation 1.1 it would seem that the only effect would be to reduce the propagation speed of small waves and have little or no effect on waves of longer wavelength. While, to some extent, this is true, the observed effects of increased wave damping and the change in surface particle trajectories must therefore be due to some other mechanism.

Increased wave damping

For deep water waves, most of the energy dissipation is due to the effect of viscosity within the wave field[58]. A clean surface is free to expand and contract with the passing of the waves. Strong velocity gradients do not occur and little energy is dissipated. Surface contamination inhibits the expansion and contraction of the surface, resulting in strong velocity gradients and consequently greater

⁵Taken from Lange and Huhnerfuss [51]

energy dissipation.

A film on the surface will move in an attempt to make the surface tension equal over the entire covered area. Waves propagating on the surface will tend to compress and extend the surface. Evidence of this can be found in chapter 6 and the experiments of Huhnerfuss [36]. Thus, as the waves propagate they generate a local surface tension gradient, or elasticity, which creates a longitudinal surface flow, figure 1.5, which in turn will oppose the original wave motion.

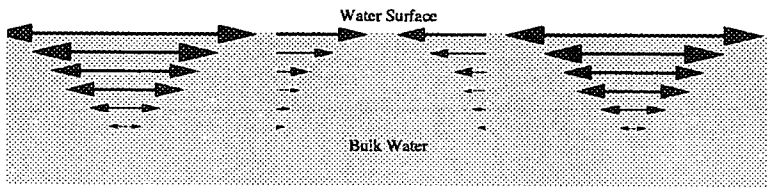


Figure 1.5: Longitudinal wave motion

Lucassen [58] defined the *surface dilatational elasticity*, ϵ , as the change of surface tension σ resulting from a change in surface area, A .

$$\epsilon = \frac{\delta\sigma}{\delta(\ln A)} \quad (1.2)$$

Thus the dilatational elasticity ranges from zero (for a clean surface) to infinity (for a completely inextensible surface). Naturally occurring surface contamination can give rise to dilatational elasticity values as high as $200mNm^{-1}$, although $50mNm^{-1}$ would be more typical [81]. This dilatational elasticity, a feature of all surface active films, is argued by Lucassen-Reynders and Lucassen [59], Scott [82] and others to be the most important parameter responsible for the observed effects to capillary-gravity waves. This idea was verified by Huhnerfuss [36] who obtained experimental evidence that surface tension gradients are indeed induced in monomers by propagating waves.

Lamb [49] defined the damping rate, γ such that

$$a = a_0 e^{-\gamma t} \quad (1.3)$$

where t is the time taken for the amplitude to drop from a_0 to a .

Lamb [49] also calculated γ for the two extreme cases; a clean surface and one covered in an inextensible film.

$$\gamma_{\text{clean}} = 2\nu k^2 \quad (1.4)$$

$$\gamma_{\text{inextensible}} = \left(\frac{\nu\omega k^2}{8}\right)^{\frac{1}{2}} \quad (1.5)$$

where ν is the kinematic viscosity of water. This theory was verified during the experimental work of Davis and Vose [10], who found that damping did increase in the presence of surface films.

Dorrestein [74] adapted the classical hydrodynamic equations to include a term relating to the dilatational elasticity of the surface film. This simple version of the theory neglects any influence of film viscosity, assuming that energy dissipation in the viscous shear layer is much greater than in the monolayer.

Building on this work, the damping rate, γ was re-expressed by Dysthe *et al.* [16] as:

$$\gamma = \frac{(\nu k^2 \frac{\omega}{2})^{\frac{1}{2}}}{(1 - \beta)^2 + 1} \quad (1.6)$$

with β a non dimensional number given by:

$$\beta = (2\nu)^{\frac{1}{2}} \rho C_s \omega^{\frac{3}{2}} k^{-2} \quad (1.7)$$

and C_s proportional to $1/\epsilon$.

Thus β ranges from ∞ in the absence of a film to zero for a completely inextensible film. If we set $\beta = 0$ in equation 1.6 we get back Lamb's original equation 1.5.

There are several features which can be noted from equations 1.6 and 1.7:

- Firstly, the maximum damping rate occurs at $\beta = 1$ and not for an inextensible film, $\beta = 0$. This maximum damping rate is about twice that associated with an inextensible film.
- Secondly, since maximum damping always occurs at $\beta = 1$, as the wavelength increases, so too must the value of ϵ required to bring it about.
- Thirdly, if we take the ratio of damping with a film present (equation 1.6) to damping with no film (equation 1.4), it actually increases with wavelength, contrary to expectation: 1m waves appear unaffected while capillary waves are completely damped.

These points can be observed in figure 1.6, taken from Lucassen [58]. The contours show the ratio of damping with film, γ , to damping with no film, γ_0 . As can be observed, for a fixed wavelength, the ratio passes through a maximum value, associated with a finite value of ϵ such that $\beta = 1$.

Also, a film possessing a surface dilatational elasticity of, say, $10mNm^{-1}$ will bring about maximum damping (about a ten-fold decrease) in a 2cm wave. However for a 20cm wave, it would take a film with $\epsilon > 100mNm^{-1}$ to bring about maximum damping (about a fifty-fold decrease). Therefore, for a fixed, typical value, of ϵ , most damping will occur in the small wavelength region, in line with observation.

A scheme for *in situ* measurements of the marine microlayer was proposed by Vesecky and Johnson [90] based on this relationship between damping rate

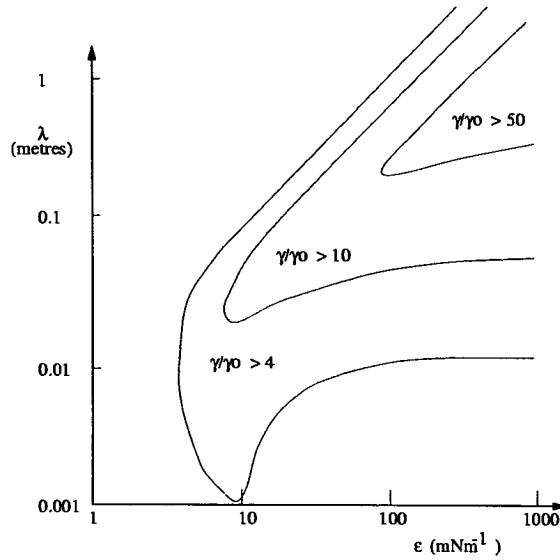


Figure 1.6: Damping ratio as a function of wavelength

and wavelength. From the damping rate of capillary-gravity waves of known wavelengths, they hoped to infer some basic properties (such as surface tension) of the surface film.

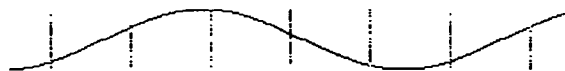
Alteration to Surface Particle Trajectories

As noted by Lucassen-Reynders and Lucassen [59] the expected circular trajectories of surface particles are modified to elliptical ones in the presence of a surface film. The effect of the elastic boundary at the surface alters the response of particles to horizontal motion, observed as a shift in phase angle (between the horizontal and vertical motion) from 90° . The reluctance of the film to compress and expand also gives rise to reduced horizontal motion.

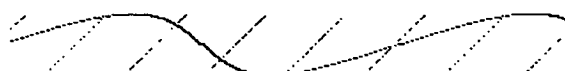
Figure 1.7⁶, shows the expected modification of surface particle trajectories for various values of β . As we shall see later in chapter 6 these are in very good agreement with the experimental results obtained in this study.

It is interesting to see that for the case where particle trajectories are elliptical

⁶Simulation software written by the author based on the work of Dysthe and Rabin [15]



(a) $\beta = 0$



(b) $\beta = 1$



(c) $\beta = 2$



(d) $\beta = 2000$

Figure 1.7: Surface profile and surface particle trajectories for various values of beta - waves traveling left to right

(as would be the case for most naturally occurring surface active chemicals), the surface profile is no longer symmetrical, with obvious implications for Remote Sensing.

Taking the case of an inextensible film, $\beta = 0$, Dorrestein [74] calculated the

change in horizontal velocity below the surface. Figure 1.8 shows that the velocity gradient is greatly increased which leads to the enhanced damping. However, as can be seen, and will also be demonstrated experimentally in these studies, the effect is restricted to a thin layer and circular orbits are preserved below the surface.

There is also an additional time dependence effect, noted by Huhnerfuss *et al.* [37] who found in a field study that damping got stronger many minutes after the slick had been spread. This, he attributed to increased order and interaction with sub-surface water molecules, as shown in figure 1.3, leading to increased damping.

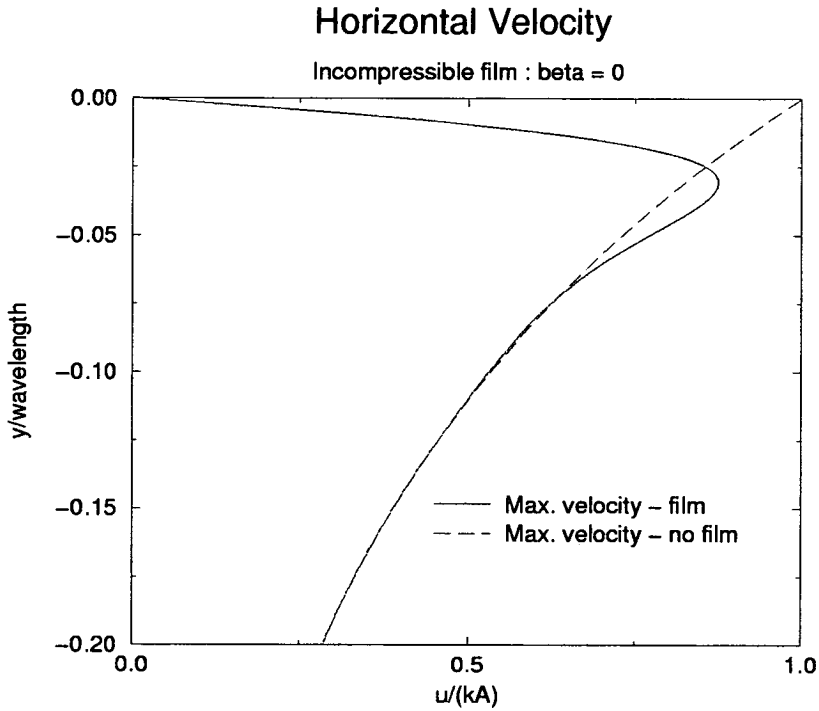


Figure 1.8: Alteration to horizontal velocity component by film

1.6 Digital Particle Image Velocimetry (DPIV)

Digital Particle Image Velocimetry is the modern counterpart of the well established flow visualisation technique of Particle Image Velocimetry (PIV).

The experimental set up and concept behind the technique will be described in later chapters. The results presented in the final chapters are quantitative experimental evidence of the theories presented above; damping of wind-waves and alteration to surface particle trajectories by surface active films. It was also possible to extend the technique to measure the effect of wind-induced surface drift and compare this with current theories.

Thus the following is not a work on Surface Chemistry nor a rigorous characterisation of wind induced waves but the extension of a new technique to display some fundamental theories.

Finally it should be noted that, similar to most laboratory studies, all experiments were performed in fresh water.

Chapter 2

Experimental Facilities

2.1 Summary

This chapter is concerned with the design and operation of the facilities used in the experimental programme. In order to observe and measure the damping effect that surface films have on wind-waves, it was necessary to construct a wind-wave facility that was capable of generating them. While attempting the second focus of these studies, that of measuring the change in orbital trajectories of surface particles, it was discovered that the flow in the wind-wave tank was too complex. A miniature wave flume was constructed to provide paddle generated waves of the same amplitude and size of those in the wind-wave tank, but without the accompanying turbulence and wind induced shear layer.

2.2 The Wind-wave flume

2.2.1 Introduction

Due to limitations of time and available laboratory space it was decided to construct a wind-tunnel above an existing wave-flume rather than build a complete customised facility. To ensure maximum fetch, the longest flume available within the group was chosen, known locally as *The Green Tank*. This facility is described in detail in the PhD thesis of Skyner [84] and only a short summary is given here.

The Green Tank is 9.8m in length, 0.4m in width, with a mean water depth of 0.75m. Situated at one end is a computer-controlled, hinged wave paddle. This simultaneously operates as an active wave absorber removing incoming reflections. At the other end, a passive foam absorber accommodates the final 2 metres of the flume.

The walls and base of the tank are formed from 1" thick glass panels. This allows maximum optical access which is especially important for the PIV system which is fully described in section 3.3.

The design of the tunnel was greatly limited by the shape of the wave flume and the restriction that it is in constant use for several different types of experiment.

2.2.2 Design Criteria

As noted by Bradshaw and Pankhurst [4], the simplest arrangement of wind tunnel is the *open-circuit* type. Air is taken from the room through the tunnel and returned to the room. To minimise construction time and take up minimal space in the laboratory, the design of the facility was based around this idea. Figure 2.1 displays the general layout of the wind-wave flume.

Air enters the tunnel through a contraction (area ratio 2:1) located above the wave paddle. This section is designed to force the air flow down onto the water surface. From here the air travels through the working section where all experimental readings are taken. It is shown later in section 2.2.4 that away from the walls, the mean air velocity in this region is uniform. Above the foam absorber, the tunnel expands to the width of the fan mounting. Thus, the tank operates in a *suck down* manner to minimise fan induced swirl.

The design was based around the recommendations of Bradshaw for "Simple Wind Tunnel Design" [3]. The exact design reasoning for each section of the wind

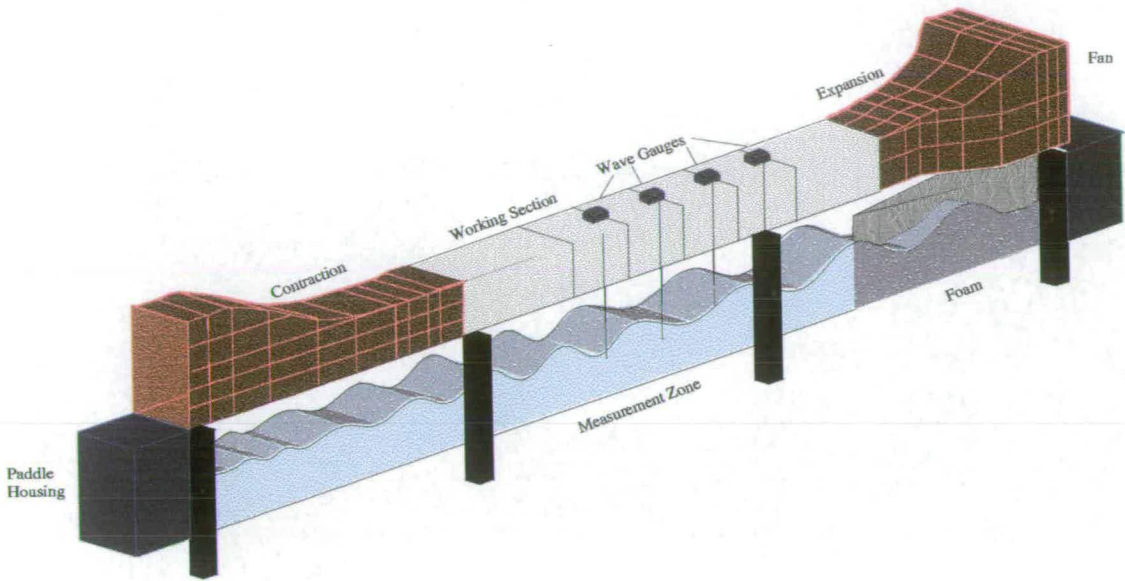


Figure 2.1: Schematic of wind wave facility

tunnel is given below:

The Working Section

The width of the working section was necessarily that of the flume below it. Although Bradshaw recommended a rectangular ratio of 1:1.5, a slightly greater height of 75cm above the still water level was chosen to minimise the effects of blockage when the wind was used in conjunction with large paddle generated waves, giving a ratio of $40:75 \simeq 1:2$.

The tank is used for several different experiments and as such it was necessary to fabricate the working section in several, lightweight sections to enable them to be easily removed. Five sections, each 1m long were constructed from polycarbonate sheeting attached to aluminium frames. The sections were bolted together and a thin strip of foam was used between each to minimise leakage.

Due to the nature of the tank, the working section is rectangular in cross section. Although corner fillets are generally used in aerodynamic wind tunnels it was felt that these would only add extra weight and complexity for little gain.

The Contraction

The contraction was required to intake air at as slow a speed as possible, to minimise initial losses, then to accelerate and force the air down onto the water surface. Thin reinforced plywood was used to form a natural curve from the width and height of the intake to that of the working section.

The maximum size (cross sectional area) of intake that could be accommodated in the lab was only twice that of the working section although ideally it should be much greater.

It was decided not to install honeycomb sections or gauze screens to reduce turbulence. There is a sudden step down from the top of the wave paddle to the water surface, downwind of where such screens would be located. The resulting separation would be responsible for most of the turbulence generation and there is little that can be done to reduce this.

The Expansion (Diffuser)

The expansion was also constructed from thin, reinforced plywood, taking a natural curve from the width and height of the working section, to that of the fan mount.

The Fan

To enable the wind generated waves to travel in the same direction as the paddle generated ones and due to the mechanics of the wave-maker, it was necessary to place the fan at the far end - operating in a sucking manner.

The fan has a variable speed controller to allow for the future option of integrating the wind speed with experiments in the tank, the wavemaker or some external apparatus. The exact specifications of the fan were selected with reference to basic aerodynamic considerations discussed in the following section.

Figure 2.2 is a photograph of the final facility.

2.2.3 Aerodynamic Considerations

Wind Speed

In order to exceed the *critical wind velocity* described in chapter 1 and from experience of a similar wind-wave facility at the Department of Ship Science at the University of Southampton, [64] a wind speed of approximately $6\text{m}\cdot\text{s}^{-1}$ is sufficient to generate waves several centimetres in amplitude over the available fetch. This velocity was similar to that used by Wang and Wu [91] in their experiments.

As the working section has a cross sectional area of 0.3m^2 the fan would need to be capable of delivering at least $2\text{m}^3\cdot\text{s}^{-1}$ through the working section.

Pressure Drop

Just as a moving object has to be capable of overcoming its associated frictional force, so too must the fan be capable of overcoming the friction of the air passing the walls of the tunnel, the *surface frictional drag* or *skin friction*.

This force is generally measured as a pressure drop in the tunnel and was calculated according to Pankhurst and Holder [69]. Only approximate calculations could be made due to the large number of *unmeasurable* influences from the wave flume itself. These include the effect of the wave paddle mechanics, the passive foam absorber and the fact that the intake and fan are both located very close to the walls of the laboratory.

Pressure drop due to the skin friction imposed by a solid boundary (*i.e.* the walls and the water surface) is given by:

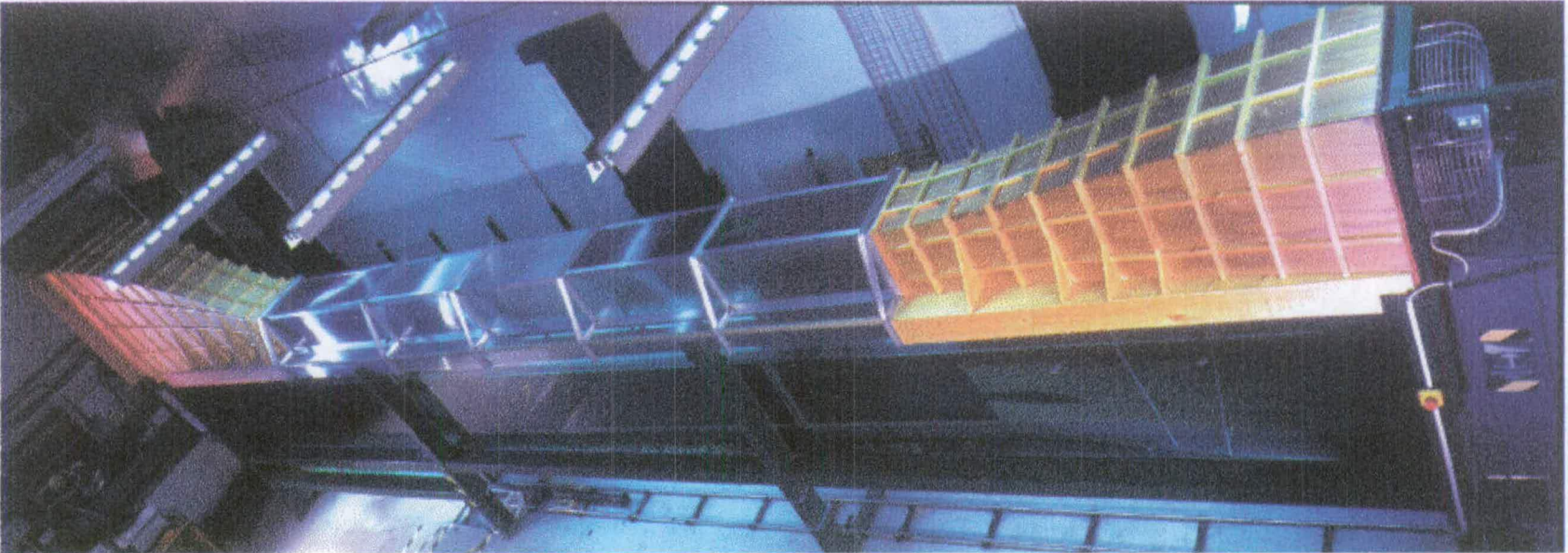


Figure 2.2: Photograph of wind wave facility

$$\Delta H = \int c_f \frac{1}{2} \rho U^2 \frac{L}{A} ds \quad (2.1)$$

where c_f is the coefficient of skin friction, ρ the density of air, U the wind speed, L the cross sectional perimeter at the air boundary, A the cross sectional area and ds being an element of length in the direction of the flow.

According to Houghton and Carruthers [34], for turbulent flow in a channel with smooth walls,

$$c_f = 0.0595 R^{-0.35} \quad (2.2)$$

$$R = \frac{ux}{\nu} \quad (2.3)$$

where R is the Reynolds number, calculated to be of the order of 1.6×10^5 from the expected wind velocity, U , characteristic length, x (in this case width) of the tank and ν the kinematic viscosity of air. For this value of Reynolds number and as demonstrated experimentally in the following section, this is within the turbulent regime and thus the use of the equation is valid.

Using the dimensions of the tunnel, there should be a pressure drop of at least 5Pa in the working section, and by a similar calculation, 3Pa and 2Pa in the contraction and expansion respectively. Loss of pressure due to the open end of the contraction can be calculated from:

$$\Delta H = \left(\frac{A_w}{A_e} \right)^2 \frac{1}{2} \rho U^2 \quad (2.4)$$

where A_w and A_e are the cross sectional areas of the working section and open end respectively. Taking our dimensions, we obtain a pressure loss of 16Pa due to the open end.

Thus, the total pressure loss in the tunnel is therefore estimated to be approximately 26Pa. This is, however, a minimum estimate due to the effects of the unmeasurable influences listed earlier.

Taking the above calculations and available budget, a 610mm diameter 5 bladed fan with a maximum operating speed of 940RPM was installed. This was quoted to deliver $2.6m^3s^{-1}$ of air against a 37.5Pa static pressure, with a resulting theoretical maximum wind speed of $8ms^{-1}$.

Ideally, it would be preferable to be able to obtain higher wind speeds such that waves were still created in the presence of a film (*i.e.* unable to be fully damped - although Dysthe [15] suggests that this is only for frictional velocities in excess of $25cms^{-1}$). However, this was the largest fan available that could be powered from a conventional 13A single phase supply. The installation of a three-phase supply to the tank was considered to be too expensive and time consuming.

2.2.4 Experimental Arrangements in the Wind-Wave Flume Wind Profile

To measure the wind profile within the tank, an ellipsoid-nosed pitot-static tube, figure 2.3, was traversed such that it remained parallel to the water surface and the sides of the tank.

The device is placed in the moving air stream with its open end, A, pointing directly upwind. Air flowing outwith the narrow boundary layer at B is taken to be travelling at a speed, v_B (although the no-slip conditions dictates that the velocity at B is zero). However, the static pressure in the stream must be transmitted without change through the boundary layer to B and it is that which we are measuring. At these low velocities, air entering the device at A, will be brought to rest and as such, a pressure difference, ΔP , will exist between the

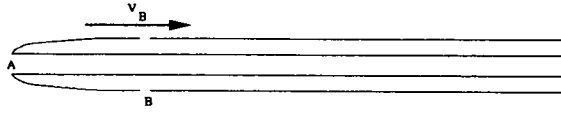


Figure 2.3: Schematic of Pitot-Static Tube

two points.

According to Houghton and Carruthers [34], for an incompressible flow, Bernoulli's equation states:

$$P_A + \frac{1}{2}\rho(0)^2 = P_B + \frac{1}{2}\rho(v_B)^2 \quad (2.5)$$

$$v_B = \sqrt{\frac{2\Delta P}{\rho}} \quad (2.6)$$

where P_A is the total pressure of the air stream, P_B is the static pressure and the quantity $\frac{1}{2}\rho(v_B)^2$ the dynamic pressure.

A digital manometer connected to the pitot-static tube displayed the pressure difference between the holes at A and B in mmH_2O . This is converted into Pascals by multiplying by g (taken to be $9.81ms^{-1}$).

Both horizontal and vertical profiles were taken at four locations in the tank. Generally, the mounting brackets for the wave gauges were used to fasten the pitot-static tube and as such, dictated their location. All the vertical profiles were obtained with the probe located along the centre line of the tank. Horizontal profiles were recorded with the probe located 40mm above the still water level. Sampling at each location for 1 minute produced the following profiles, figure 2.4.

The vertical profiles indicate that the mean wind speed is constant above the air-water interface. At such low wind velocities, the resolution of the digital manometer ($0.1mmH_2O$) gives a rather large error of $\pm 0.6ms^{-1}$ in each reading which explains why the moderate windspeed profiles appear *kinked*. However, it is worth noting that these readings were only taken to characterise the general

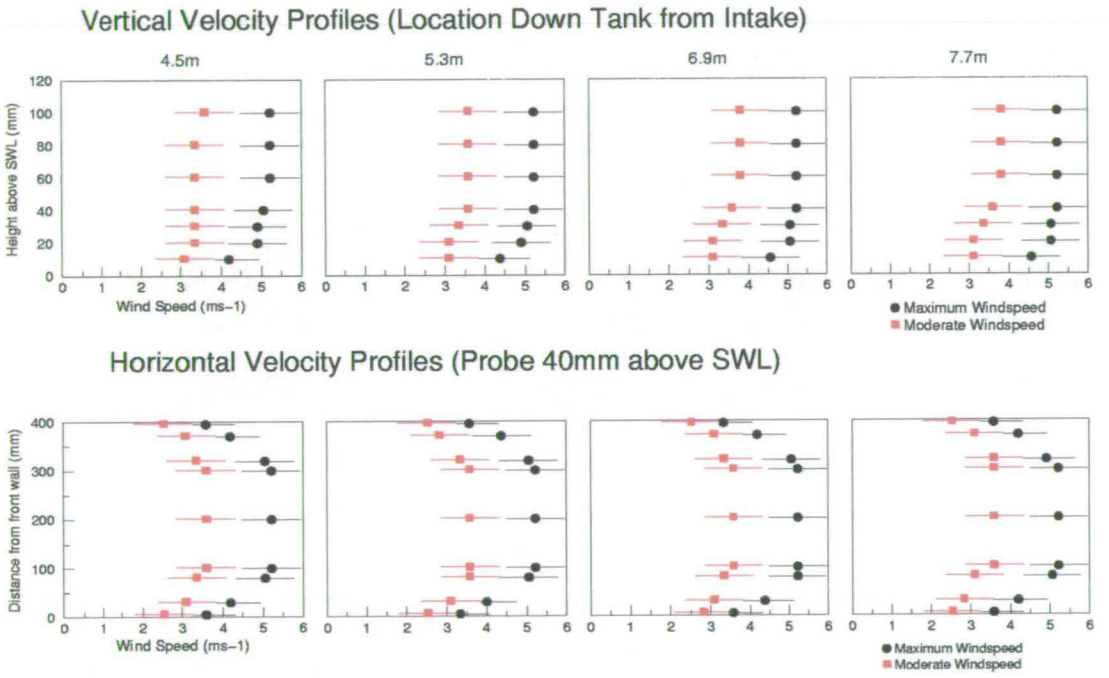


Figure 2.4: Wind Profiles

behaviour of the flow and to obtain an approximate wind velocity.

The horizontal profiles show a flattened parabolic shape, consistent with turbulent flow [88]. This indicates a region of constant mean wind velocity down the centre line of the tank. It was strongly desirable to have uniform flow in this area as this was the region where most of the wave gauge and PIV measurements were taken and any cross tank components can lead to erroneous results.

The maximum centreline windspeed recorded was approximately 5.5ms^{-1} which, although lower, is close to that of the original design. This lower value is not surprising given that the foam absorber, wave paddle and close proximity of both ends to the laboratory walls will have a significant and unavoidably detrimental effect on the maximum achievable wind velocity.

It was originally intended to obtain full field velocity information of the air flow over the water surface using the PIV technique. However, despite several attempts this was found to be extremely difficult. A fuller description of this experiment can be found in section 3.3.11.

Wave Gauges

Changes in the profile of the water surface and details regarding the alteration of spectral components within the wind generated waves are easier to obtain from wave gauge readings than from PIV measurements. This is a consequence of the fact that PIV measurements become highly erroneous close to the water surface. The wavy surface causes problems with the rectangular nature of the PIV analysis software and the highly reflective nature of the air-water interface gives rise to a very bright line, obliterating seeding particle images.

In order to accurately measure the amplitude and slope of the small amplitude, high frequency waves it was hoped to use non intrusive wave gauges.

Several such devices have been invented for specific field studies [54, 87, 57,

40, 48] although the author is not aware of any in day-to-day laboratory use. Lee's [54] device utilised Snell's law of diffraction to obtain the wave slope and height. A similar device was invented by the author, figure 2.5. A vertical, red laser beam is refracted by the water surface before passing through two green acetate sheets placed a short distance apart. The point of incidence with each sheet appears as a bright spot when captured by a CCD camera mounted directly above. The displacement of the two dots from the centre can be related to the slope and height of the water surface by simple geometry.

The system was evaluated by an undergraduate student [20], supervised by the author. The instrument proved that it would be a useful tool for such studies, once a number of improvements had been made. The most notable of these was the speed at which the CCD camera could capture images, store and process them. One possibility is the use of an *intelligent* camera coupled with a Digital Signal Processing (DSP) chip. If the camera itself could locate the spots, there would be no need to store them and this bottleneck would be illuminated.

However, this device was not the main focus of these studies and it was decided not to proceed with such improvements. The instrument is still an ongoing final-year undergraduate project.

In the end, the tank was fitted with 4 (intrusive) conductive wavegauges. These consist of 2 metal rods, 3mm in diameter, 40cm in length, separated by 2cm, as shown in figure 2.6. The output voltage is linearly proportional to their depth of immersion as seen in figure 2.7. A number of these gauges were in common use in the group and were capable of sampling the water surface at faster rate than the laser based device.

The sampling computer was capable of sampling each gauge at up to 500 000Hz, although in order to keep data volume to a manageable level and yet

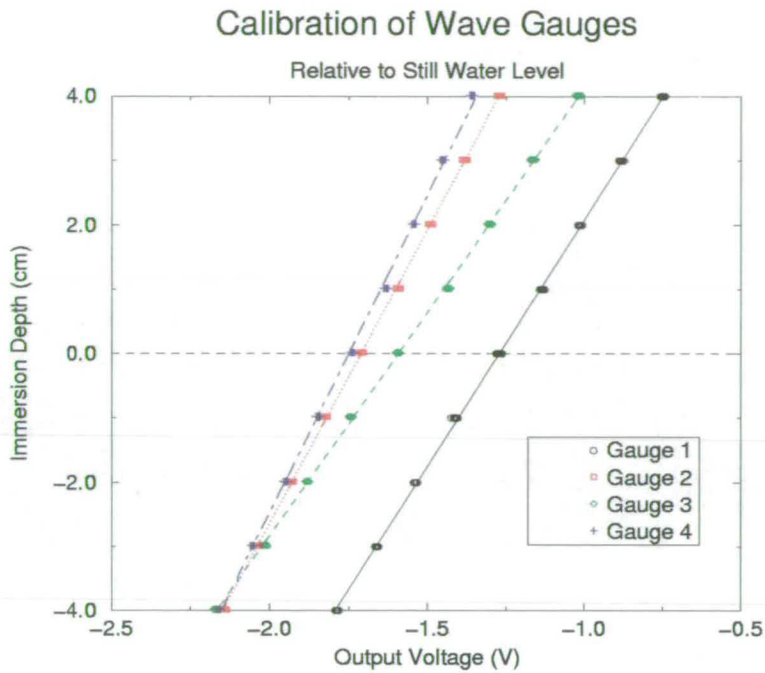


Figure 2.7: Linear response of wave gauges to immersion depth

allow a reasonable time period to be sampled, a more realistic figure was chosen. To obtain this sampling frequency, fully developed wind-waves were recorded at 160Hz. Fourier analysis indicated, figure 2.8, that the majority of the spectral component was below 16Hz. According to the Nyquist sampling theorem [73], sampling at 32Hz would be sufficient to correctly reconstruct this signal. This was the same sampling rate used by Wang and Wu [91] in their studies of wind-induced water turbulence.

To ensure the gauges were operating correctly, they were tested with a sinusoidal paddle generated wave. According to deep water wave theory [26], a wave of 1.39Hz should be 80cm long (the distance between gauges) and assuming the gauges are calibrated correctly, the readings at each gauge should be identical, figure 2.9.

Fourier Transform of Wave Gauge Output

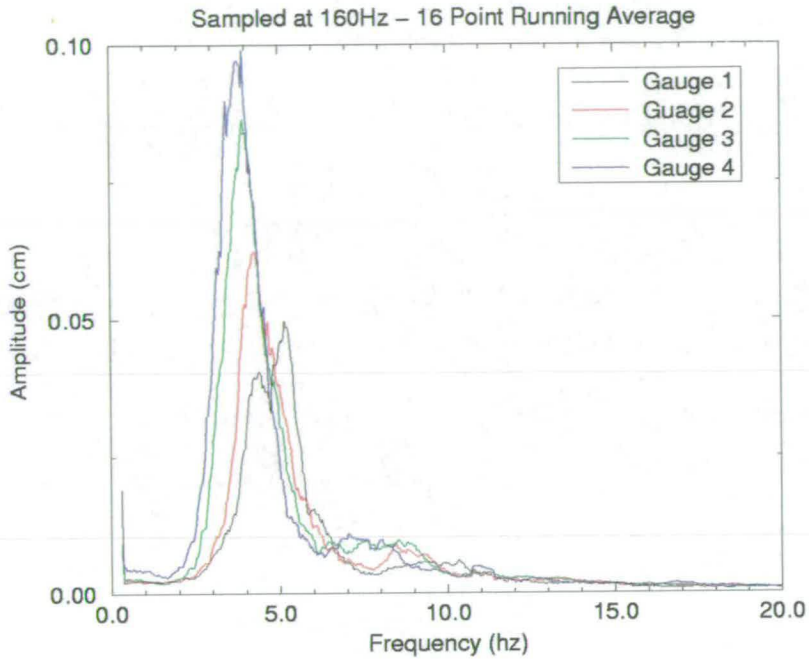


Figure 2.8: Spectral analysis of wind waves

Wave Gauge Test Wave

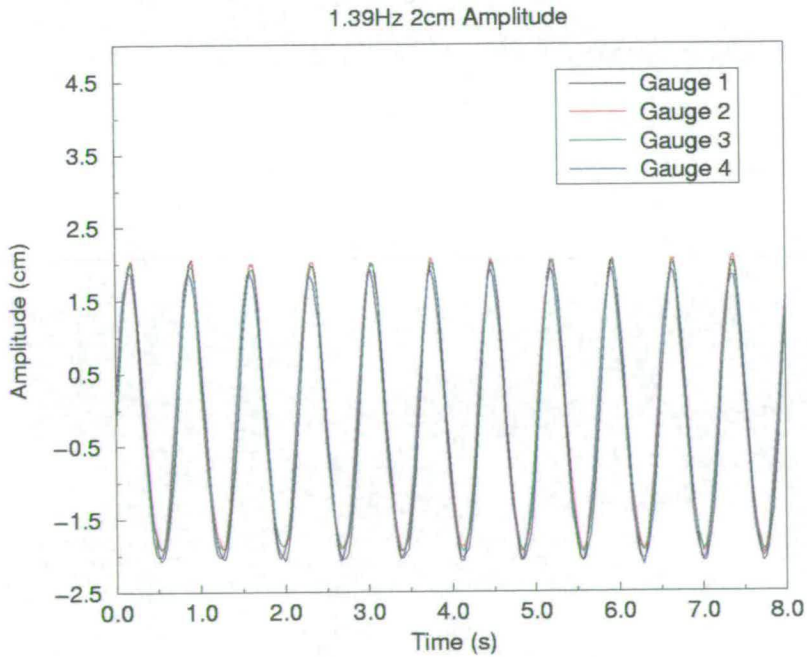


Figure 2.9: Wave gauges operating correctly

Cross tank components

At sea, the waves at any one point will not necessarily be travelling in the same direction. However, in the laboratory studies this is not quite the case. The side walls of the tank only allow waves to build up in the direction of the mean wind flow, thus reducing cross tank motion. Fortunately, this is a requirement for Particle Image Velocimetry since out of plane motion leads to erroneous analysis as will be described in section 3.3.

To test this assumption, two gauges were located at the same fetch, arranged symmetrically about the centre line. The cross tank distance between the gauges was varied and the output from each crosscorrelated using a routine written by the author¹. A value of 1 would indicate that the waves were purely 2 dimensional, with no cross tank component. As can be seen from figure 2.10, at small separations the gauges correlate well. Thus, in the region where the PIV measurements are taken, it is valid to assume that there is little cross tank component in the measured velocity.

2.3 Mini Tank

2.3.1 Introduction

In attempting to observe the trajectories of surface particles, the highly turbulent water motion associated with wind generated waves make it difficult to obtain any confident quantitative results. Added to the fact that the sheer size of the *Green Tank* made it difficult to apply the films in the first place and that the surface films used completely damped out any wave motion, Mechanically generated waves provide highly repeatable, 2 dimensional waves which are not dependent on energy transfer from the wind (which is affected by the presence of a film). The wind-

¹based on Numerical Recipes in C [73].

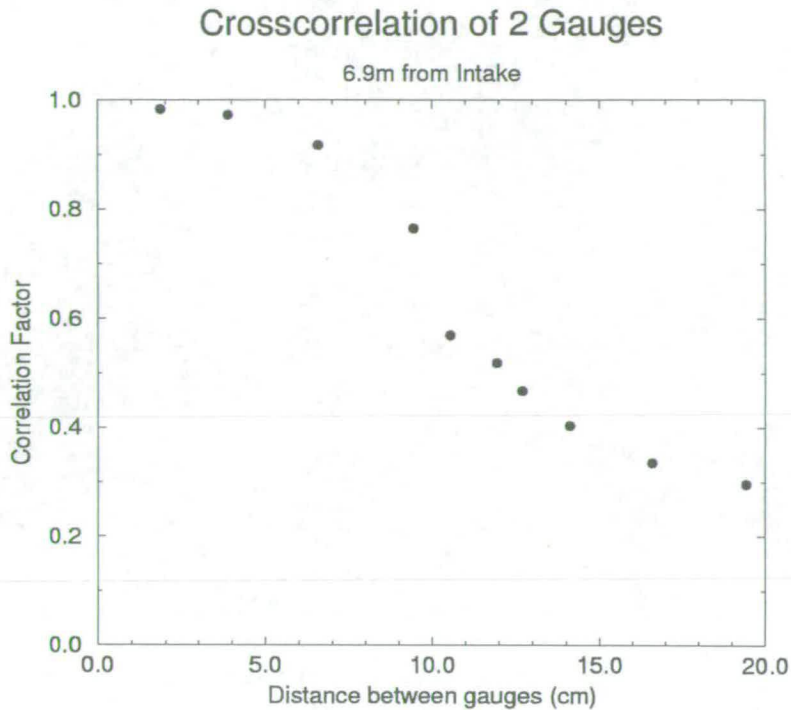


Figure 2.10: Crosscorrelation of Two Wave Gauges

wave spectra above, figure 2.8 indicates that the main component was around 3.5Hz and it seemed sensible for the paddle generated waves to be around this frequency.

The *Green Tank* paddle is not capable of generating such high frequency waves and for the other reasons given above it was decided to construct a custom built facility. This would have to be capable of generating the key features of the wind generated waves, *i.e.* surface shear layer and waves of the same magnitude.

The *Mini Tank* is 2.5m long and 75mm wide. In its simplest set-up, figure 2.11, the paddle generates clean, sinusoidal waves at 3Hz. Foam at the far end acts as a passive wave absorber. Due to the small size, it is very easy to add and clean a variety of surface active films. The tank has a full PIV system and wavegauges similar to those of the *Green Tank*.

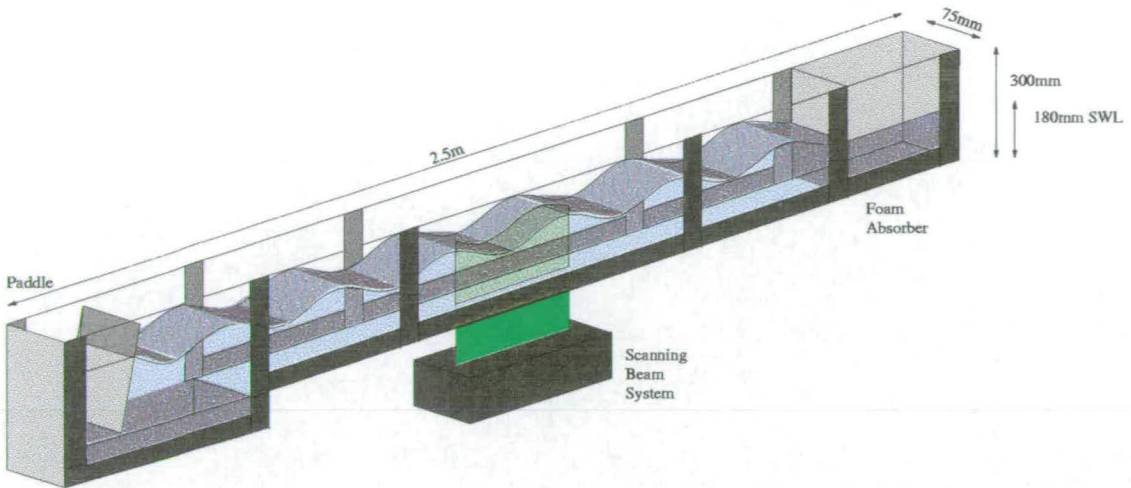


Figure 2.11: Schematic of Mini Tank Facility

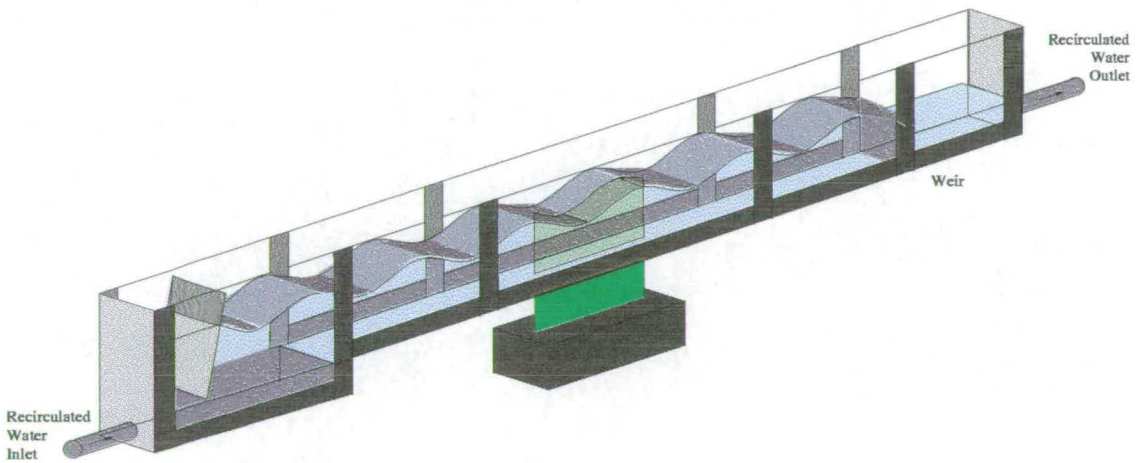


Figure 2.12: Schematic of Mini Tank Facility with weir

2.3.2 Weir Tank

A second feature of the tank is its ability to create a surface shear layer, similar to that observed in wind-generated waves. A weir inserted at the far end of the tank replaces the foam. Water pouring over the weir generates the shear layer and is re-circulated back round below the paddle, figure 2.12. The weir also provides wave absorption as water above the still water level (SWL) pours over the weir, thus preventing any reflection.

Chapter 3

Experimental Techniques

3.1 Summary

Concurrent to the design and operation of the experimental facilities described in the previous chapter, some advancement was also made in the full field flow visualisation techniques of Particle Image Velocimetry (PIV) and Particle Tracking Velocimetry (PTV).

A brief description of the current *state of the art* of both techniques is given along with the author's contribution and how both of these were actually applied to surface film studies.

3.2 Flow Visualisation

The ability to obtain accurate, quantitative, velocity measurements of a fluid under study is not a new concept. For instance, Laser Doppler Anemometry (LDA) has been able to supply single point velocity measurements for nearly 25 years [99]. However, complicated traversing apparatus and highly repeatable experiments have been required to provide full field measurements.

Modern full field flow visualisation is an extension of the popular image of wind tunnel testing. Smoke was introduced at a point (or points) upstream of an obstacle and the path of the smoke taken to be that of the surrounding air. Very

little quantitative measurements could be taken apart from the general behaviour of the flow.

Nowadays, flow visualisation is, in general, a multi stage technique. The first stage being the stroboscopic illumination of tracer particles within the fluid¹. To obtain quantitative results, the tracer particles are imaged by either conventional photography or digital CCD cameras. The recorded images are subsequently post-processed by optical or computational systems to calculate the particles displacement between illuminations. Knowledge of the time difference between successive illuminations allows the velocity to be calculated. The various stages of the process are depicted in figure 3.1.

Westerweel [92] identified three *modes* of recorded image. Where the seeding density of the tracer particles is such that the average distance between particles is much greater than their displacement between illuminations, we can only obtain information about the flow at certain points. In multiple exposure images, individual particles are readily distinguishable from each other and as such this form of analysis is commonly known as **Particle Tracking Velocimetry (PTV)**.

The other two modes both yield velocity information at all points in the image. At slightly higher seeding densities, while individual particles can still be distinguished, it is not generally possible to locate the same particle from exposure to exposure. A statistical analysis is required to process such images. This seeding density and analysis form the basis of the **Particle Image Velocimetry (PIV)** technique.

In fact, as shown by Cowen and Monismith [8] the similarities between modern PIV and PTV are such that both techniques can be applied simultaneously to

¹Smoke can still be used as seeding, but particle diameters are not usually highly controllable.

certain experiments in order to increase the accuracy of the calculated velocity vectors.

The images obtained from very high seeding densities display only a speckled pattern with no distinguishable particles, due to the multiple scattering of coherent light. This technique, known as **Laser Speckle Velocimetry (LSV)** was not used in these studies and as such is not discussed further. However, as it is a specular pattern being matched in LSV, there is no difference in the analysis technique to that used for PIV.

It is a basic assumption of all these techniques that the seeding particles faithfully follow the flow and that their motion is representative of the mean local velocity. The calculated velocity is also taken to be the average velocity between successive illuminations.

3.3 Particle Image Velocimetry (PIV)

3.3.1 Introduction

Particle Image Velocimetry (PIV) is a well established technique for obtaining non-intrusive, full-field quantitative velocity information from the fluid under investigation. One of the most widely used applications (and that which shall be described here) is that of recording a thin slice of 2-dimensional water motion.

Due to the multitude of published work relating to PIV [98, 13, 23, 24, 25, 84, 65] this section shall concentrate only on current PIV development and its specific application to the study of surface films.

3.3.2 Experimental Setup

The basic experimental setup for PIV studies can be seen in figure 3.1. For 2D water wave experiments, a thin slice of fluid is illuminated parallel to the

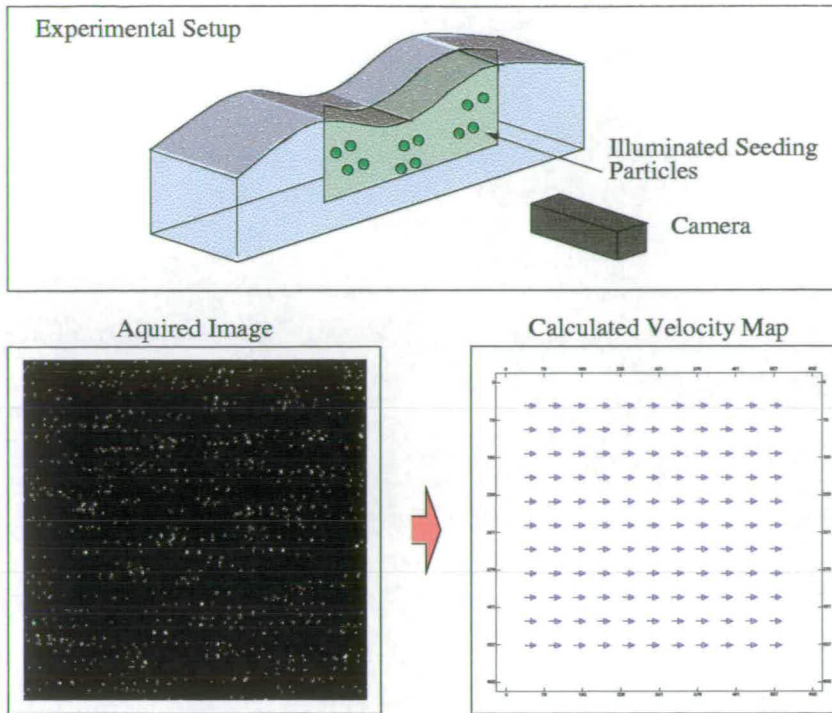


Figure 3.1: Basic flow visualisation setup

direction of wave motion. The images of the tracer particles are captured to a camera, located normal to the light sheet. The acquired image is stored for subsequent analysis from which a velocity vector map is calculated.

3.3.3 PIV Development

PIV development has been one of the major focuses of research of the Fluid Dynamics Group at The University of Edinburgh for the past 15 years. Improvements in manufacturing techniques, laser technology, digital (CCD) cameras and desktop computers have had a major impact on the various stages of PIV.

3.3.4 Developments in Seeding and Illumination

Seeding

In order to record the fluid flow it is first necessary to seed the fluid with suitable tracer particles. These are chosen such that their size is small enough that their

motion can be taken to be that of the surrounding fluid yet large enough that they scatter enough light to be visible. In addition, they should neither alter the flow nor interact with each other. Westerweel [92] described such particles as **ideal**.

The efficiency with which particles scatter light is related to their size and the difference between their refractive index and that of the surrounding fluid [47]. In the case of water motion and solid seeding particles, this difference is minimal, requiring the use of relatively large particles ($> 10\mu m$), [1].

According to Melling [62], it is not only the overall scattering efficiency but the angular distribution which is important. Most PIV experiments are performed such that the observed reflected light is at 90° to the source of illumination, the intensity of which can be several orders of magnitude lower than light reflected at 0° . This fact has been utilised in several PIV experiments, in the so called *forward scatter mode*, where the source of illumination, seeding and camera are co-linear.

The nature of PIV also assumes that in order for the motion of the seeding particles to faithfully represent the motion of the fluid, the effects of gravity and inertia are minimal. Since in these experiments we are concerned with relatively large seeding particles within small amplitude, high frequency (for water wave experiments) waves it is necessary to take these factors into account.

From [47], the settling or upward drift of seeding particles due to gravity is given by;

$$V_g = \frac{d_p^2 g}{18\mu_0}(\rho_p - \rho_0) \quad (3.1)$$

where d_p is the particle diameter, μ_0 is the dynamic fluid viscosity and ρ_p and ρ_0 are the particle and fluid densities respectively.

Melling [62] derived an expression to relate how a particle responds to fluctuations in the surrounding fluid as a function of the frequency, f . U_p^2 is essentially a measure of a particle's kinetic energy, which is related to that of the surrounding fluid, U_f^2 by;

$$\frac{U_p^2}{U_f^2} = \left(1 + \frac{\omega_c}{C}\right)^{-1} \quad (3.2)$$

where

$$C = \frac{18\mu_0}{\rho_p d_p^2} \quad (3.3)$$

$$\omega_c = 2\pi f \quad (3.4)$$

In addition to the requirements stated above, it is also generally desirable that the seeding particles are non-toxic, non-corrosive, fairly inexpensive and in particular for these studies, non-surface active.

Conifer pollen was, until recently, the chosen seeding particle but advanced manufacturing techniques have brought about silver coated, hollow glass spheres with a mean diameter of $15\mu m$ and density of $1.6gcm^{-3}$ which are more suitable.

From equation 3.1 these particles have a downward settling velocity of around $0.07mms^{-1}$ which accounts for a fraction of a percentage error in our calculated velocities (approx. $2 - 20cms^{-1}$). The fact that the particles remain suspended for several hours visually confirms this.

Using the values of particle diameter and density to produce figure 3.2 from equation 3.2, we can assume the particles faithfully follow the surrounding flow, in the 1-100Hz range.

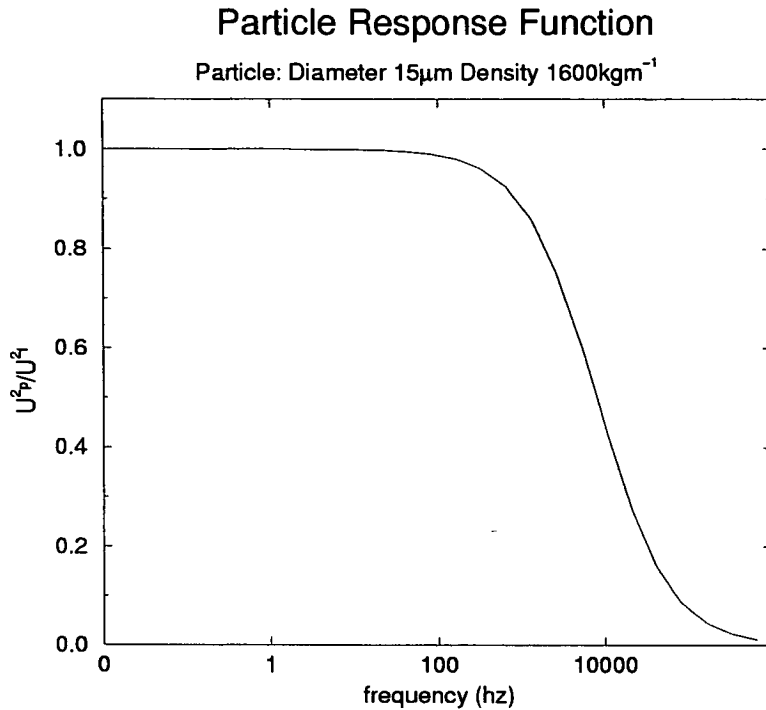


Figure 3.2: Response of particle to oscillating flow

Illumination

Illumination, in the case of water motion, is most commonly produced by a laser generated pseudo light sheet. This is to provide a thin 2D illumination and overcome the Gaussian intensity profile that is obtained when the beam is simply expanded using a cylindrical lens.

The scanning beam system developed at The University of Edinburgh [24, 25] directs an incoming beam from a CW Argon-Ion laser to a rotating octagonal mirror. This mirror is located at the focus of a parabolic mirror. The resulting scanning beam produces, in effect, a thin (few millimetres thick) sheet of laser light, figure 3.3. It should be remembered that while the sheet will have a constant intensity across its width (assuming a perfect parabolic mirror), it will still have a Gaussian profile through its depth.

Previously, only high power (15W), water cooled lasers were capable of gener-

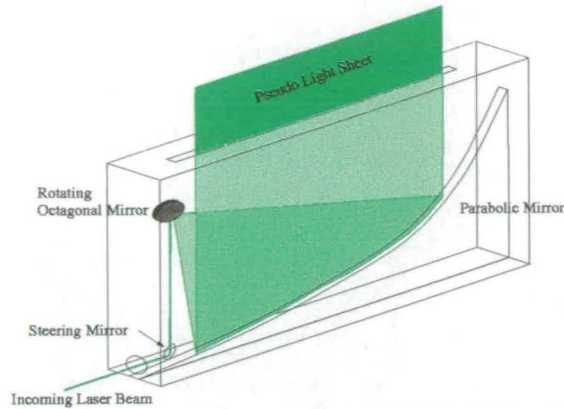


Figure 3.3: Scanning beam illumination system

ating the necessary illumination. Image capture developments and modern, diode laser pumped Nd:YAG continuous wave (CW) laser technology has allowed the use of the far more user friendly, low power (300mW), air cooled laser currently in use.

With the use of such a low power laser the effects of scan time, seeding density and depth become important. Increasing the scan frequency causes the laser beam to traverse faster across the sheet. Consequently each seeding particle is illuminated by the beam for a shorter period of time. Since the intensity of the captured image (using either wet photography or CCD arrays) is dependent on exposure time, or in this case, illumination time an appropriate adjustment may have to be made to the optical setup to ensure sufficient contrast. Passing through a depth of seeded water will attenuate the beam and as such, low power lasers are only of real use in either very low seeding applications or over short distances/depths. The 15W laser was still required for experiments in the Green Tank due to the depth of water.

The low power laser / scanning beam system was also successfully used by the author in a wind tunnel test on an aircraft model.

3.3.5 Image Capture Development

In the earlier PIV systems of Gray [23] and Skyner [84], used locally until fairly recently, the actual recording of the tracer particles was done by means of wet-photography. As early as 1991 Willert and Gharib [98] demonstrated that digital CCD cameras could be used to remove the bottle-neck associated with negative development. Especially in the case of obtaining turbulence statistics, it is vitally important to obtain as many independent results as possible and the removal of the negative development stage can represent a significant time saving.

Locally, most image acquisition is now performed digitally due to the work of Dewhurst and Jakobson [13], the author and others, brought about by advancements in the quality and cost of CCD camera technology.

Validity of CCD image acquisition

The spatial resolution of CCD devices is much lower than that of photographic film. Typical CCD arrays have around 80 sensors per mm over an area of around 10mm^2 while the resolution of photographic film is 100-300 lines mm^{-1} over $35 - 50\text{mm}^2$.

Westerweel [92] demonstrated that, given suitable consideration to the experimental parameters (magnification, particle size etc.), CCD arrays were suitable for PIV image acquisition since we are only interested in the position of the particles and not their exact shape. A consequence of this is that we cannot fully identify the precise centroid of the particle. While this is not necessary for PIV, it is required for Particle Tracking, as noted by Prasad [72].

In a later paper, Westerweel [95] went on to prove that measurements of turbulent statistics obtained from CCD images were comparable to those obtained from wet-film PIV and, in fact, the ability to collect many times more indepen-

dent results in a certain period of time using CCD based acquisition make this technique more suitable.

With the use of digital CCD cameras and their associated discretised image plane, it is assumed that each sensor, or pixel, is square. While this is the case for some of the cameras in use locally, those with rectangular pixels must have the final vectors scaled accordingly.

Single Camera Systems

PIV based on wet-photography obtained multiple images of each tracer particle on a single frame. Autocorrelation routines, discussed in section 3.3.6, produced the resulting velocity vector maps. The initial, single camera, digital systems [52, 76] were simply an extension of this and suffered from the same problems of directional ambiguity and erroneous calculations in areas of low velocity.

Multiple Camera Systems

One method of overcoming these problems is to capture each successive particle image to separate CCD frames. The fixed frame rate of commercially available CCD devices makes it is necessary to capture them to physically separate CCD arrays. A novel double camera system based on this idea has been developed by Dewhirst, [13], and is in use at Edinburgh, figure 3.4². A beam splitter placed behind the camera lens allows the flow to be imaged by two separate, independently synchronised CCD cameras. The use of an external, digital pulse generator to control the time separation permits a pair of successive images to be obtained within micro-seconds³ of each other.

²Diagram courtesy of Tim Dewhirst

³The uncertainty inherent in the resetting of the CCD arrays is of the order of micro-seconds. Due to this, the minimum time separation that can be reliably used is approximately 5 micro seconds [12]

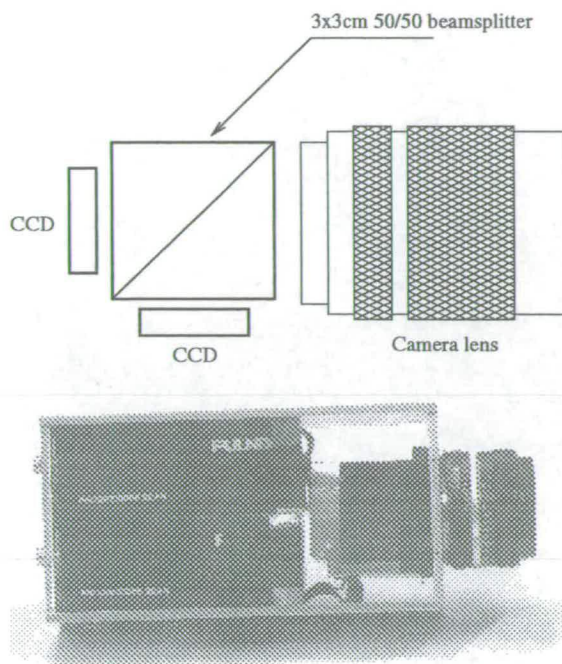


Figure 3.4: 2-CCD array system

On-board frame stores hold the images on the cameras until downloaded to the frame-grabbing PC for future processing.

The particle images taken from these separate frames can be analysed by crosscorrelation. This method has neither the problems of directional ambiguity or those associated with small displacements. Section 3.3.6 describes in detail the advantage of the use of this camera during analysis.

The timing of the cameras can be precisely controlled and synchronised to the scanning beam system such that for the duration of the exposure, the light sheet appears as continuous illumination. A similar 4-camera system has also been used in the study of accelerating flows, [13, 11]. The ability to have very small time separations between images reduces the error in the assumption that the particles' velocity is constant between illuminations.

Both the single and multiple CCD PIV systems allow the results of a particular

experiment to be obtained within minutes where previously they would have taken hours.

The author has been responsible for the hardware testing and writing of software drivers for several of the new CCD cameras currently being used at Edinburgh University.

3.3.6 Post Processing Development

Analysis of the resulting image has been the second major focus of PIV advancement. One of the consequences of camera improvements has been to allow the shift from analysis by autocorrelation to analysis by crosscorrelation.

During this time, the essential essence of PIV analysis has remained the same. That being, the image is subdivided into many small *Interrogation Areas*. A correlation analysis is applied to the intensity distribution, $a(x,y)$, of each interrogation area such that [73]:

$$A(x, y) = \int \int a(x, y) a(x - x', y - y') dx' dy' \quad (3.5)$$

The highest signal peak of the correlation function, $A(x,y)$, is related to the mean particle displacement between exposures, which in turn is related to the mean fluid velocity in that area.

Thus, it is taken that the velocity of all tracer particles within an interrogation area is constant and as such, the size of these areas must be chosen to fit this assumption.

Analysis by Autocorrelation

In the case of multiply exposed single frame images, such as in figure 3.5, an autocorrelation function is obtained for each interrogation area. Rather than

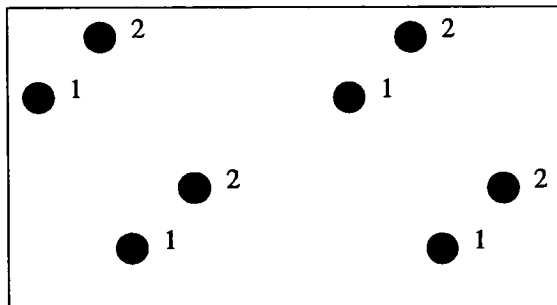


Figure 3.5: Simplified multiply exposed single frame image

calculating the correlation function directly, using the Wiener-Khintchine theory we can calculate it by the computationally less intensive method of Fourier Transforms [73]⁴;

$$A(x, y) = FT^{-1}\{|FT\{a(x, y)\}|^2\} \quad (3.6)$$

An example of the 2D autocorrelation function $A(x, y)$ can be seen in figure 3.6. The central tallest peak is the self-correlation peak, the other peaks being the signal peaks and the remaining values are background noise. Background noise appears as a result of particles incorrectly correlating with their neighbours, overlapping particle images or particles moving out of the interrogation area. Accurately locating the signal peaks relative to the self-correlation peak yields the mean displacement from which the velocity can be obtained for that area.

In order to obtain highly accurate velocity vectors from the discretised correlation plane it is necessary to locate the peak to *sub pixel* accuracy. We can make use of the fact that, with appropriate selection of experimental parameters, the correlation peak will cover more than one pixel. Westerweel in his thesis [92] also proved that the two displacement directions can be dealt with independently

⁴Direct calculation of the correlation function for an $n \times n$ interrogation area involves n^4 operations. The same operation in Fourier space involves only n^2 calculations. In fact it is usually Fast Fourier Transform (FFT) algorithms which are used, which involve only $N \log_2 N$ calculations

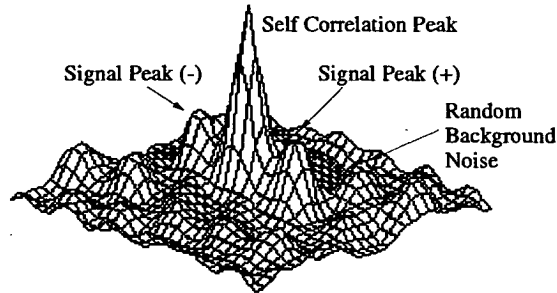


Figure 3.6: Example of 2D Autocorrelation function

and that only the nearest neighbours contribute *significant* information to the estimation of particle image displacement. Thus, fitting a function to these three points and calculating its maximum should find the peak to sub-pixel accuracy. Willert [97] investigated several of these, so called, *three point estimators* including centre of mass, parabolic fit and Gaussian fit. Others such as Westerweel [92], Cowen [8] and Dewhurst [11] (the author of the PIV analysis code used for some of the experiments) have found the Gaussian fit estimator to be the more accurate. This would seem to follow from the fact that the particle images have essentially a Gaussian intensity distribution and correlation of a Gaussian with another yields a further Gaussian.

Two features of the autocorrelation function result in errors in the calculated velocity vector. Firstly, it is symmetric⁵, thus there is a directional ambiguity of 180° in the resulting velocity vector. This follows directly from the fact that in a multiple exposure image, there is no knowledge of which particle image was captured first. Secondly, where the velocity is small, the signal peaks lie too close to the self correlation peak to be resolved. This is a consequence of the fact that the multiple particle images lie on top of each other.

A number of novel methods have been suggested to *tag* the particle images

⁵This symmetrical feature is actually used to increase the resolution of the peak detection. Both peaks are detected and the mean value extracted

and thus remove the 180° ambiguity. Using a different colour laser for each illumination and capturing the resulting image with a colour camera identifies which particle image came first. A computationally applied colour filter separates the particles into separate images which can be crosscorrelated by the technique described below. However the problems of optical alignment and the fact that in areas of low velocity particles still lie on top of each other, have prevented widespread use of this technique. The use of modern 3-CCD colour cameras would solve this problem however there is still the experimental difficulty associated with aligning two lasers of different wavelengths.

Another scheme proposed by Lawson *et al.* [52] made use of adaptive optics to modify the point spread function between exposures. A filter could separate each image during analysis but the idea was not widely adopted for the same reasons given above.

The most common system in use is that of *Image Shifting*. A known shift is applied to all vectors during the image acquisition by means of panning the camera or viewing through a rotating mirror. All vectors have the same sense of direction and particles in stationary areas of the flow no longer appear to lie on top of each other. This shift is removed at the analysis stage and the problems of directional ambiguity and zero displacement are removed. However the additional apparatus complicates the experimental set up and the rotation adds a geometric distortion which must also be accounted for. A full description of this technique can be found in Morrison's thesis [65].

The earliest PIV analysis system in use at Edinburgh performed the first (forward) FT optically by probing the developed negatives with a low power laser and using the Fourier Transforming properties of a lens. The photographic negative was translated such that the laser stepped across the entire frame in

1mm intervals. A small CCD camera located in rear focal plane of the Fourier Transforming lens and recorded the Youngs fringes and a PC computed the second (reverse) FT using a Fast Fourier Transform (FFT). The resulting process took around 2 seconds per interrogation point.

The modern system in use is a purely digital process. Images are taken directly from the CCD camera. A fast Pentium (P166) based PC computes both FFT's at speeds ranging from 30-90 points per second. *State of the art* Pentium II 400MHz based computers can compute over 200 points per second.

Where quantitative results are required, a further stage of post-processing removes erroneous vectors⁶ and replaces them with ones interpolated from its neighbours. In studies where the mean flow direction is known, directional biasing can be applied to the calculated vectors to remove the effects of the 180° ambiguity.

Figure 3.7 is the image of a spinning disk covered with glass particles. This was illuminated by a low power laser. No image tagging or shifting was used during image acquisition. Analysis by autocorrelation without any post processing, figure 3.8, clearly shows directional ambiguity and erroneous vectors near the centre, where the mean velocity is small. In this area, the ratio of erroneous to real vectors is approaching 50%.

In the above experiment each particle is illuminated twice during the exposure. The experiments of Keane [44] showed that while the probability of valid vector detection increased as the number of particle images increased, this could have effects on apparent seeding density and illumination (especially with pulsed laser systems).

⁶Erroneous vectors are identified by the application of a Global Histogram Filter. A 2 dimensional histogram is created of all calculated vectors. Those which lie outwith 2 standard deviations of the mean in either the X or Y direction are discarded [12].

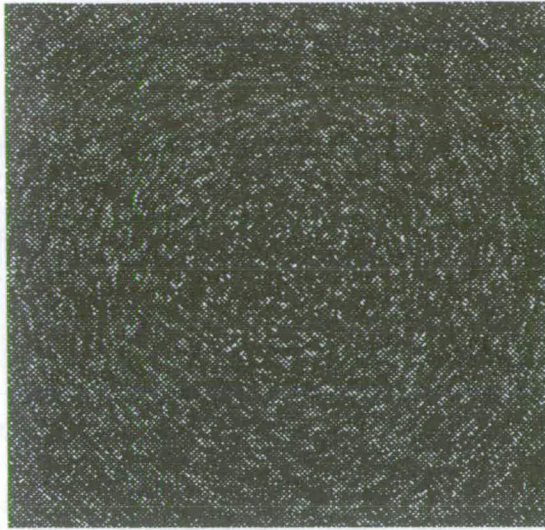


Figure 3.7: Double exposure of each particle

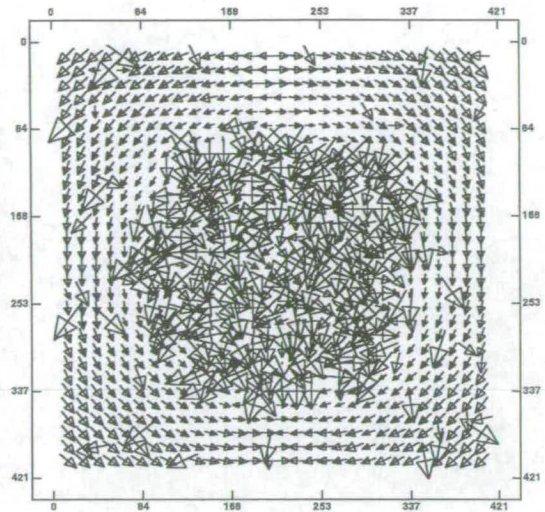


Figure 3.8: Analysis by Autocorrelation - No post processing applied

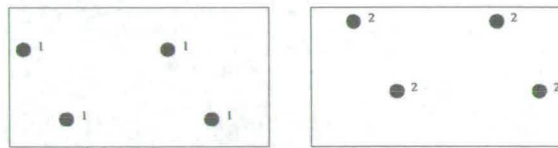


Figure 3.9: Simplified single exposed multiple frame image

Analysis by Crosscorrelation

Analysis by crosscorrelation assumes that each illumination of the seeding particles has been imaged to separate CCD frames, figure 3.9. If we take the intensity distribution of an interrogation area in one image to be $a(x,y)$ and the same spatial area from the second image to be $b(x,y)$ we calculate our correlation function $C(x,y)$ according to;

$$C(x, y) = FT^{-1}\{FT\{a(x, y)\}FT\{b(x, y)\}\} \quad (3.7)$$

The extracted displacement is again obtained by means of peak detection but in this case there is no symmetry (figure 3.12) and the 180° ambiguity is removed. Areas with low local velocity can be resolved because although particles are in

the same location, they are now on different frames and no longer overlapping. Another feature of the crosscorrelation function, as noted by Keane and Adrian [45], is that the height of the noise peaks are significantly lower (roughly half) than those for an equally seeded autocorrelation interrogation area. This is explained by the fact that each double exposure autocorrelation area will contain twice as many imaged particles leading to twice as many spurious correlations.

If we now image the spinning disk to separate frames, figures 3.10 and 3.11 the resulting velocity vector map, figure 3.13, displays the obvious advantage of the crosscorrelation method. There is now only one erroneous vector amongst the 899 correct ones.

3.3.7 Digital Particle Image Velocimetry (DPIV)

A consequence of this fully digital (image capture and analysis) approach is that the technique is now commonly referred to as **Digital Particle Image Velocimetry**.

DPIV is a highly active area of research in several countries (e.g. USA, China, Germany, UK) with several commercial systems (e.g. TSI, Dantec, OFS) being used to aid industrial design (e.g. Volvo, Rolls-Royce).

3.3.8 Sources of Errors in DPIV

Strict attention to the possible sources of error must be taken into account during the experimental stage to ensure accurate PIV analysis. Keane and Adrian [43] identified the 6 most important parameters regarding optimising PIV performance:

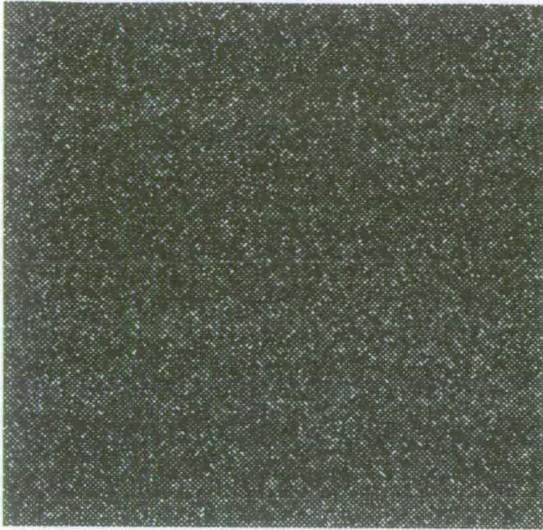


Figure 3.10: Image from 1st Exposure

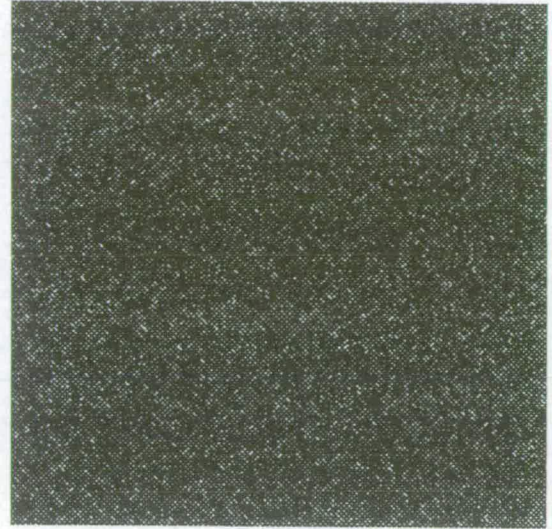


Figure 3.11: Image from 2nd Exposure

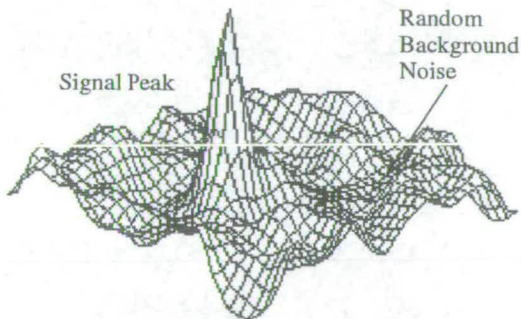


Figure 3.12: Example of 2D Cross Correlation Function

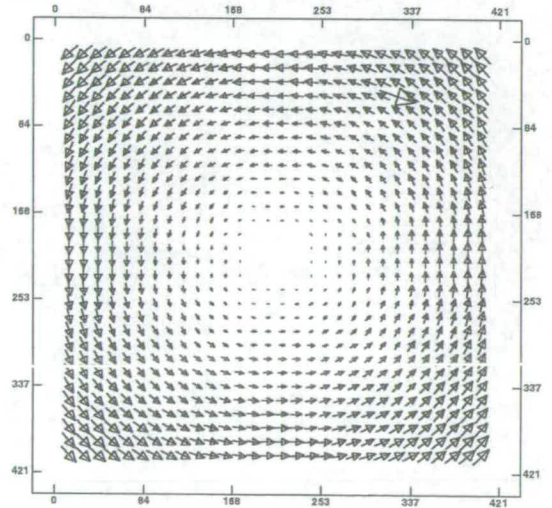


Figure 3.13: Analysis of Image by Crosscorrelation - No post processing applied

Observed Mean Velocity

The observed mean velocity manifests itself as the particle spacing on the acquired image(s). The scan rate of the light sheet, magnification of the camera optics and exposure time all have to be set such that for the desired interrogation area, the mean particle displacement is less than half of this. In the case of autocorrelation,

it is desirable to have more than two images of each particle and as such the, mean particle displacement should be much less than half the interrogation width. It is also necessary, as observed by Adrian [2], to ensure that the displacement is greater than the uncertainty in its measurement.

Observed Particle Size

With reference to the validity of CCD based image acquisition, several researchers including Kompenhans *et. al* [47] and Cowen and Monismith [8] have shown that the three point estimators, particularly the Gaussian one, perform best where the particle images occupy 2-3 pixels (in each direction). This is explained by the fact that the width of the correlation peak is directly related to the width of the particle image (d_p). For small particle images ($d_p < 1.5$ pixels), the peak is so narrow such that the values surrounding the peak are close to that of the background noise. The sub-pixel estimator fails and the calculated peak location tends towards integer values. Surprisingly, the error also begins to increase as the width of the particle image increases. This is due to the fact that the correlation peak increases in width and decreases in height. Neighbouring points have very similar values and the superposition of the random background noise leads to spurious peaks.

Seeding Density

The effect of increased seeding density is to increase the number of particle pairs in each interrogation area, thus reducing the measurement uncertainty which results in an increase in the height of the correlation peak. Keane and Adrian [45] found that the probability of detecting a valid vector rises steadily with seeding density to greater than 95% with around 10 particle pairs per interrogation area.

Also, as noted by Westerweel [93] it is assumed that the fluid is homogeneously

seeded otherwise poorly seeded areas will not contribute to the estimation of the mean velocity.

Out-of-plane motion

Although, recent experiments by Kompenhans *et. al* [47], Dewhurst [11] and Brucker [5] have attempted Dual-Plane PIV measurements to obtain the out-of-plane velocity component, any out-of-plane motion will tend to cause an error in the calculated velocity. This is in general due to the loss of particle pairs as particles either move completely out of the light sheet or suffer from an intensity change due to the Gaussian intensity profile through the depth of the light sheet.

Keane and Adrian [45] suggested increasing the width of the light sheet between the first and second exposures but this will reduce the overall intensity of the second sheet and greatly increase the complexity of the experimental setup, thereby reducing any benefit that may have been gained. Therefore, in order to keep this error to a minimum, the experiment should be arranged such that the fluids cross sheet velocity component is kept as small as possible.

Bias Error

Conventional digital correlation analysis is prone to a form of error known as **bias error**. The selection of interrogation area size, sampling theory and certain features of the correlation plane will tend to add a bias to the calculated velocity. Keane and Adrian [45], Westerweel [92], Kompenhans *et. al* [47], Cowen and Monismith [8] and Dewhurst [11] have performed simulations in order to characterise and reduce these errors.

A 1D slice from the centre to the edge, through the signal peak of the the correlation function is depicted in figure 3.14. The signal peak is a displacement *function* rather than a unique value, or δ -function. The peak of this function

represents the mean velocity [93].

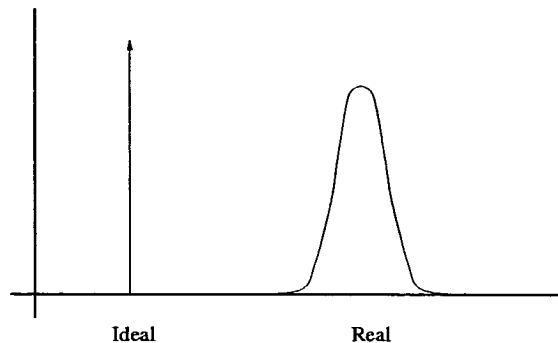


Figure 3.14: Ideal and real displacement functions

This is partially due to the fact that the particle images are not precise δ -functions and also that the flow is not exactly uniform over the entire interrogation area. Thus, each particular image pair contributes their unique displacement to the overall displacement function.

The greater the spread of velocity within the interrogation area, due to shear for example, the broader and lower (as the area under the curve must remain the same) the peak becomes.

The correlation function is also modified by a term relating to the finite width of the interrogation area. This is in effect the correlation function of the two interrogation areas. For square interrogation areas, this will be a triangular function [93], \mathcal{F} , as shown in figure 3.15.

This has the effect of decreasing the peak non-uniformly, skewing the peak and therefore the measured displacement becomes biased towards zero. Since any velocity gradient present in the fluid will widen the peak, and thus exacerbate this problem, this effect is commonly known as **gradient bias**.

In simple terms this may be thought of as being due to large displacements being more likely to cause particles to leave the interrogation area and therefore small displacements will contribute more to the displacement function. However,

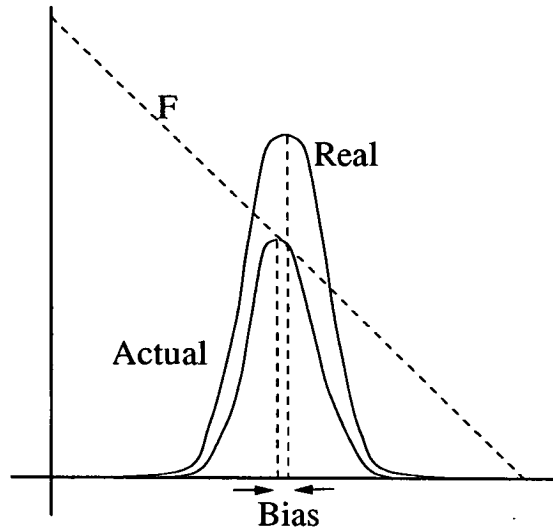


Figure 3.15: Actual displacement functions modified by \mathcal{F}

as Westerweel [93] noted, this rather simplistic approach is wrong as the bias still appears in uniform velocities.

As would be expected, this effect decreases as the size of the interrogation area increases, at the cost of spatial resolution. Mathematically, this is because the width of the base of the function, \mathcal{F} , is twice that of the interrogation area. As the function widens, its gradient decreases and its effect on the displacement function decreases[93].

Since the effect of the function can be precisely calculated mathematically, it is possible to correct for it. These so called *weight kernels* can be applied to the displacement function to retrieve the unbiased estimate⁷.

Other approaches such as increasing the size of the second interrogation area can decrease this bias. Again the simple explanation, that by increasing the size of the second area all particle pairs will be found, was found by Westerweel to be inaccurate.

Figure 3.16 indicates the mathematical reasoning behind why different sized

⁷The phrase *unbiased estimate* in relation to DPIV was first coined by Westerweel

interrogation windows decrease the bias error. The function, \mathcal{F} , is flat at the point where it intersects the real displacement function and decreases it uniformly. It also indicates that it does not matter which interrogation window is increased in size.

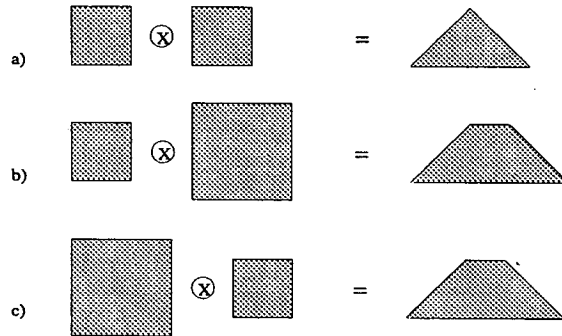


Figure 3.16: Effect of different interrogation window sizes on the function, \mathcal{F} . Cross in circle denotes crosscorrelation function

This bias error is typically of the order of 0.1pixels and while not altering velocity calculations greatly, it can have significant effects on derived results, such as vorticity.

Another form of biasing, which Keane and Adrian [45] referred to as **detection bias**⁸ arises from the fact that as the correlation peak decreases in height and increases in width, due to either increased particle image diameter or increased particle image displacement, the likelihood of a random noise peak being higher than the signal peak increases. This detection bias can be reduced by careful consideration to detail of the experimental setup and the use of crosscorrelation analysis where the amplitude of the random peaks is half that of those in autocorrelation, as noted earlier.

⁸Although a common term, this is actually a misnomer because it is not a systematic bias that can be mathematically characterised

Data Validation Criterion

As there is a non-zero probability that a noise peak will be detected as the highest peak of the correlation function, each velocity vector map will contain a certain number of erroneous vectors. In order to minimise these and remove the need for human validation, vectors are only accepted if their associated peak is substantially larger than the surrounding background noise. Keane and Adrian [43] suggested, based on simulations, that the height of the greatest peak should be between 1.2 and 1.5 times that of the next highest peak. The EdPIV analysis software used in these studies used a value of 1.2

Where this condition is not met, this will result in a gap in the velocity vector map. It is often the case that a continuous map is required and Nogueira [67], Kompenhans [47] and others have suggested several ways of interpolating the missing vector value from its neighbours.

Other Sources of Error

Huang [35] studied the effect of electronic camera noise on PIV results but found them to be much smaller than the sources listed above. His findings also found that the fully-digital approach (described in section 3.3.10 below) was even less prone to error. Stanislas [86] carried out an experimental programme to investigate the effect of camera lens and focusing on PIV results but the obvious conclusion is to use the best available equipment and to arrange the experimental set up such that the recommendations listed above are followed.

As noted by Fincham [19] and Dewhurst [11], but usually forgotten by most people implementing PIV algorithms, the resulting velocity vector is actually the mean velocity calculated between two points.

Thus velocity vectors should not be located at the interrogation centre, but at

a point half way between it and the mean displacement. While not effecting the calculation of velocity, this can have significant effects on calculated derivative quantities, such as vorticity.

3.3.9 Optimisation of PIV Parameters

A recent study by Westerweel [94] also found that the RMS error in calculation of the particles displacement, u , decreases rapidly when $|u| < 0.5$ pixels. If the second interrogation window is offset by the integer part of the particles displacement, the residual displacement will always be less than half a pixel with the resulting decrease in error.

This technique, known as *re-interrogation*, where the first pass of the PIV algorithm obtains the approximate velocity vector. During the second pass, the interrogation window in the second image is moved by an (integer) amount calculated from the first pass. Also, since the height of the correlation peak is related to the number of particle pairs, by moving the second interrogation area, this greatly increases the chance of finding all particles from the first image in the second image. Thus the size of the interrogation area can be reduced, increasing the spatial resolution, while maintaining the same signal-to-noise ratio as obtained with the larger interrogation size without the window offset.

In general to obtain the greatest number of valid vectors, it is advantageous to have some *a priori* knowledge of the flow field under investigation.

3.3.10 Future of PIV Development

The ultimate goal of PIV systems is the ability to provide *real-time* velocity vector maps and statistics of the fluid being observed. While there are such systems in operation, such as the Dantec installation at the Iowa Institute of Hydraulic Research, these are highly specialised and prohibitively expensive for

common use.

The PIV systems in development at Edinburgh are the first stage of realising this goal using affordable, *off the shelf*, optics and electronics. Actual velocity maps can be obtained within minutes of imaging the fluid. Further advancements in low-cost computer hardware will bring processing time down to sub-seconds. Until recently, although image acquisition was performed with digital CCD cameras, it was actually an analog video signal from these cameras which was stored by the PC. Current *state-of-the-art* CCD cameras and frame-grabbing equipment allow a fully digital approach with resulting greater control and ease of use.

3.3.11 DPIV applied to surface film studies

Prior to this work, there was virtually no DPIV system available locally. Experiments in the wind-wave tank generated highly turbulent flows with strong shear and low mean velocities far below the surface. It became clear very early that a digital, crosscorrelation approach would be required. While the multiple CCD camera was developed by Dewhirst [11], the author was responsible for ensuring the underlying digital infrastructure was in place. In addition to creating a modern network to transfer, store, and process the data, a frame-grabbing routine was written. This was capable of taking multiple images in real time from both the single and multiple camera DPIV system for future processing.

Flow measurements below the surface of wind-waves and wind induced shear were one of the first uses of the local DPIV system. Analysis by crosscorrelation produced results similar to figure 3.17. The full results presented in chapter 5 will show these to be in good agreement with theory.

The computer network is now used by all active researchers in the group and fully integrated into the departmental network. The frame grabbing routine has been used in a variety of other projects.

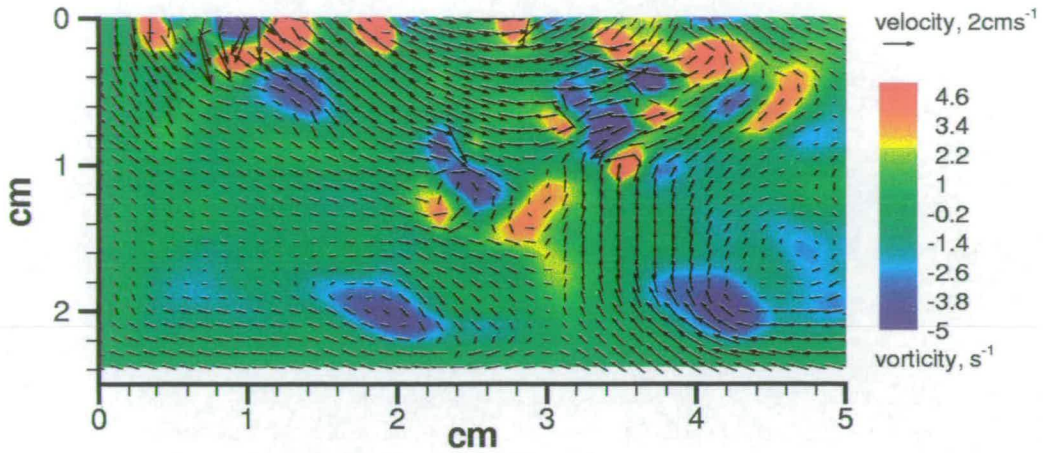


Figure 3.17: Example of DPIV analysis of wind generated waves

It was also originally intended to perform DPIV measurements on the air flow above the water surface. Despite several attempts this proved to be an exceptionally difficult task. This was due to a number of factors:

- The air phase would need to be seeded with a large quantity of suitable non-surface active, non-toxic material. Water mist was decided to be the only suitable material but would lead to other problems due to the open ended nature of the wind tunnel.
- Another major problem is the illumination of the air-phase. Using the same scanning beam system as for the water phase, air seeding particles

are randomly and multiply illuminated by refraction at the water surface. A separate scanning beam box would need to be mounted above the wind tunnel but due to the beam delivery system in the laboratory this was not possible. Current advances in low power lasers or fibre-optic beam guides may make this possible in the future.

- The air close to the water surface is in an area of high velocity gradient. As seen earlier, the velocity as little as 20cm from the water surface is up to $5ms^{-1}$ dropping to zero (or possibly negative values) close to the surface. These conditions make for poor PIV measurements and at the time of these experiments, the multiple-camera system (which could possibly cope with such conditions) had not been invented.

Although a few images were recorded, it was virtually impossible to get any confident quantitative results from the area close to the water surface. Peirson [70] claims to have made such measurements but lack of published results indicates that these were of low quality, presumably for the reasons stated above.

Future experiments with modern lasers, fluorescent seeding, crosscorrelating cameras and Particle Tracking software could make these valuable experiments a possibility in the near future.

3.4 Particle Tracking Velocimetry (PTV)

3.4.1 Introduction

As noted by Cowen and Monismith [8] there are two distinct forms of Particle Tracking Velocimetry (PTV); multiply exposed single images and single exposure multiple images. These are analogous to the auto and crosscorrelation methods of PIV. Using the same experimental apparatus as that for PIV it is possible

to obtain both types of image although the former method of multiply exposed single images was chosen for the following reasons:

- The main focus of this work was to investigate the change to surface particle trajectories under the influence of surface active films. This could only be achieved by tracking the motion of such particles. PIV analysis assumes particles move in straight lines between exposures and in our case, this is not so. The additional fact that it is currently quite difficult⁹ to take many images with small time separations makes PIV quite limited for this work as figure 3.18 indicates. Multiply exposed single images do not suffer from this problem as the time between successive illuminations can be very short as this is dictated only by the laser scan rate. The length of exposure can be timed such that complete circular trajectories can be captured. Although there will be the 180° directional ambiguity in each velocity vector although the true sense can be inferred from the direction of propagation of the wave.
- The particles are actually tracked by hand. This is only really feasible where all the particle exposures are in the same image.

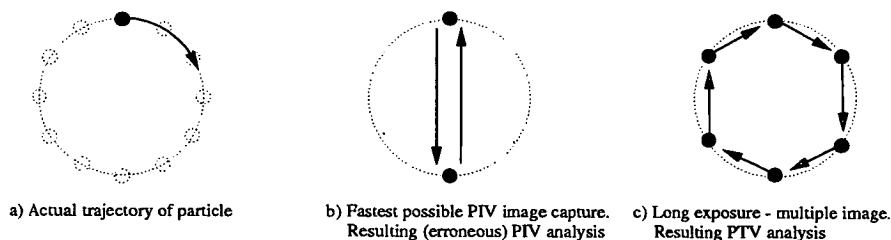


Figure 3.18: Possible ambiguity in velocity derived from PIV images

- To prevent storing images with no useful data it was useful to see the entire trajectory on a monitor before it was saved to disk. Again this is only really possible when the entire trajectory is on a single frame

⁹Though the multiple camera systems of Dewhurst and current advances in image acquisition software may soon overcome these difficulties

3.4.2 Actual Implementation of PTV software

To track the motion of these surface seeding particles, software was written by the author to analyse the long exposure traces. A single CCD camera was used in conjunction with very low seeding to obtain multiple (about 60+) images of each tracer particle, an example of which can be seen in figure 3.19.



Figure 3.19: Typical Multiple Exposure Image - Single Camera

To save on development and coding time it was decided to use semi-manual tracking. The approximate location of a particle is selected by the user. A peak detection routine then locates the exact centre of the particle, figure 3.20. Simple peak detection would, however, return a poor location due to the discretised nature of the image plane. Therefore, once the pixelised location of the peak has been detected (x, y) , a Gaussian curve is fitted to it and its nearest neighbours (a separate one for x and y) and used to calculate the true location of the peak (x_p, y_p) . Equation 3.9¹⁰ describes how this is implemented. $P(x, y)$ is the intensity value at the position (x, y) .

¹⁰from Kompenhans *et al.* [47].

$$\begin{aligned}
 x_p &= x + \frac{\ln P_{(x-1,y)} - \ln P_{(x+1,y)}}{2 \ln P_{(x-1,y)} - 4 \ln P_{(x,y)} + 2 \ln P_{(x+1,y)}} \\
 y_p &= y + \frac{\ln P_{(x,y-1)} - \ln P_{(x,y+1)}}{2 \ln P_{(x,y-1)} - 4 \ln P_{(x,y)} + 2 \ln P_{(x,y+1)}}
 \end{aligned}
 \tag{3.8}$$

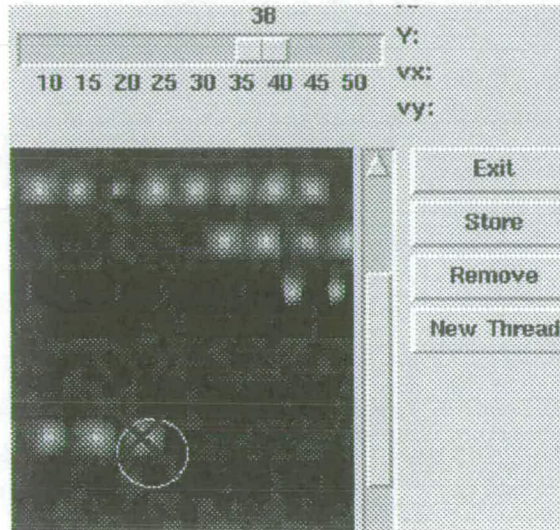


Figure 3.20: Exact location of particle

Gaussian peak fitting was chosen from the experiences of Kompenhans [47], Dewhurst [11] and others working in DPIV development. The problem of sub-pixel particle location is similar to that of detecting the centre of the correlation peak in PIV analysis. Gaussian fitting has become the method of choice due to the fact that the particle images themselves can be well represented by a Gaussian intensity distribution and hence its use here.

Once a particle has been selected, the user selects its next image and the resulting velocity vector displayed, figure 3.21, and stored to disk.

The routine was tested with simulated PIV images obtained from the SimPIV software developed by Dewhurst. These numerically generated images have randomly located particles of a specified size. The particles have a Gaussian intensity

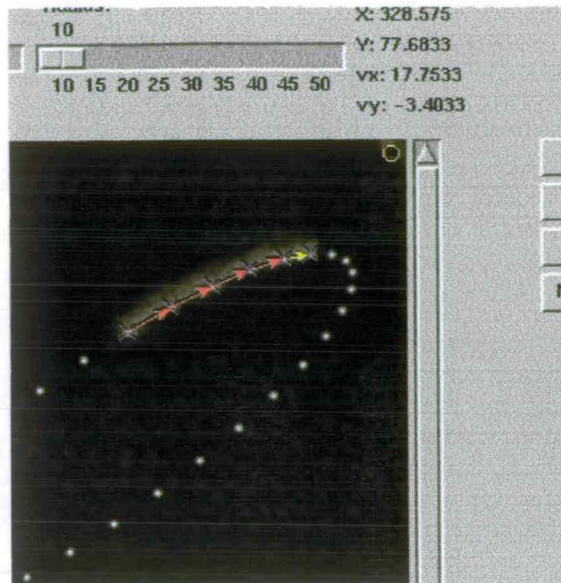


Figure 3.21: Calculated velocity vectors

distribution, where the mean is dependent on the particles randomly allocated location within a pseudo (Gaussian) light sheet. These particles are located on random background noise and thus give images very similar to real PIV images. This idea of numerically generated PIV images has been used by many researchers including Westerweel [94] and Cowen and Monismith [8].

Figure 3.22, of simulated sparsely seeded Poiseuille flow, shows good agreement between the theoretical velocity and that calculated from the PTV software, figure 3.23. The benefit of the sub-pixel fitting is also shown clearly. The results of the same image analysed by autocorrelation PIV are also included to indicate the unsuitability of this method at this seeding density. Poiseuille flow was chosen as later work is concerned with shear flow. Poiseuille flow displays increasing velocity gradient with distance from the centre-line, a condition in which traditional PIV fails (as seen in figure 3.23).

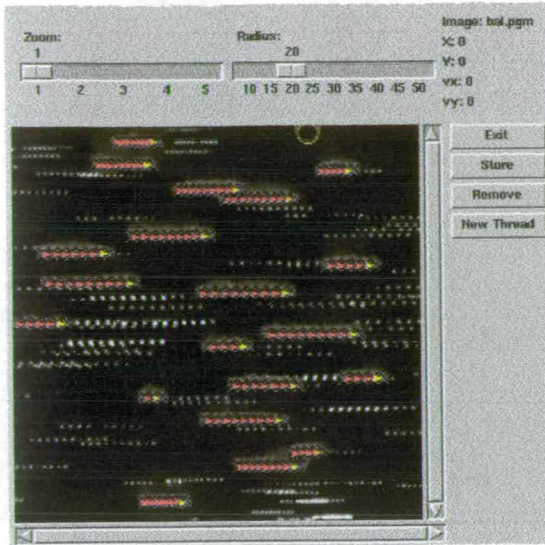


Figure 3.22: Simulated Poiseuille flow with calculated vectors

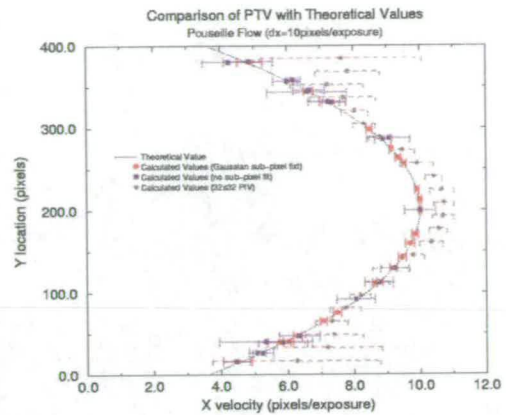


Figure 3.23: Comparison of theoretical and calculated velocities

3.4.3 Future of PTV Development

Obviously it would have been ideal for the software to perform the tracking automatically. This, however, adds two further complexities to the software. Firstly, the software has to be able to identify a particle and distinguish it from its neighbours and background noise. Secondly, the particle must then be tracked from image to image.

Essentially all particle detection algorithms are based on the same concept. This is to make the particles as bright and distinct as possible from the surrounding background and then to locate the centre of each particle to sub-pixel accuracy. In the case of tracking small, dispersed, particles, simple binary thresholding can be used, such as that described by Cowen and Monismith [8]. White pixels neighbouring other white pixels were taken to be the same particle. A sub-pixel algorithm then located the particle's centre. Where the particles are larger and closer packed, a more complex algorithm must be employed such as the radial filter, used by Capart *et. al* [7] in order to distinguish individual particles.

Several ideas have been proposed for the tracking algorithm. The simplest idea is to search an area of increasing radius from a particles previous position. To save computational time, this search can be refined, by searching a smaller area around the particles likely position, calculated from the particles previous trajectory, as used by Capart *et. al* [7].

Keane *et al.* [46] describe a "super-resolution" PIV system. A velocity vector for each particle within an interrogation area could be calculated, rather than just taking the mean. In this way, the routine was far less susceptible to problems relating to velocity gradients, out-of-plane displacements and low seeding densities. They have shown in simulations that spatial resolution can be increased by \sqrt{N} , where N is the number of particles per interrogation area.

Also, in a recent paper by Cowen and Monismith they describe a similar "hybrid" digital particle tracking velocimetry technique [8]. PIV is used to guide a particle tracking routine and in this way they were able to increase the resolution of PIV by up to an order of magnitude, given ideal conditions.

These are not to be confused with experiments of Hirsra *et al.* [31] where they describe a system capable of obtaining PIV results from an area of only $1mm^2$ using an ultra-high seeding density and very high magnification lenses.

A very recent paper by Hering *et al.*[29] utilised a novel particle growing algorithm to track individual particles between exposures. This routine appeared more complex (and thus computationally intensive) than the hybrid technique although may be more suited to tracking individual particles over large time scales.

The author believes that most future PIV /PTV routines will be based around the hybrid idea although unfortunately there was not enough time to implement this concept into the Particle Tracking routines used for this study. It has to be

remembered that DPIV and PTV are both relatively new techniques and their advancement closely follows the technological advances of the equipment on which they depend.

In addition to these developments in Particle Tracking software, there is also on-going research into the seeding used for this type of experiment. The use of fluorescent materials [30] has opened up a range of new particle tracking experiments. In two phase flows (e.g. solids in air), one substance can be chosen to fluoresce. If used in conjunction with the 2-camera system described earlier, a simple colour filter can be placed in front of one of the arrays, enabling the two phases to be separated prior to analysis. Even more exciting possibilities arise from the use of phosphorescent seeding particles. After initial excitation, depending on the material used, these particles can emit light for, up to, minutes. An example use of this concept would be to seed a flow with phosphorescent material and illuminate a small point in space upstream of the measurement zone. The particles that had passed through that point would continue to glow and could be captured on successive frames (or a single frame with the use of a mechanical shutter). The particle's motion could then be tracked from exposure to exposure. Another obvious use would be in the study of mixing, where one fluid is seeded and illuminated prior to the mixing process.

Finally, all ideas presented above relate to advancements in 2D Particle Tracking software. Guezennec *et al.* [27] have presented an idea for 3D particle tracking although the only published results have related to computer generated images.

3.4.4 PTV applied to surface film studies

Previously it had only been possible to perform a statistical analysis of PIV images. A mean velocity could be obtained for small areas of the flow, but not for individual particles. By identifying the same particle from exposure to

exposure it is possible to track the orbital motion of individual surface particles under the influence of a surface film. These results are presented in full in chapter 6.

Thus, using the software written by the author described above, it is possible to obtain velocity information with low seeding densities where these would previously have been unobtainable with conventional PIV. Using the multiple camera DPIV system with fast frame grabbing software it should be possible to record each exposure to separate frames. A *composite* image could be produced for the particle tracking algorithm, however there would now be no directional ambiguity as there would be knowledge of which image came first.

Chapter 4

Image Processing

4.1 Summary

As non-standard techniques were being employed in this study, to obtain any qualitative information from the images obtained, several image processing routines were developed by the author. These included correcting images for geometric distortion and fitting an ellipse to a set of points.

In order to test the validity of the ellipse fitting software, it was also necessary to develop a routine capable of generating simulated images where the exact parameters were known, so these could be compared with those calculated.

Without going into detail of the computer codes involved, this chapter describes the basic mechanisms behind these routines.

4.2 Geometric Correction

The mapping of the original scene to the recorded one, is in general for most PIV systems, not a linear one. Design imperfections in the camera lens, the glass walls of the tank and the precise horizontal and vertical alignment of both the camera and light sheet all contribute to the distortion of the recorded image. Any distortion of the recorded image will effect the particle-pair spacing and the resulting velocity calculation.

The recorded image, $g(x, y)$ can be taken as a function of the original image [96], $f(x, y)$ such that¹;

$$g(x, y) = f(r(x, y), s(x, y)) \quad (4.1)$$

where

$$r = a_0 + a_1x + a_2y + a_3x^2 + a_4y^2 + a_5xy \quad (4.2)$$

$$s = b_0 + b_1x + b_2y + b_3x^2 + b_4y^2 + b_5xy \quad (4.3)$$

If we record a scene where the precise coordinates of elements within the image are known (such as a grid), we can use these to calculate the coefficients of the distortion function. This correction can then be applied to the final calculated velocity or used to correct the images prior to analysis. The latter is generally favoured, since the distortion is likely to induce an apparent velocity gradient and bias the calculation of the mean[11].

Willert [96] suggested correlating a cross (+) with the image of the grid. This would automatically produce a set of exact coordinates which could be compared with those known. Although a routine to *de-warp* the images was implemented by the author, it was highly dependent on the exact alignment of the calibration grid within the light sheet, similar to Willerts findings.

It was generally found that it was better to spend extra time ensuring that the light sheet and camera were perfectly aligned, horizontally, vertically, and precisely parallel, than to correct for it later.

¹Some researchers such as Soloff *et al.* [85] have used higher order polynomials

4.3 Production of Simulated Images

A simple routine was implemented to generate simulated particle images. The centre, size and orientation of the resulting ellipses could be varied in order to test the parameter extraction software described below. The precise location of each Gaussian particle centre was also known to ensure that they were being correctly located. Figure 4.1 is an example of such images.

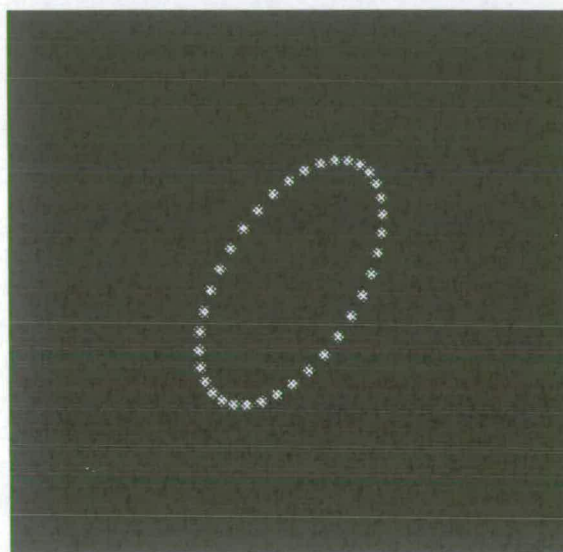


Figure 4.1: Simulated Image

4.4 Ellipse Parameter Extraction by Pseudo Randomised Hough Transform (RHT)

4.4.1 Introduction

One of the most common routines currently used for the detection of shapes (lines, circles, ellipses) within images is the **Hough Transform (HT)**, [53]. The essence of the technique is that points in a binary image space are mapped to points in parameter space from which the original shape can be extracted.

Although this research is concerned with the detection of ellipses in images,

to explain the technique, the simplest case of a binary image containing a single straight line expressed by;

$$y = a_0x + b_0 \tag{4.4}$$

as seen in figure 4.2 shall be described first.

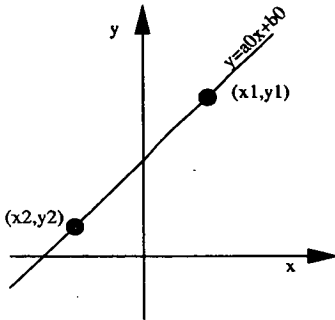


Figure 4.2: Line in image space

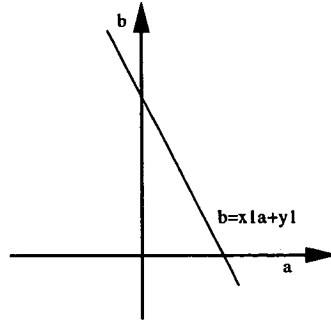


Figure 4.3: Point (x_1,y_1) mapped to line in transform space

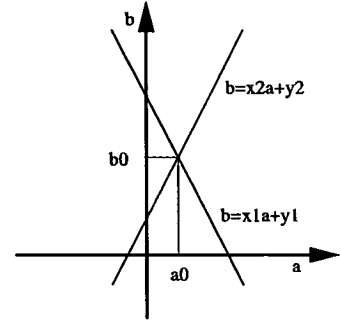


Figure 4.4: Points (x_1,y_1) and (x_2,y_2) mapped to lines in transform space

There are several forms of parameterisation, but using that described by Hough in his original patent application [33] a point in image space, (x_i, y_i) , is mapped onto the line;

$$b = y_i - ax_i \tag{4.5}$$

in parameter space (a, b) . Figure 4.3 shows the point (x_1,y_1) mapped to the line $b = y_1 - ax_1$. This line being all possible combinations of a and b that could give the point (x_1, y_1) .

Taking a second point in image space (x_2,y_2) and parameterising gives a second line, figure 4.4. Again, this line is all possible combinations that could give the point (x_2, y_2) . Since the points were on the same original line, they must

have the same values for a and b . Thus from the point of intersection the values of a_0 and b_0 , the parameters of the original line, are obtained.

Any point (x_i, y_i) taken on our line in image space will pass through the point (a_0, b_0) in parameter space.

4.4.2 Images with more than one line

Extending the previous concept, suppose the image now has two lines, figure 4.5, with parameters $y = -x + 13$ & $y = 4x + 30$ and lengths 9 & 10 pixels respectively.

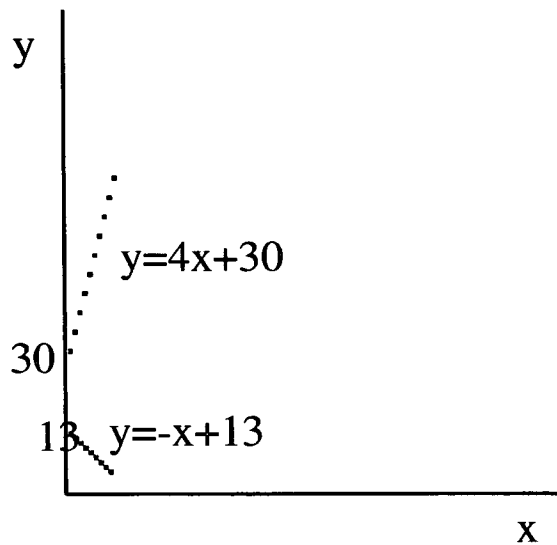


Figure 4.5: Input to Hough Transform

Now, parameter space, \mathcal{P} , is a two dimensional array such that each time a value for (a, b) is obtained, the value of $\mathcal{P}(\cdot, \cdot)$ is incremented by one.

Taking a standard Hough Transform of figure 4.5, each point in the image space, generates a line in \mathcal{P} space. A simple peak detection routine will return the values of a and b for each line in the original image, figure 4.6 (The height of each peak being the length of the original line).

However, generating a line for each point in image space is computationally intensive and it was noted previously that only two points from each line are

necessary to uniquely identify it. Instead of taking every point in image space, two points are selected at random and equation 4.5 solved to obtain a value for a and b .

If points are selected from different lines in image space they map to random values of a and b in \mathcal{P} space while points on the same line will generate the same values.

Repeating this process several times produces 2 high peaks surrounded by lower random peaks. Again, locating the highest peaks will return the original values of a and b , figure 4.7.

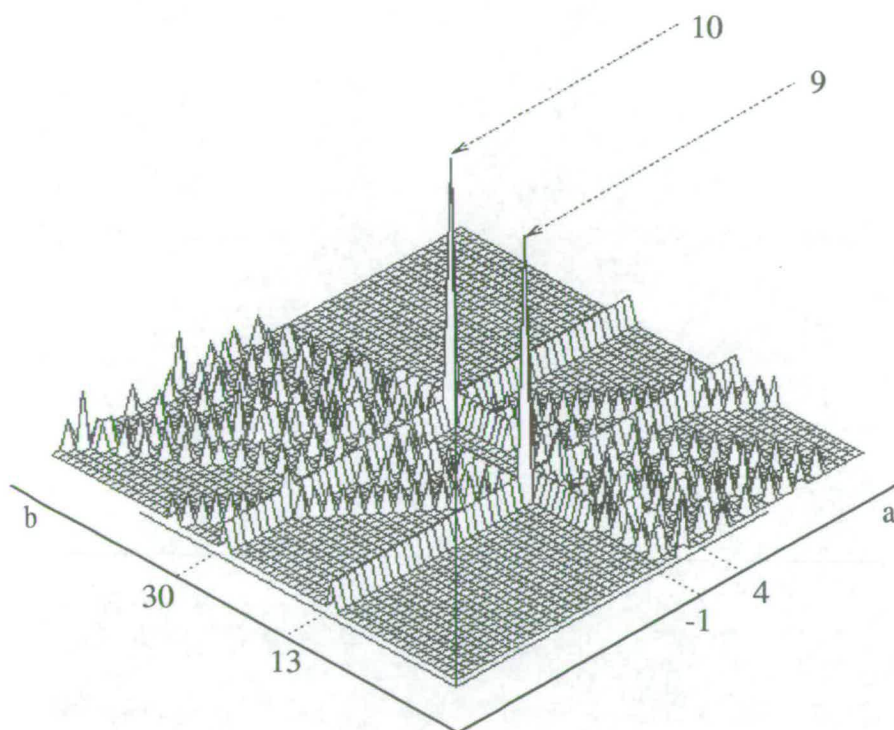


Figure 4.6: Standard Hough Transform

Since only a few points have been selected from the original image, the increase in computational efficiency is quite dramatic. This method is commonly referred to as a **Randomised Hough Transform**.

It is not difficult to see how this concept is extended to the detection of any

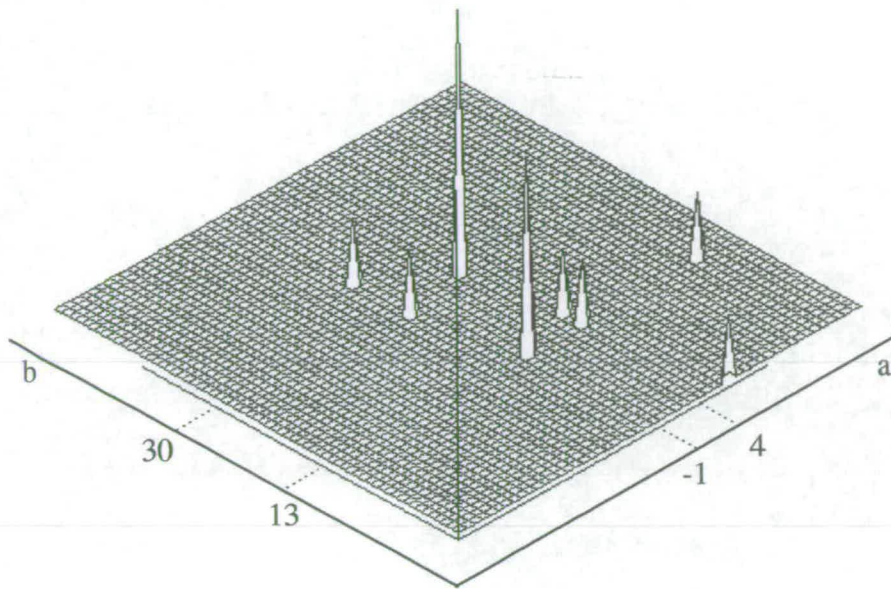


Figure 4.7: Randomised Hough Transform

shape, so long as the shape can be described in terms of a linear equation.

4.4.3 RHT applied to ellipse detection

An ellipse is defined as the solution to

$$a(x - p)^2 + 2b(x - p)(y - q) + c(y - q)^2 = 1 \quad (4.6)$$

where (p, q) is the coordinates of the centre of the ellipse.

To find the unique solution of an ellipse passing through a set of points would require that we solve a set of 5 simultaneous non-linear equations.

In order to solve this practically we make use of a geometrical feature of ellipses to reduce our problem to a linear one.

Suppose we take an ellipse with three points A, B & C . Let $M_{AB}(x_{MAB}, y_{MAB})$ be the midpoint of the chord AB . Taking the tangents of points A and B we find they intersect at a point $I_{AB}(x_{IAB}, y_{IAB})$. According to Yuen [100], the centre

of the ellipse must then lie on the extended line $M_{AB}I_{AB}$ as illustrated in figure 4.8.

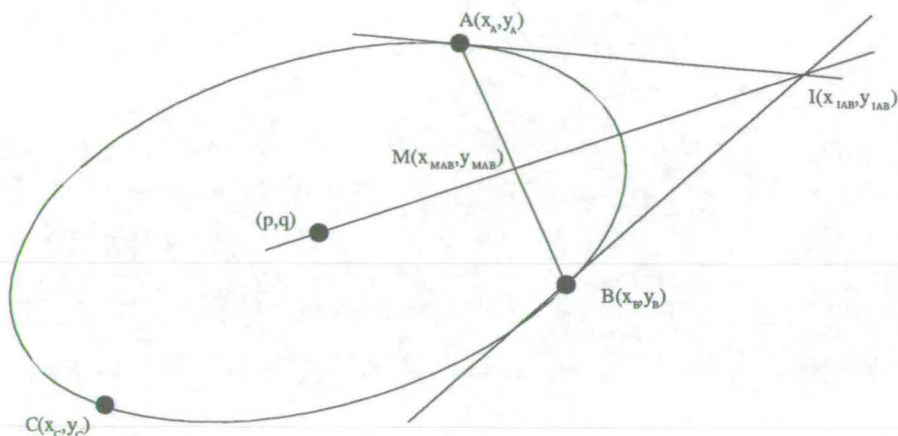


Figure 4.8: Centre lies on line $M_{AB}I_{AB}$.

Repeating this calculation for the points B and C , the centre of the ellipse must lie at the intersection of the lines $M_{AB}I_{AB}$ and $M_{BC}I_{BC}$, figure 4.9.

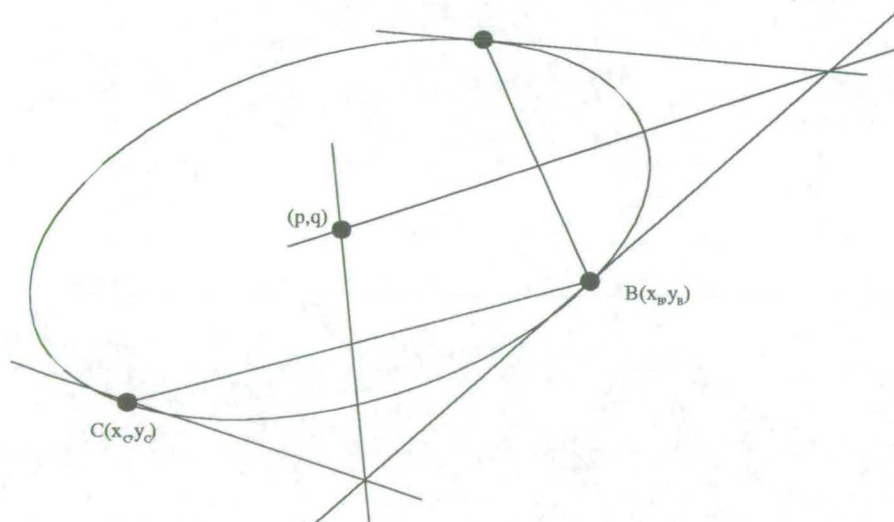


Figure 4.9: Centre lies at intersection of $M_{AB}I_{AB}$ & $M_{BC}I_{BC}$.

The above assumes that points A , B & C have non-parallel tangents as there would be no point of intersection. It is also essential that the gradient of the tangent is not excessively large, as described in section 4.4.5.

Once the centre of the ellipse is located it can be mapped onto one centred on the origin and the original equation is reduced to the simpler case of the general equation of an ellipse,

$$ax^2 + 2bxy + by^2 = 1 \quad (4.7)$$

which is linear with 3 unknowns.

Computationally this becomes the solution of the matrix

$$\begin{bmatrix} x_A^2 & 2x_A y_A & y_A^2 \\ x_B^2 & 2x_B y_B & y_B^2 \\ x_C^2 & 2x_C y_C & y_C^2 \end{bmatrix} \begin{bmatrix} a \\ b \\ c \end{bmatrix} = \begin{bmatrix} 1 \\ 1 \\ 1 \end{bmatrix} \quad (4.8)$$

which is easily solved using the routines of McLaughlin [61] based on Numerical recipes in C [73].

Thus, taking three points on the ellipse, calculating the centre and solving equation 4.8 we obtain a solution for (a, b, c) . It is, however, more useful to convert these to the lengths of the major and minor axes $(r1, r2)$ and the angle from the horizontal of the ellipse (θ) .

This approach is different to that used in other ellipse detection programs such as Nair [66] and Ho [32] where the centre of the ellipse was detected by finding points on the ellipse with parallel tangents. A line between these points must pass through the ellipse centre. However, this method is much more computationally intensive than the method described above.

4.4.4 Actual Implementation

The ellipses that we require to parameterise are actually a collection of discrete points obtained from multiple exposure PIV images of seeding particles on a wavy surfactant covered surface, as can be seen in figure 4.10.

The lack of a continuous ellipse complicates the estimation of the tangential lines. This can be overcome by taking triplet sets of a particle and its nearest neighbours, where the tangent is then taken to be that of a quadratic fitted through each triplet, figure 4.11.

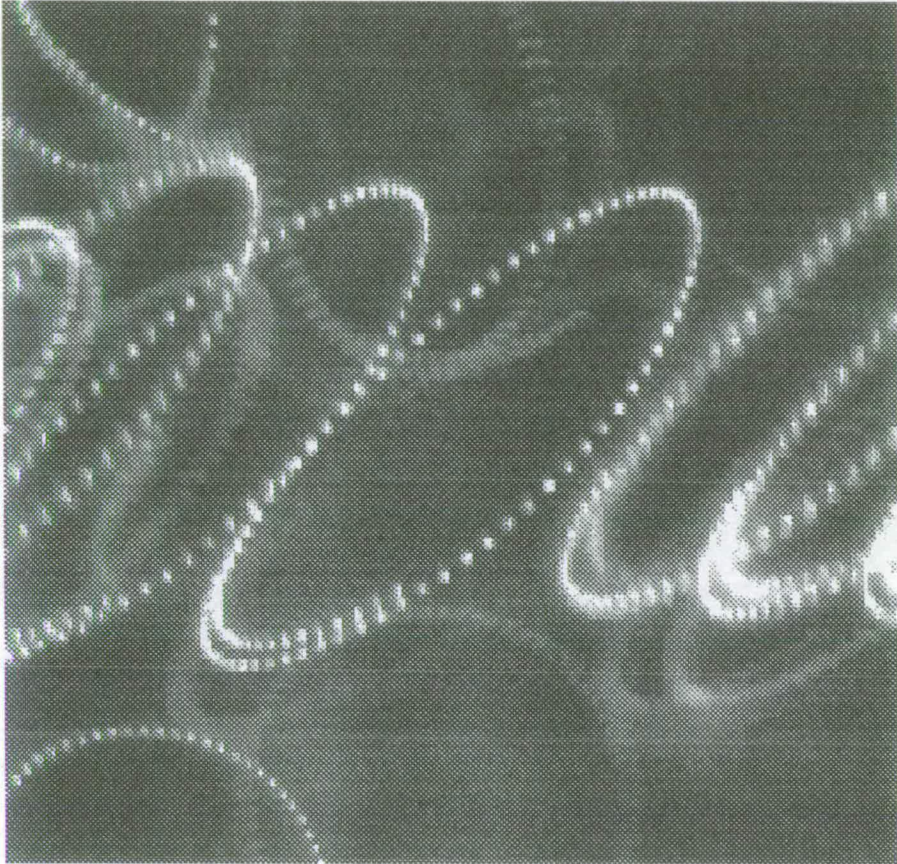


Figure 4.10: Ellipse is actually discrete points

The points are selected from the image using an adaption of the Particle Tracking Routine described in the previous chapter. The same sub-pixel fitting algorithm is used to locate the exact centre of each point to improve accuracy. Simulated images with known coordinates were checked to ensure the precise centre was being located accurately.

The principle of the Random Hough Routine is utilised by the fact that 9 random points (three triplets) are picked from the ellipse and used to calculate its

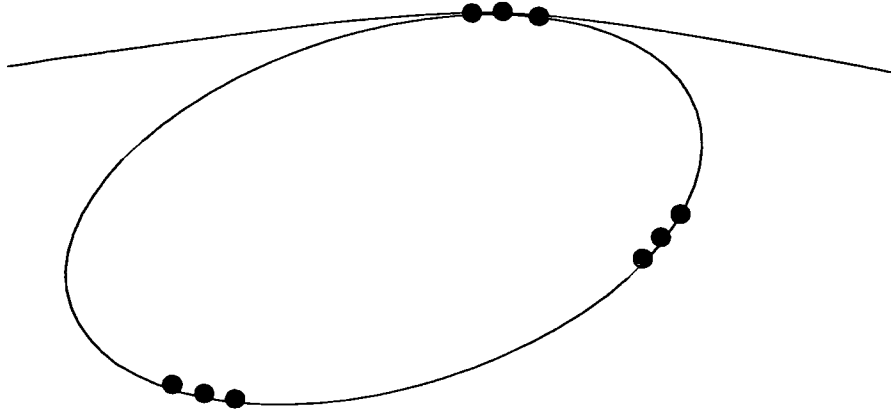


Figure 4.11: Triplet set with fitted quadratic

parameters. This is analogous to the idea of only picking a few random points on a line as described earlier. The ellipse fitting routine was actually found to work with greater accuracy when 4 triplet sets were chosen, thus giving 12 available points. The routine could have been adapted to accept 5 triplet sets, however 4 produced perfectly reliable results and the additional time required for point selection could not be justified. The idea of the Randomised Hough Transform is to use the minimum of information/computation to yield the parameters of the shape under investigation.

Three points are taken at random from the 12 (with no more than one from each triplet set) to which an ellipse is mathematically fitted. The coordinates of the centre along with values for r_1 , r_2 & θ of the fitted ellipse are stored. Since the order in which the points are selected is important, there are 648 ($12 \times 9 \times 6$) possible permutations. This point selection/calculation routine is repeated 1000 times in order for most permutations to be selected without excessive computational time.

At the end of these calculations a mean is obtained for each parameter. Those ellipses with any one parameter exceeding two standard deviations from its mean are discarded which, assuming a normal distribution of calculated values, should

	Centre (x)	Centre (y)	r1	r2	theta
Actual Parameters	125	125	80	40	1.047
Calculated Parameters	124.202	124.892	81.306	38.815	1.047

Table 4.1: Comparison of calculated parameters with original values

remove the worst 5%. This process is iterated until no ellipses are discarded.

This approach is justified by looking at a histogram of the pre-filtered results from applying the technique to a synthesised ellipse of known parameters. As can be seen in figure 4.12, each parameter is reasonably well approximated by a normal distribution about the mean due to the random nature of the errors. This is not quite the case for the parameters $r1$, $r2$ although this is to be expected since the routine is much more likely to calculate too large an ellipse, than too small.

Although the histogram would suggest that a peak detection routine would return the *best fit* ellipse, it has to be remembered that each calculated parameter will generally be unique. To place the values in bins of fixed width, for the purpose of peak detecting, would result in a decrease in resolution.

After filtering, the resulting (mean) ellipse is drawn through the points, figure 4.13 and the parameters stored to disk. Analysing a synthesised ellipse produces results which compare very favourably with the original parameters, table 4.1.

4.4.5 Errors in ellipse calculation

There are three main sources of error in the parameterisation of the discrete points. The first being the assumption that the tangent at a point on the ellipse can be approximated by the tangent of a quadratic through that point and its nearest neighbours. The second is the calculation of the ellipse centre which is a direct result of the calculation of the tangent gradient. And finally the error in the calculation of the actual values of ellipse parameters $r1$, $r2$ & θ .

Histogram of 1000 Ellipses calculated through Points

Actual Ellipse: cx=200, cy=200, r1=100, r2=50, theta=1.05

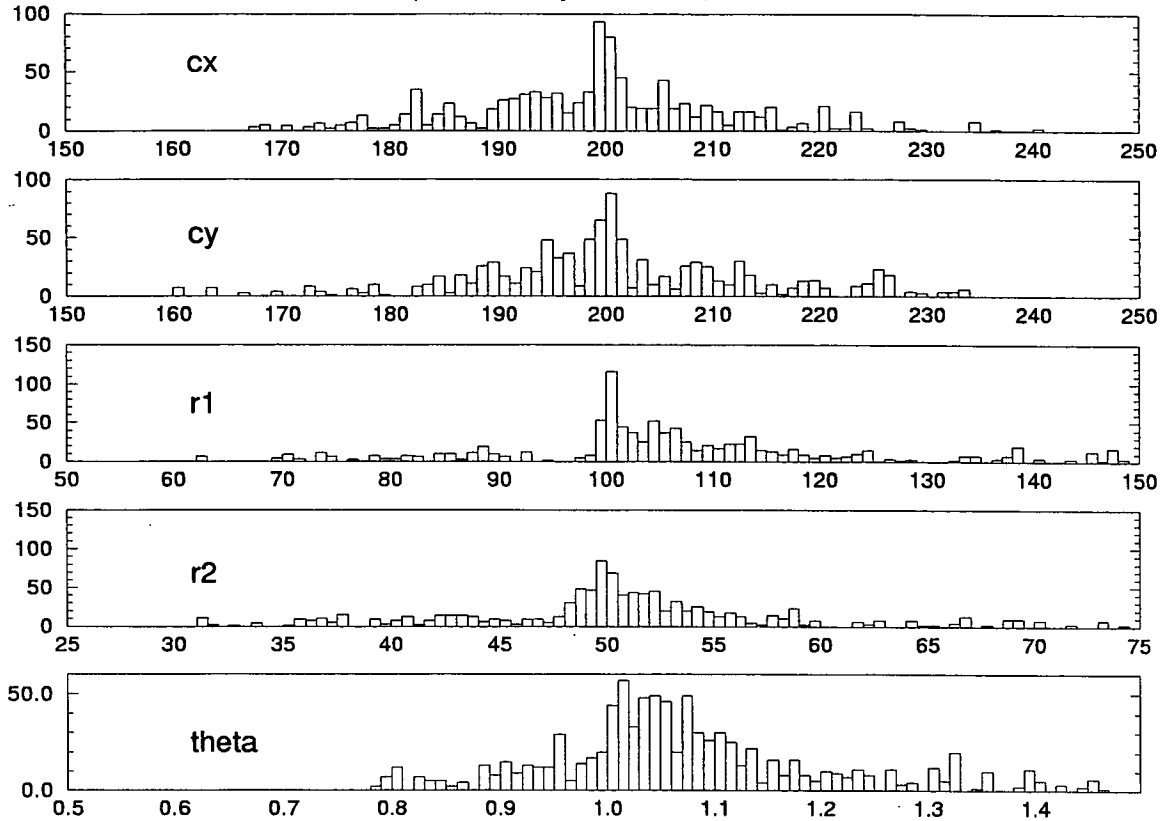


Figure 4.12: Histogram of pre-filtered ellipse parameters

Quadratic Assumption

In order to test the validity that the tangent to an ellipse can be approximated by the tangent to a quadratic fitted to a point and its' nearest neighbours, we note that for a circle (the simplest case), the gradient of the tangent is given by;

$$gradient = \frac{-x}{\sqrt{(r^2 - x^2)}} \tag{4.9}$$

where x is the x-coordinate of the point and r is the radius of the circle. Thus, using the simulation software described above, for each point a comparison of the actual tangent gradient with the calculated one can be made, figure 4.14.

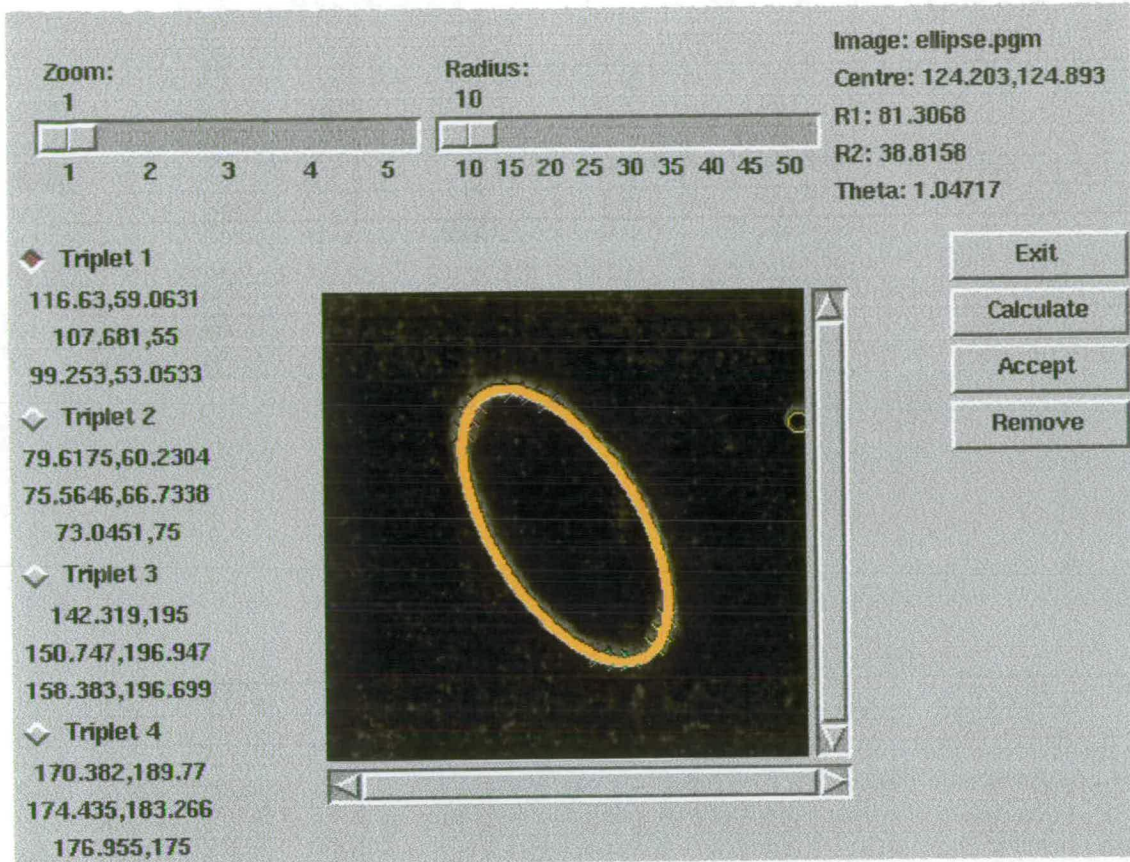


Figure 4.13: Ellipse fitted to points

As indicated, apart from where the tangent gradient tends to infinity, the error is small and the assumption is valid. The real image shown in figure 4.10 has around 60 points (*i.e.* about 6 degrees between points), therefore, assuming points are chosen such that the gradient is not excessive, the calculated tangent will be close to the real value.

Calculation of Tangent

A synthesised, origin centred, ellipse of known parameters was used to determine how errors in the calculation of the tangent gradient effect the computed values for the coordinates of the ellipse centre (cx, cy) . This calculation was performed by directly passing points to the ellipse calculation routine, *i.e.* there was no

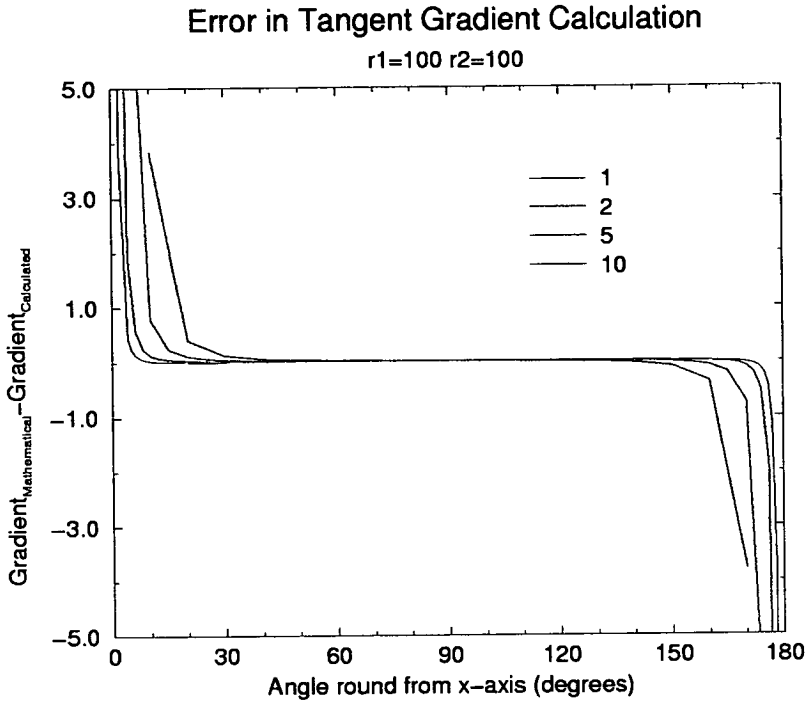


Figure 4.14: Error in calculated tangent gradient. Legend indicates angular separation between points (degrees)

image generated and the manual point selection routine was not used.

The ellipse was computationally rotated through π (in increments of $\frac{1}{1000}\pi$) while the three points remained fixed at $\frac{1}{4}\pi$, $\frac{7}{8}\pi$ and $\frac{14}{8}\pi$, relative to the major axis of the ellipse. (This was the middle point of the triplet with neighbouring points being $\pm\frac{0.1}{8}\pi$). Calculation of the tangent gradient at each point can be seen in figure 4.15.

During the rotation, the tangent gradient calculated at each point will tend towards infinity. A graph of this for one point would be expected to resemble figure 4.16. The reason for this anomaly can be explained as follows. Around the region of infinite tangent gradient, two of the three points will have the same x-coordinate, figure 4.17. The gradient of the tangent is calculated from the coefficients of the fitted quadratic (q_2, q_1, q_0) according to;

Calculation of Tangent Gradient at each Point

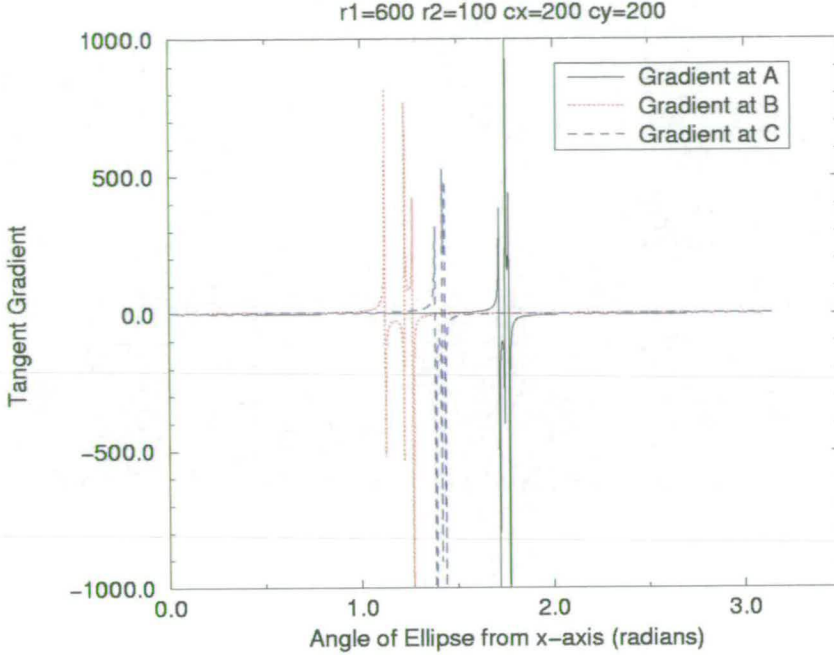


Figure 4.15: Calculated tangent gradient

$$D = (x_2 - x_3)(-x_3 + x_1)(x_1 - x_2) \tag{4.10}$$

$$q_2 = \frac{(x_2 - x_3)y_1 + (x_3 - x_1)y_2 + (x_1 - x_2)y_3}{D}$$

$$q_1 = \frac{-[(x_2 + x_3)(x_2 - x_3)y_1 + (x_3 + x_1)(x_3 - x_1)y_2 + (x_1 + x_2)(x_1 - x_2)y_3]}{D}$$

$$q_0 = \frac{x_2x_3y_1 + x_1x_3y_2 + x_1x_2y_3}{D}$$

$$grad = 2q_2x + q_1 \tag{4.11}$$

Thus each time two points have the same x coordinate, D in equation 4.10 $\rightarrow 0$, therefore the calculated tangent gradient $\rightarrow \infty$, which manifests itself as the triple crossing of the origin seen in figure 4.15.

Non-symmetric triplet sets were used with outside points varying from $\pm \frac{0.1}{8}\pi$ to $\pm \frac{0.5}{8}\pi$ that of the middle point and different values for the location of the centre of each triplet set relative to the major axis but these were found to have

Expected Tangent Gradient

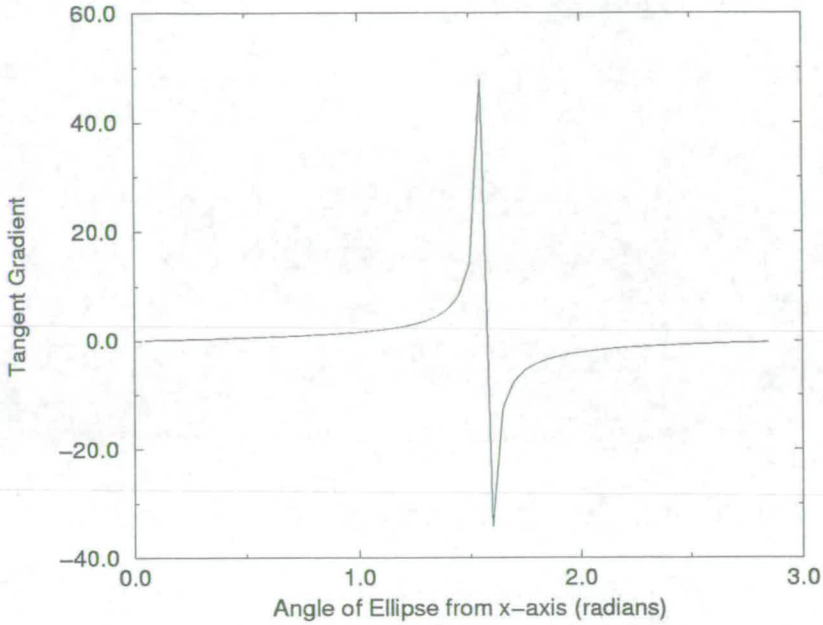


Figure 4.16: Expected tangent gradient

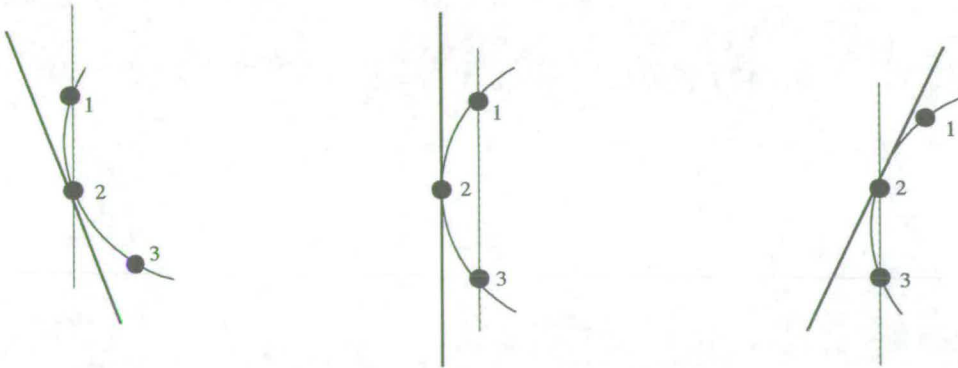


Figure 4.17: x-coordinates identical at high tangent gradient

little effect on the calculation of the tangent.

The significance of an error in the calculation of the tangent gradient is the resulting effect that this has on the estimation of the ellipse centre, figure 4.18. However figure 4.19 shows that, assuming triplets are picked with moderate tangent gradients, the error in centre coordinates is below 2%.

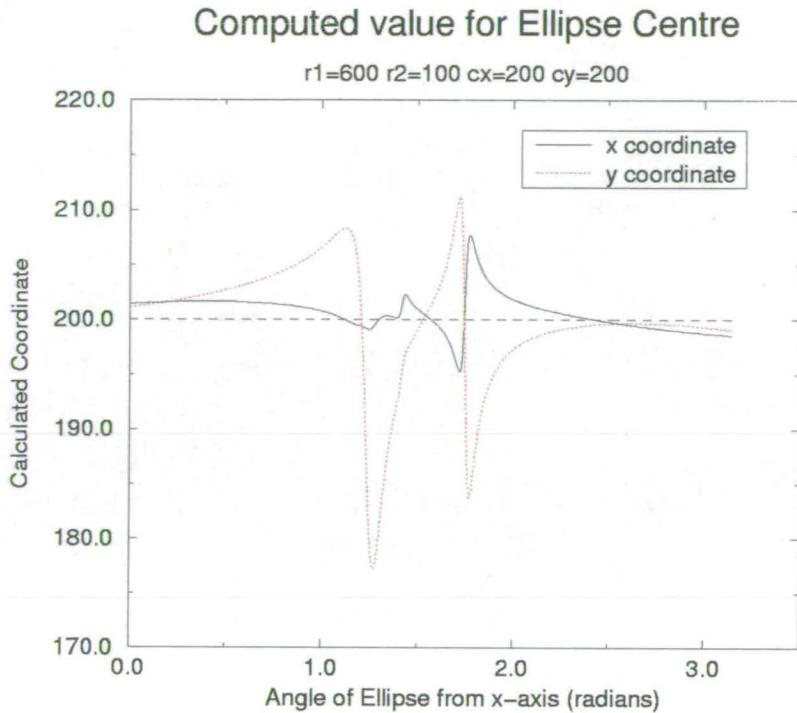


Figure 4.18: Comparison of Calculated centre coordinates with actual coordinates (---)

Error in ellipse parameters

The parameters $r1$, $r2$ and θ were calculated at each stage of rotation. Comparison with known values produced the following results, figure 4.20.

Again, it is not surprising to see that maximum error occurs at the same points where the calculation of the tangent is ambiguous. Generally the percentage error, figure 4.21, in $r1$ and $r2$ is below 2% and θ (the most important parameter for this study) is below 1% indicating that this is a valid technique for estimation of ellipse parameter values.

Point Selection

Analysis of these errors indicates the way in which points should be selected around the ellipse. For the quadratic assumption to be valid, points within a

Percentage Error in Computed value for Ellipse Centre

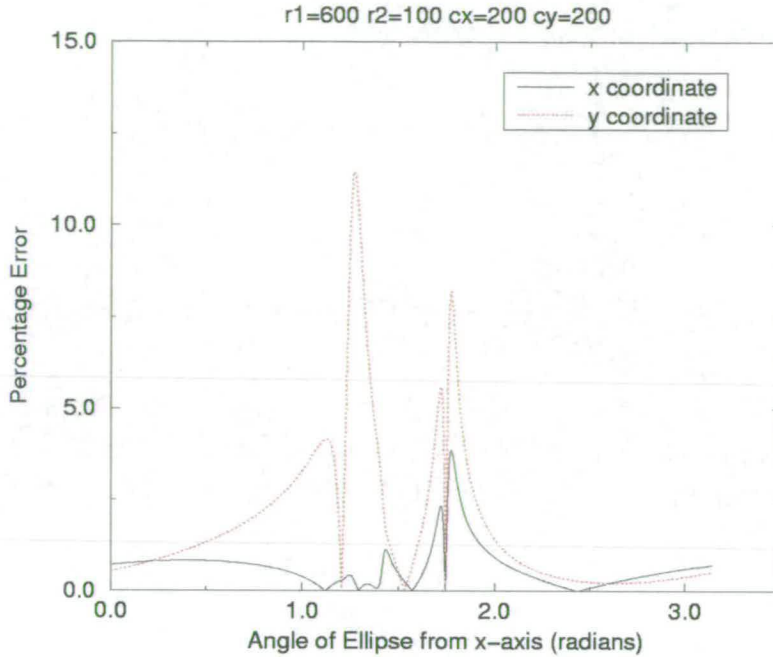


Figure 4.19: Percentage error in calculated coordinates

triplet set should be as close to one another as possible. Care should be taken to avoid selecting triplets where the tangent gradient is likely to be very high. Due to the method of calculating the ellipse centre, it is also necessary to prevent selecting triplets that are likely to have parallel tangents as this will lead to an erroneous point of intersection and thus a resulting error in centre coordinates. Trial and error suggested that the triplets should be located towards the top and bottom of the ellipse as this tended to reduce the likelihood of tangents having parallel gradients. Bearing the above in mind, selecting points sequentially, either clockwise or anti-clockwise, around the ellipse generally produced reliable results. Open-ended ellipses should generally be avoided as these will obviously lead to erroneous results.

4.4.6 Description of title

The word *pseudo* is used in the section title due to the fact that our method is not truly random and in a strict mathematical sense, it is not a transform. Both of these points will be addressed in turn.

Random

Since the ellipse to be parameterised, and the points to be used, are picked by hand to certain criteria, the method cannot be regarded as truly random. This approach was taken to reduce the initial programming time and to add a certain element of *quality control* to the process. However, apart from the addition programming effort required, there is no reason that the entire ellipse detection routine could not be completely automated with points being picked at random from image space.

Transform

In a strict mathematical sense, the mapping of pixels to ellipse parameters is not a transform, due to the fact that this process is irreversible. *i.e.* you could not map the fitted ellipse back to the original discrete points [53].

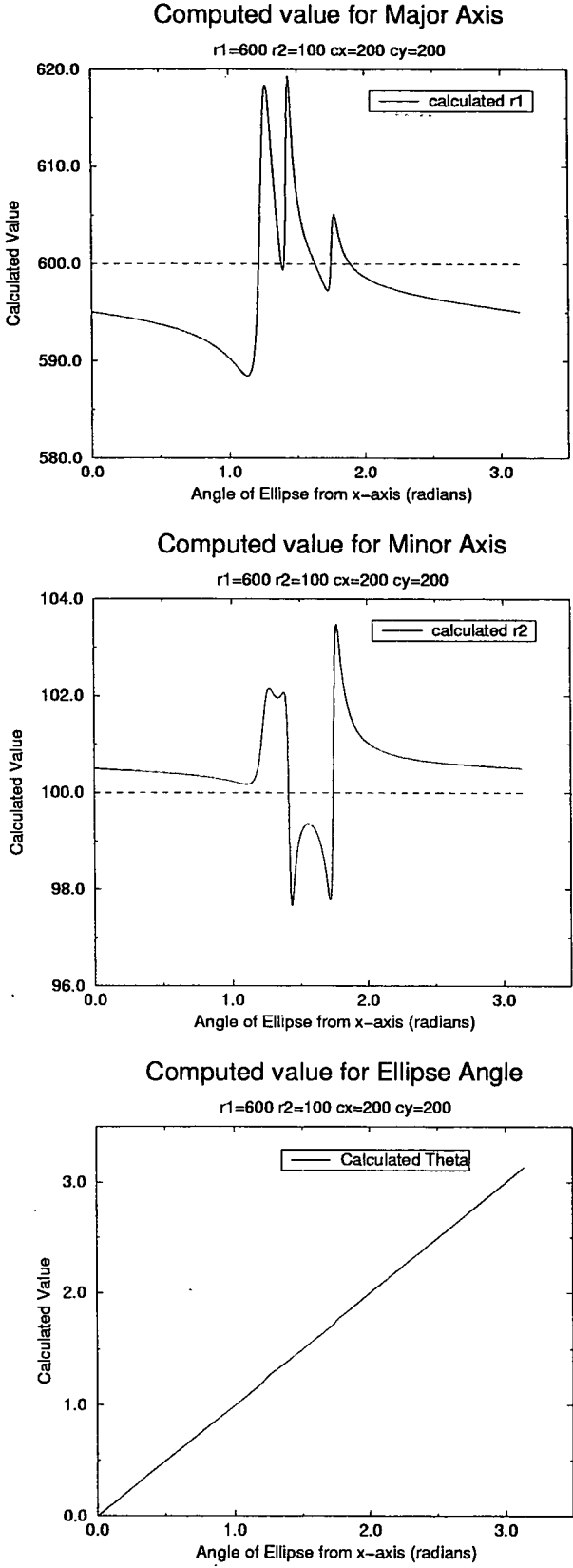


Figure 4.20: Comparison of calculated ellipse parameters with actual parameters (- -)

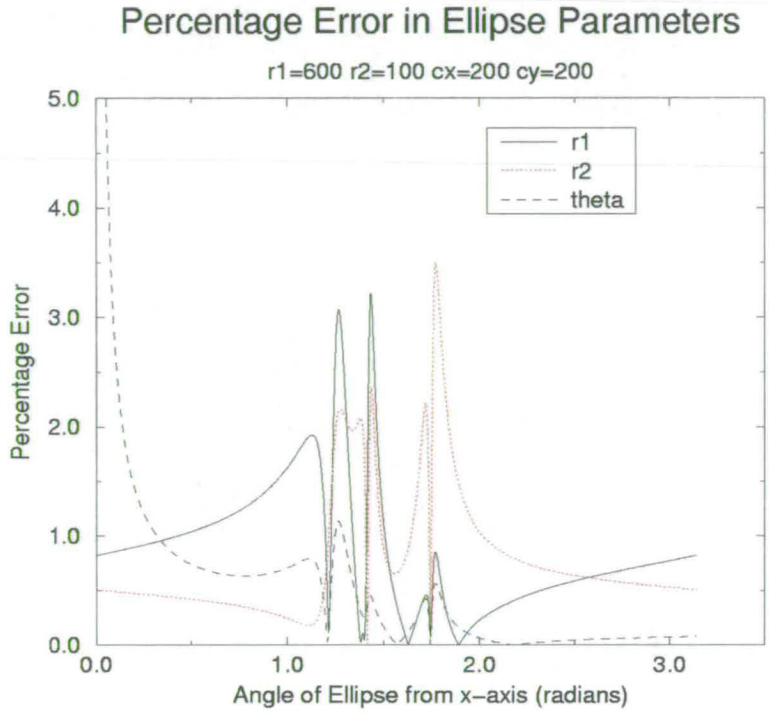


Figure 4.21: Percentage error in ellipse parameters

Chapter 5

Results 1 - Effect of Surface Films on Wind Generated Waves

5.1 Summary

A series of experiments was performed in the wind-wave facility (described in section 2.2) to observe and measure the effect of a surface active film on wind-induced waves. The general characteristics of the wind-induced waves and the final results were found to be in good agreement with current theoretical predictions.

5.2 Introduction

The *Green Tank* is in constant use and available lab time is limited. For this reason and the sheer physical size of the tank, only films that were *self cleaning* were to be considered. Hand Soap¹ was chosen as the film to study as it is strongly surface active, inexpensive and readily available. Above all, it quickly mixes with the bulk fluid leaving the surface, in effect, clean for future experiments.

It is not thought that mixing a fraction of a millilitre of soap into over 3000 litres of water will greatly effect the bulk characteristics. The measurements described below, indicate that the wind waves return to the same state after the soap has mixed sufficiently.

¹See Appendix A for chemical composition

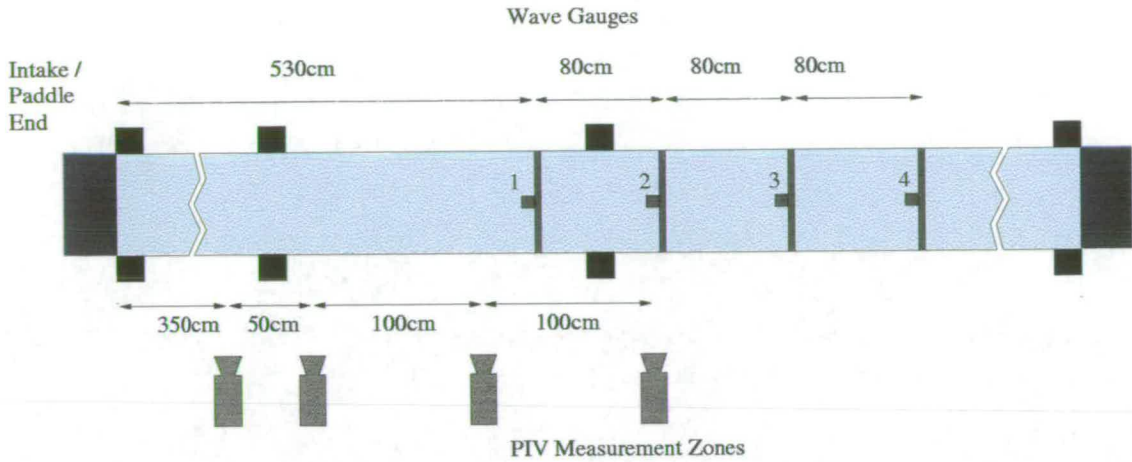


Figure 5.1: Location of wave gauges and PIV Measurement Zones

A series of PIV experiments using the 2-camera system described in section 3.3.5 and wave gauge readings were used to quantitatively measure the change in frequency and amplitude of the generated waves in the presence of the surface film.

5.3 General Characteristics of Laboratory Wind Generated Waves

In order to measure the effect of the film, it was first necessary to fully characterise the undisturbed wave field. Four locations down the tank were chosen to take PIV and wavegauge measurements. The location of these was largely dictated by mounting brackets (gauges) and optical access (PIV), figure 5.1. During all the PIV and wavegauge measurements, the fan was run at its maximum speed producing a mean centreline wind velocity of approximately 5.36ms^{-1} . The wind-induced wave pattern was generally allowed to become fully developed before any measurements were taken.

Camera	2 × Pulnix 9701
Vertical Resolution	484 pixels
Horizontal Resolution	768 pixels
Lens	Nikkor 50mm 1:1.4
f number	2.8
pixels/particle	2-3
Δt	0.0078125s

Table 5.1: Experimental Parameters

5.3.1 DPIV Measurements

The camera parameters were initially optimised according to the recommendations of Adrian [2] and slightly adjusted by trial and error to maximise the number of valid vectors, table 5.1.

The 2-camera system was positioned at each of the locations depicted in figure 5.1. Twenty double images were obtained at each location. All the images were obtained in as short a time as possible to prevent the return flow along the base of the tank from generating turbulence which would interfere with the results. Between each location the tank was allowed to settle with the fan switched off. The waves were allowed to develop fully before any results were taken. In all cases the camera was positioned 50cm out from the glass wall of the tank, just below the still water level. After a single pair of images had been obtained it was quickly analysed to ensure it yielded valid vectors. The remaining 19 pairs were saved directly to disk for future processing.

Each pair of images were subsequently analysed by crosscorrelation, a typical vector map for each location is presented in figures 5.2 - 5.5. Additionally the maps are superimposed on the vorticity, w , calculated from [88]:

$$w = \frac{dv}{dx} - \frac{du}{dy}, \quad (5.1)$$

where u and v are the velocities in the x and y directions respectively. The vorticity is presented as the coloured background and legend purely to aid the eye in the interpretation of the vector maps.

At low fetch, figure 5.2, the wind-induced wave motion is small and penetrates only a few millimetres into the bulk. The general flow is in the horizontal direction. As fetch increases, both the magnitude of the wave induced motion and the depth of penetration increase. At the maximum fetch, figure 5.5, the wave motion is such that it has begun to induce vortices in the bulk. No longer is the motion only in the horizontal direction and a large vertical component exists well below the surface.

As noted by Wang and Wu [91] the velocity is actually a superposition of the mean motion, the wave orbital motion and the turbulence motion. They were also aware that, while it is conceptually simple to separate these components, practically, it is quite difficult. Although the mean can be easily calculated and subtracted, it requires advanced analysis such as the Triple Decomposition Method of Magnaudet [60] to separate the other two components. This technique, however, was beyond the scope of this study.

Most of the results presented here will be root-mean-squared (RMS) values of velocity. These have been calculated from all twenty PIV images taken at the same location. In general a value has been calculated for each vertical interrogation area (depth), averaged over all images and horizontal interrogation areas. In this way we obtain a general picture of the flow characteristics.

The velocity profile beneath gravity waves propagating in deep water on a film-free clean surface is given by [50]:

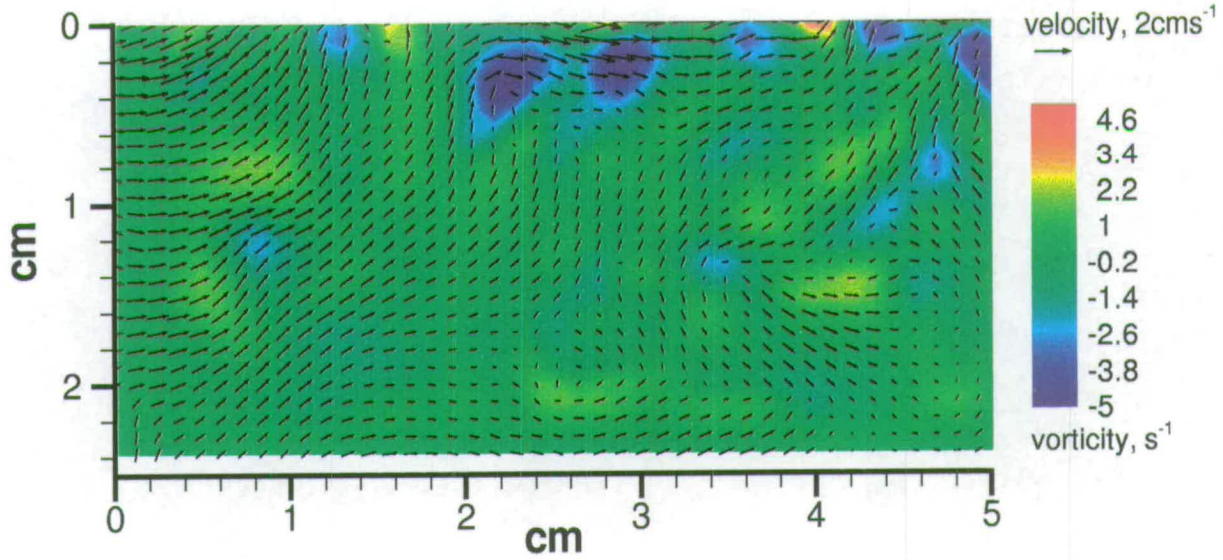


Figure 5.2: Typical Vector and Vorticity Map - 3.5m

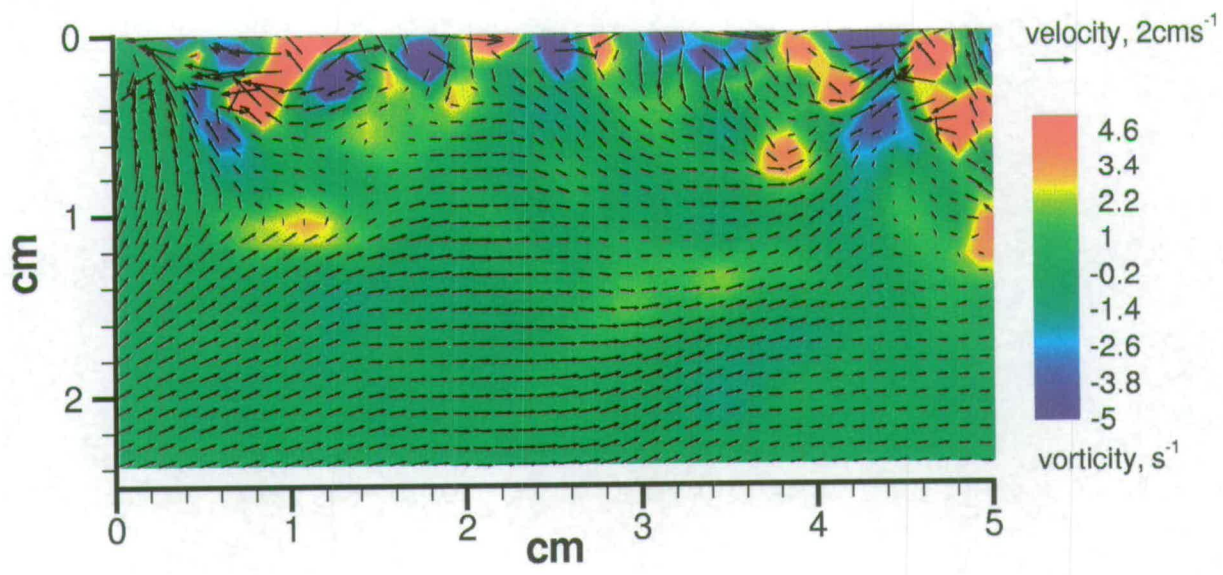


Figure 5.3: Typical Vector and Vorticity Map - 4m

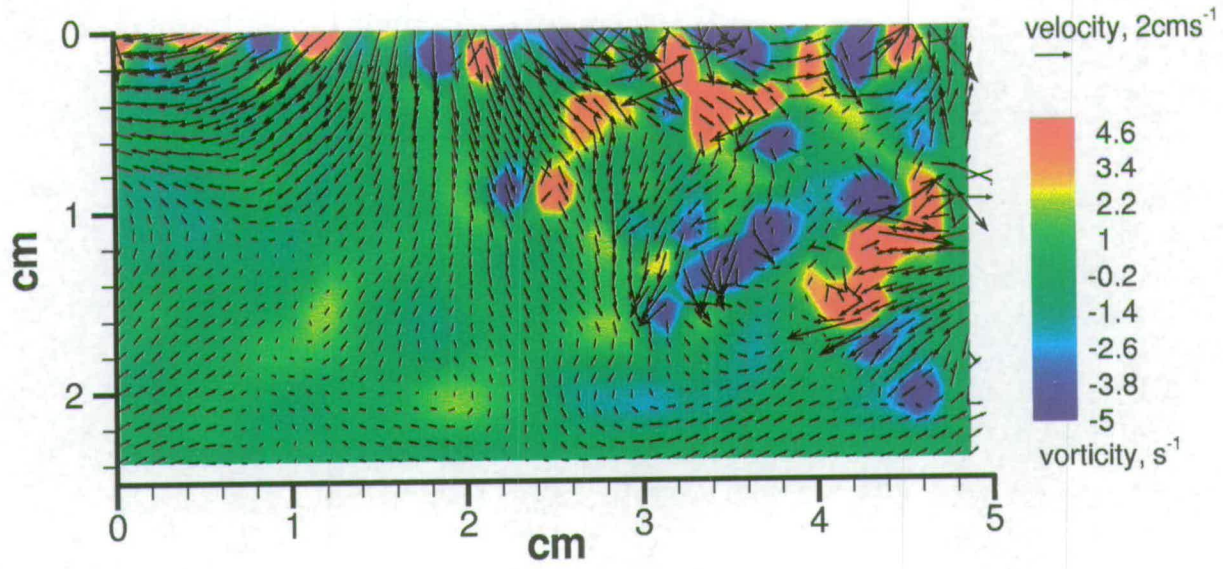


Figure 5.4: Typical Vector and Vorticity Map - 5m

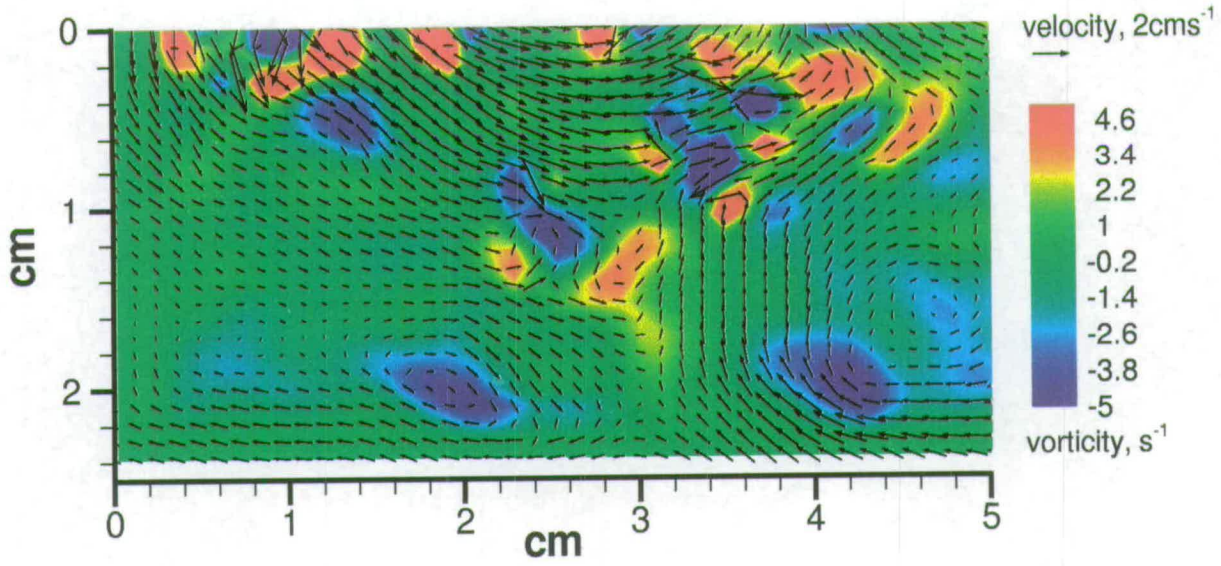


Figure 5.5: Typical Vector and Vorticity Map - 6m

$$u = Ake^{-ky} \sin(kx - \omega t) \quad (5.2)$$

$$v = Ake^{-ky} \cos(kx - \omega t) \quad (5.3)$$

$$A = \frac{a\omega}{k}, \quad (5.4)$$

where a is the amplitude, k the wavenumber and ω the frequency of the wave. Thus, both the vertical and horizontal velocity diminishes exponentially with depth. Measurement of the velocity profile beneath the wind-induced waves for a range of wind speeds, figures 5.7 and 5.6 reveals several interesting features:

- At low wind speeds where no visible waves exist, there is virtually no vertical velocity component and only the wind-induced horizontal surface drift is evident. What little vertical velocity exists is associated with the general turbulent motion in the tank.
- As the wind speed increases, there is no change in the vertical motion while the magnitude and depth of the shear layer increases. These results are consistent with the idea of a *critical wind velocity*, described in section 1.4.
- Above this wind speed, waves begin to appear with the resulting increase in vertical velocity component.
- As the wind speed increases, the velocity profiles begin to resemble the exponential profile suggested by equation 5.3. The dashed lines in the vertical velocity profile are exponential fits to the data. The same lines have been superimposed on the horizontal data to demonstrate the extent to which the wind induced shear modifies the expected profile.

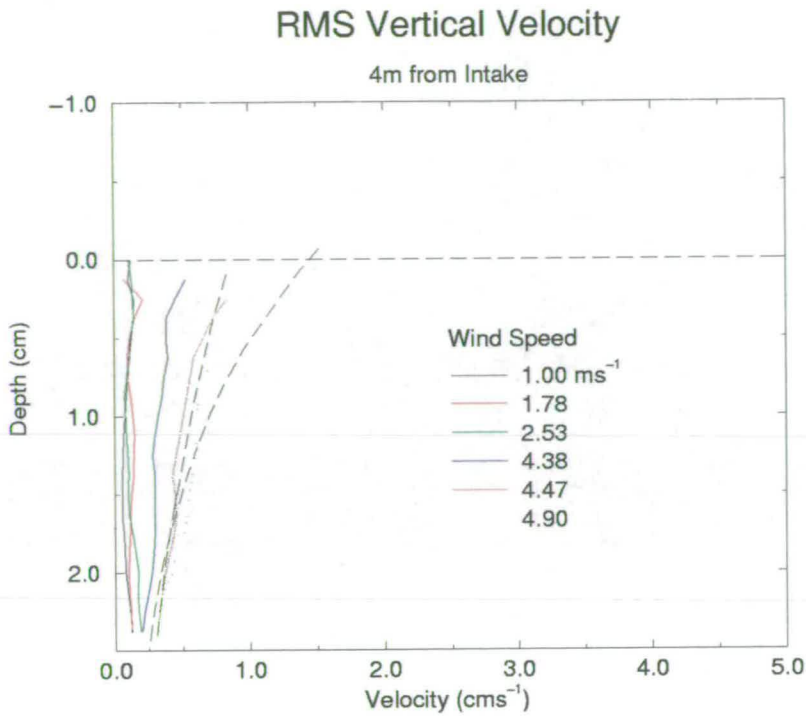


Figure 5.6: RMS Vertical Velocity with exponential fit (- - -). Wind Speed 5.36m.s^{-1}

5.3.2 Wave Gauge Measurements

While raw wavegauge results could be used to obtain the amplitude of the waves, it is of greater benefit to Fourier Transform these time series measurements into frequency spectra. In this way, the dominant frequencies present in the wind-induced wave field could be observed.

Frequency Analysis

Figure 5.8 displays the main spectral components of fully developed laboratory-generated wind waves. Those closest to the intake, *i.e.* smallest fetch, have a higher peak frequency than those further downwind, *i.e.* greater fetch. This is exactly what we would expect as it is the small, high frequency waves which combine together to create the larger, low frequency waves. It is also clear that

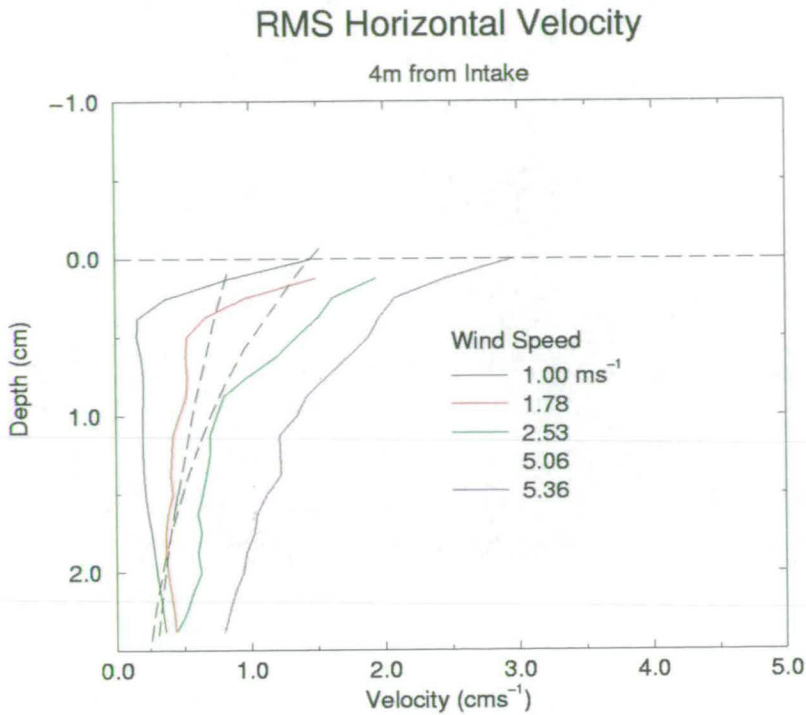


Figure 5.7: RMS Horizontal Velocity with exponential fit (- - -). Wind Speed 5.36ms^{-1}

the high frequency component is virtually identical at each gauge, indicating that ripple formation is uniform over the entire tank.

In fact, Phillips [71] suggested that the high frequency components were independent of fetch and proposed an empirical law based on the field measurements of Burling [6];

$$\Phi = 7.4 \times 10^{-3} \times g^2 \times \omega^{-5} \tag{5.5}$$

where Φ is the wave spectrum. This is in good agreement with the spectrum of the waves recorded here, figure 5.9 where Philips theory is given by the dashed line (- - -).

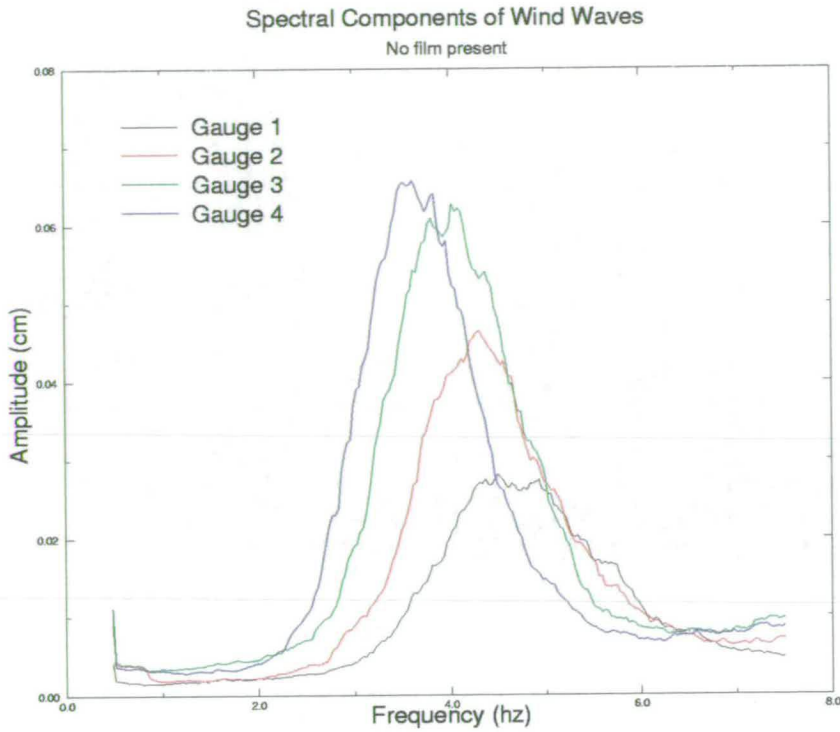


Figure 5.8: Spectral components before the film is applied. Wind Speed $5.36ms^{-1}$

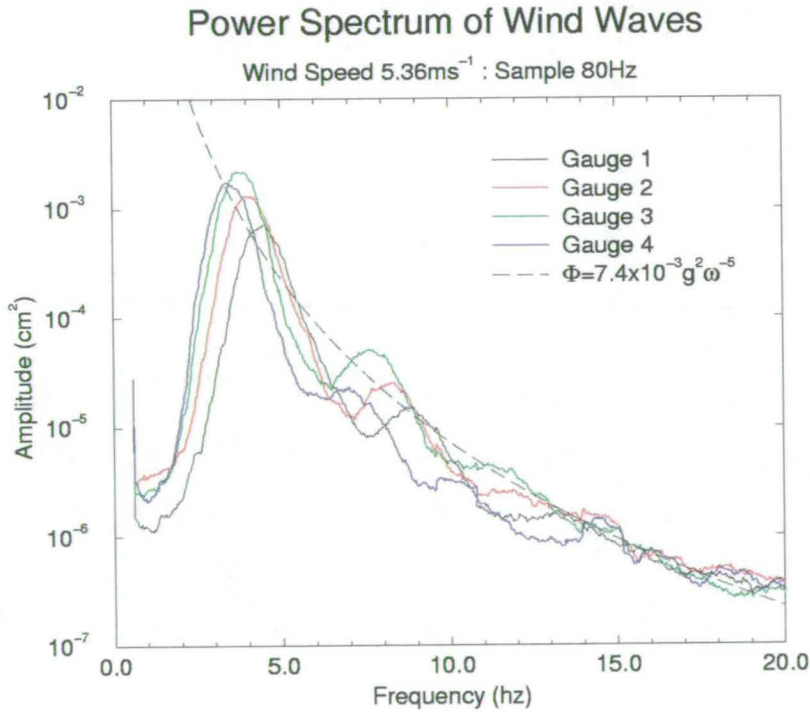


Figure 5.9: Comparison of Phillips Theory (---) and experimental results

5.4 Damping of Wind Generated Waves by Hand Soap

All of the following results were obtained with the fan running at its maximum speed producing a mean centreline wind velocity of approximately 5.36ms^{-1} . Again, the wind-induced wave pattern was generally allowed to become fully developed before any measurements were taken. A single drop of the surfactant, hand soap² was added by syringe to the water surface, 1m from the intake.

As the film spread, the area of water upwind of the film front became perfectly flat. This continued until the film had spread to cover the entire tank. Though the surface was smooth, there was still considerable surface drag causing a strong shear layer. Analysis by PIV, figures 5.18-5.22, display the magnitude and extent of this layer. This actually served to *wipe* the film off the surface. Around 2 minutes after the film was added, the waves began to form again and the tank returned to its pre-film state.

5.4.1 DPIV investigation of wind wave damping

Several PIV images were taken at each location. Figures 5.10-5.17 detail the change in horizontal and vertical velocity between the no-film and film case.

Figure 5.10 actually indicates that near the surface the horizontal velocity increases. This is due to the fact that at this fetch, the wave-induced orbital motion is minimal and the film allows a strong shear layer to establish. Figure 5.11 shows that what little wave-induced vertical motion there is, disappears completely. The remaining vertical velocity is the residual turbulent motion in the tank which, as displayed, is independent of depth.

The exponential profile is beginning to be established at 4m, figures 5.12 and

²See Appendix A

5.13. Also, as expected, the vertical motion decreases dramatically in the presence of the film to around the same *background* value as the 3.5m case.

The horizontal velocity continues to approximate to the expected exponential profile, although modified by the wind induced drift, figures 5.14 and 5.16. For the 6m case, the surface drift in the presence of the film is smaller than expected, presumably caused by some interaction with the end of the tank or the foam absorber.

As fetch increases, so too does the magnitude of the wave-induced vertical motion and the depth to which it penetrates, figures 5.15 and 5.17. Again, in the presence of the film, all vertical motion is suppressed and the residual turbulent component is of the same magnitude as the 3.5 and 4m cases.

Additionally, close up images were taken at 4m from the intake to detail the change in RMS horizontal and vertical velocity as the film enters the measurement zone, figures 5.18-5.22. The hand soap was added to the water surface 1m from the intake at 0s. Before the film reaches the zone (8s), both the horizontal and vertical profiles resemble the expected exponential curve, decreasing in magnitude with depth. As the film spreads, the waves become smaller, observed as a drop off in both components (10-12s). The film is just entering the zone during the measurement taken at 13s. At this point, the strong horizontal surface drift is just beginning to establish. The completely film-covered cases (14s, 15s) display very little vertical motion and, the now fully established, horizontal surface drift.

There are several explanations for the strong surface shear. It could be argued that the initial shear is due purely to the spreading of the film and that the residual shear is an inertial effect. While to some extent this will be true, the author believes that the observed shear is due to the wind dragging the surface downwind. The measurements suggest that the shear velocity is constant with

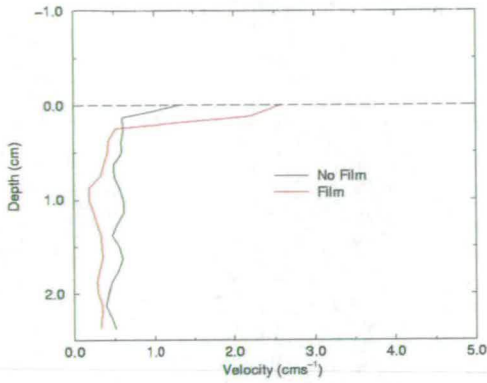


Figure 5.10: RMS V_x - 3.5m

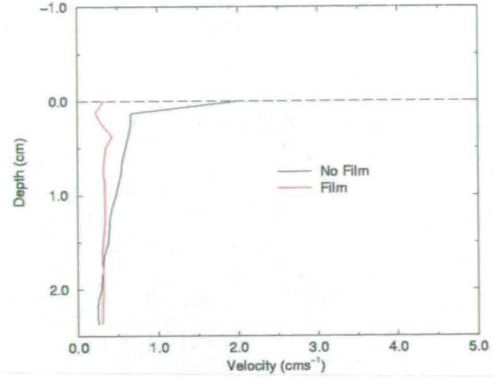


Figure 5.11: RMS V_y - 3.5m

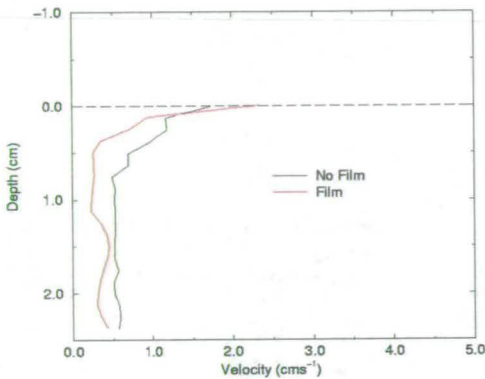


Figure 5.12: RMS V_x - 4m

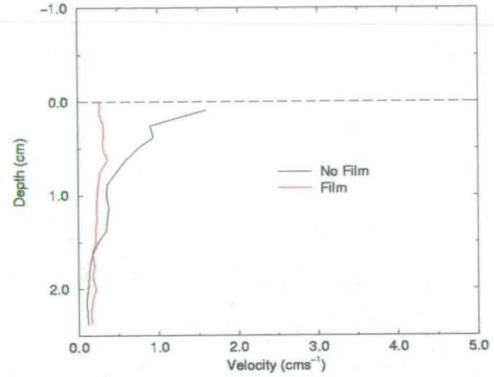


Figure 5.13: RMS V_y - 4m

time, figures 5.21, 5.22, and not decaying as you would expect if it were an inertial effect. Although not presented in the results, the strong shear is visually observed to last for several minutes, right up until the point where the waves re-appear. The shear appears constant across the width of the tank although this was not possible to measure due to the location of the scanning beam box.

Lange [51] collated many observations of wind induced surface drift for wind speeds ranging from $2-12\text{ms}^{-1}$. Most observations calculated the drift to be around 2-5% of the mean centreline wind velocity. These results indicate a surface drift velocity of just over 15cms^{-1} which is approximately 3% of the wind velocity

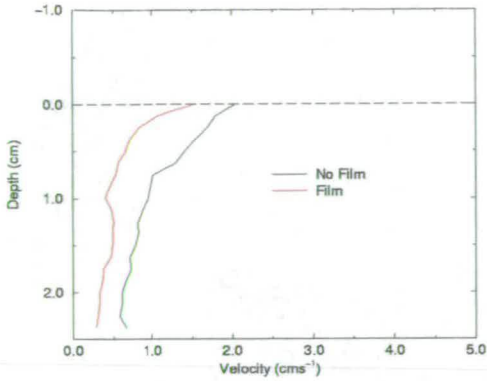


Figure 5.14: RMS V_x - 5m

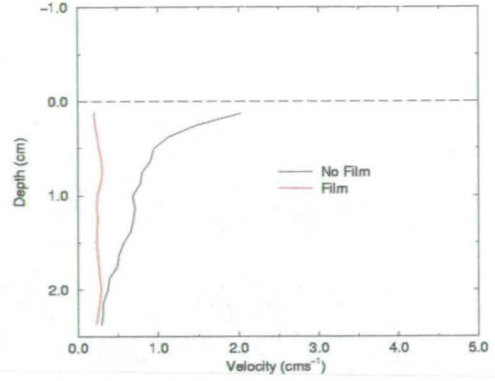


Figure 5.15: RMS V_y - 5m

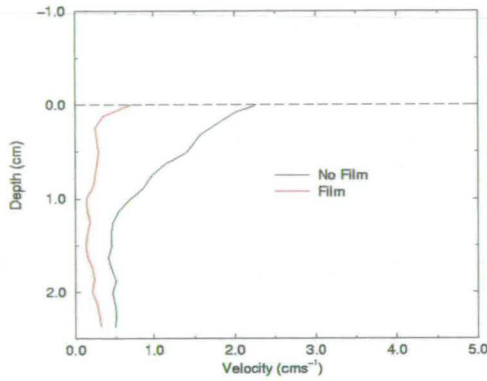


Figure 5.16: RMS V_x - 6m

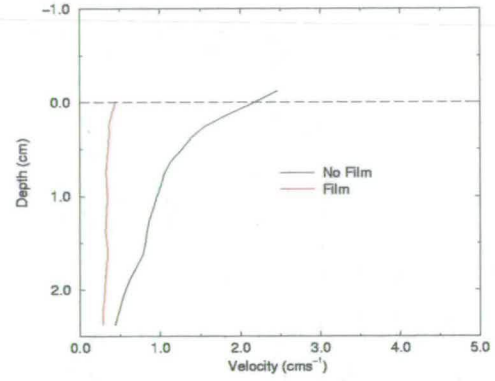


Figure 5.17: RMS V_y - 6m

($5.36ms^{-1}$).

The slight vertical velocity that does exist again is the residual turbulent motion in the tank. This is also present in the horizontal component although there is also an additional component due the recirculation in the tank. Due to the closed nature of the tank, water pushed along by the surface drift returns along the bottom. Very quickly a tank-deep circulation establishes. As can be seen however, in the measurement zone, the magnitude of this motion is constant with depth.

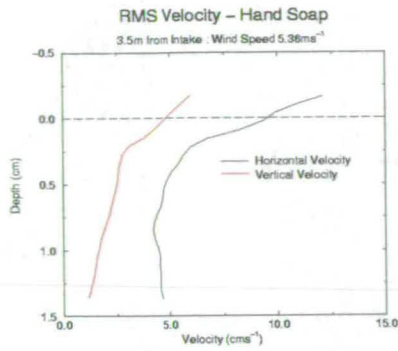


Figure 5.18: 8s after film added

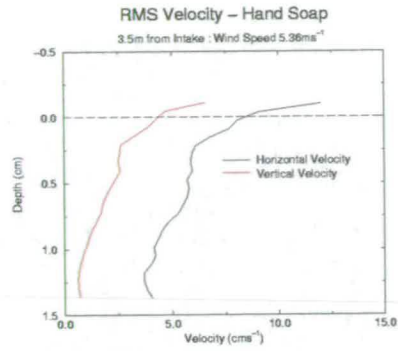


Figure 5.19: 10s after film added

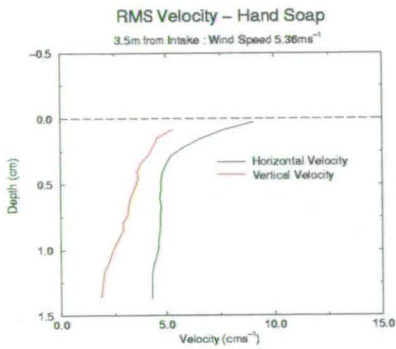


Figure 5.20: 13s after film added

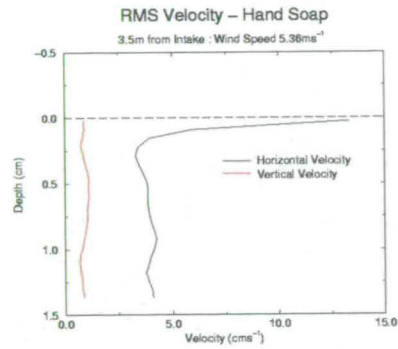


Figure 5.21: 14s after film added

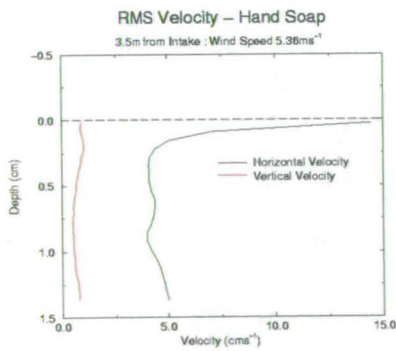


Figure 5.22: 15s after film added

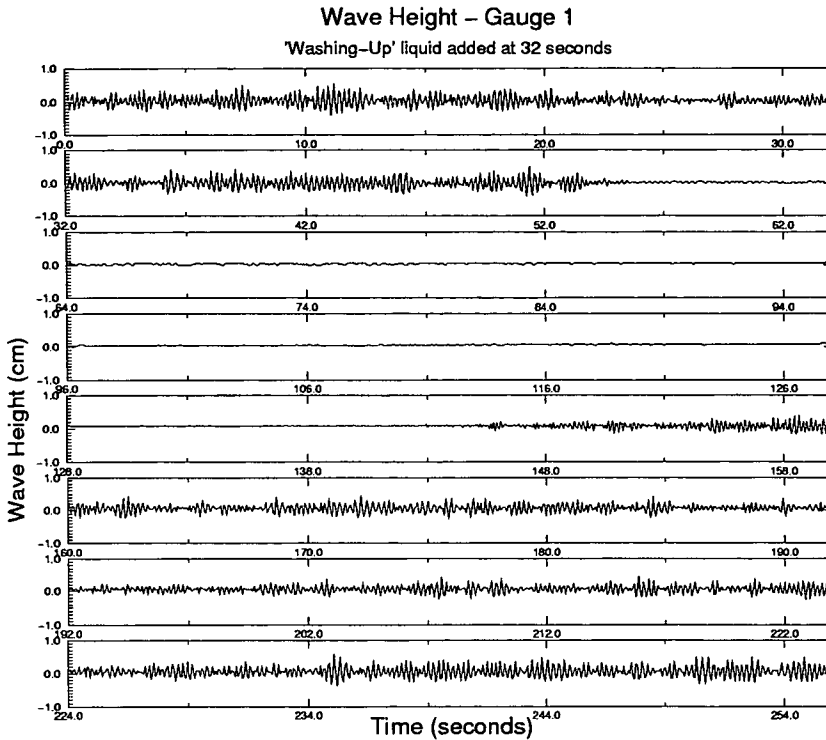


Figure 5.23: 4 Minute record of wave amplitude at Gauge 1

5.4.2 Wave Gauge investigation of wind wave damping

Simultaneously, 4 capacitance wave gauges, described in detail in section 2.2.4, were sampled. Figures 5.23 to 5.26 record the entire passing of the film from addition to complete disappearance, The sampling frequency of the wave gauges was reduced to 16Hz to allow a recording time of just over 4 minutes. This lower sampling rate was justified by reference to the experiments of Mitsuyasu *et al.* [63] where, with similar equipment and apparatus they found the dominant frequency of wind waves to be in the range 0-4Hz. The central section of each trace clearly shows the period where the film had completely damped all waves.

Analysis of the wave gauge records reveal several interesting features:

- The maximum wave amplitude as the film spreads displays a strong variation at each of the gauges, figure 5.27. Gauge 1 (furthest upwind) displays

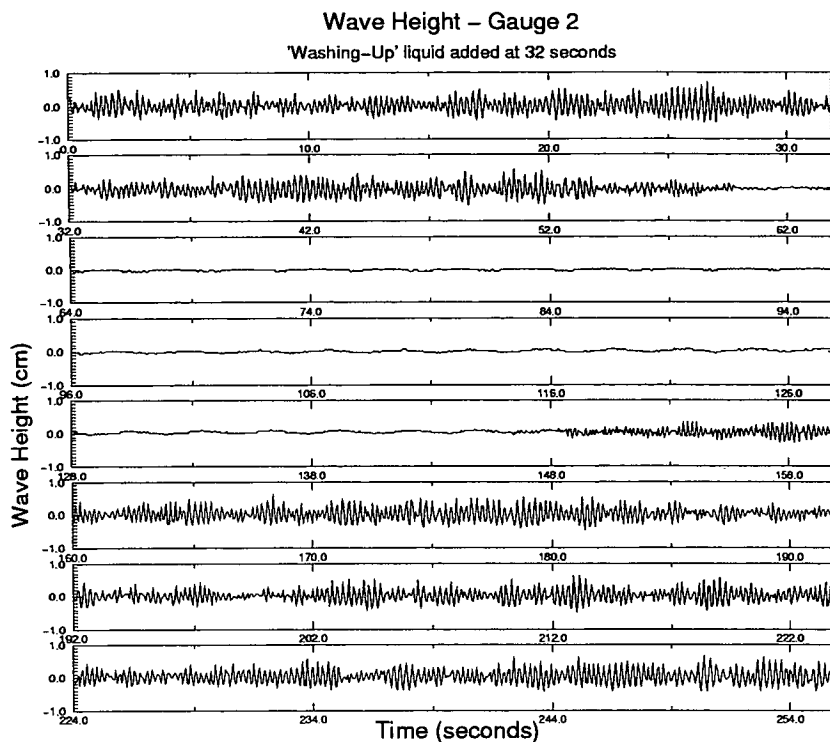


Figure 5.24: 4 Minute record of wave amplitude at Gauge 2

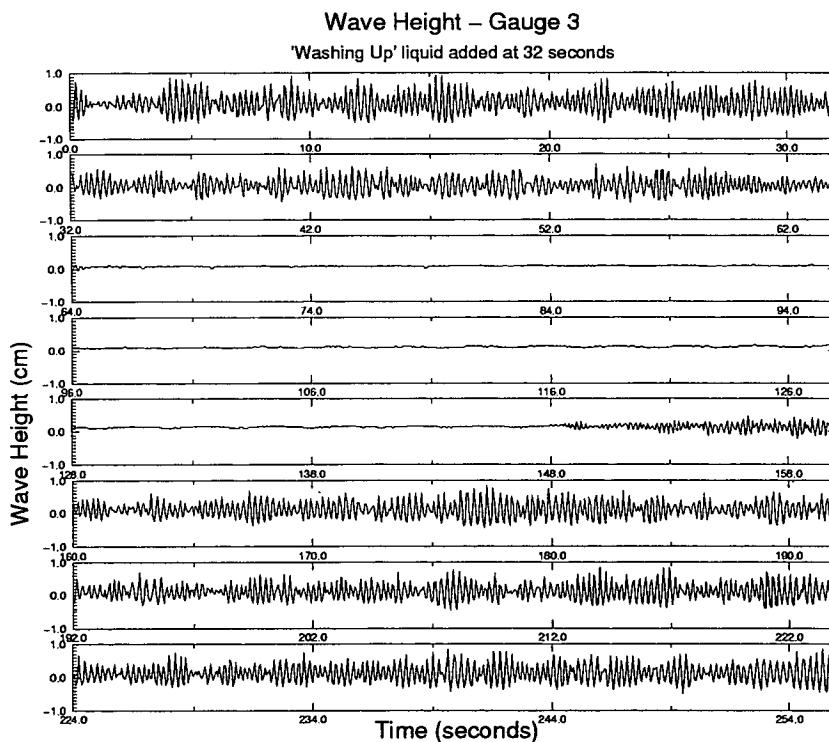


Figure 5.25: 4 Minute record of wave amplitude at Gauge 3

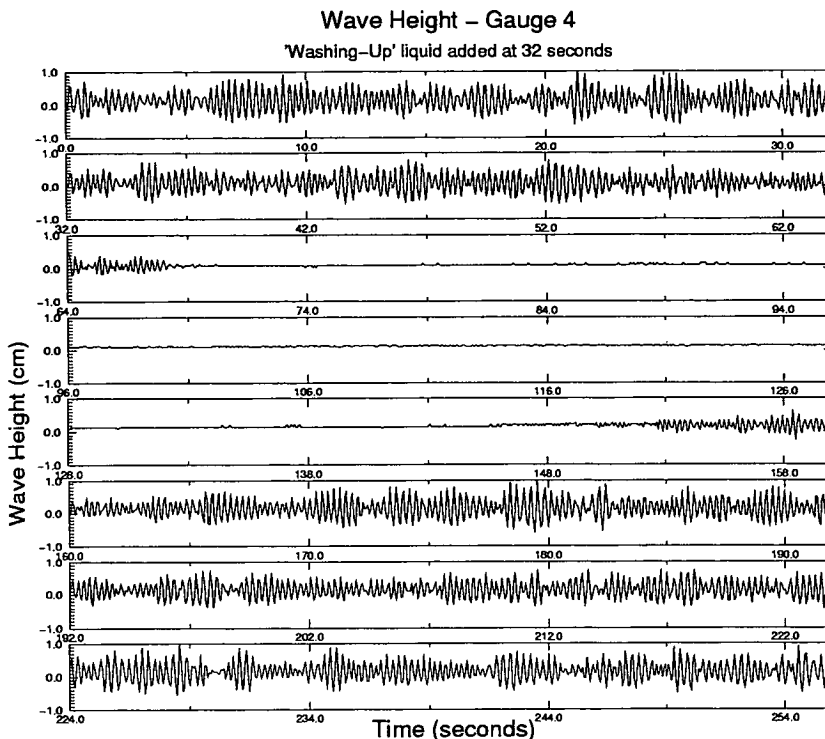


Figure 5.26: 4 Minute record of wave amplitude at Gauge 4

only a strong drop-off in maximum wave amplitude as the film actually passes. However, at gauge 4, the reduction begins long before the film reaches the gauge. The waves present at gauge 4 are actually a superposition of many smaller waves which have interacted, grown and propagated downwind. As the film advances, the area of non-film covered water in which these waves are generated, decreases. Thus the number of waves contributing to the total wave height measured at the gauge drops. The graph was obtained by looking backwards from the film covered section to find the maximum wave amplitude. The value only changes when a greater amplitude than the current maximum is found. To account for the ambiguity in the trace from the 4th gauge when it falls within the trace from the 3rd gauge it has to be remembered that the waves are random and while we would expect a larger wave at the 4th gauge, it just never actually

Damping of Maximum Wave Amplitude

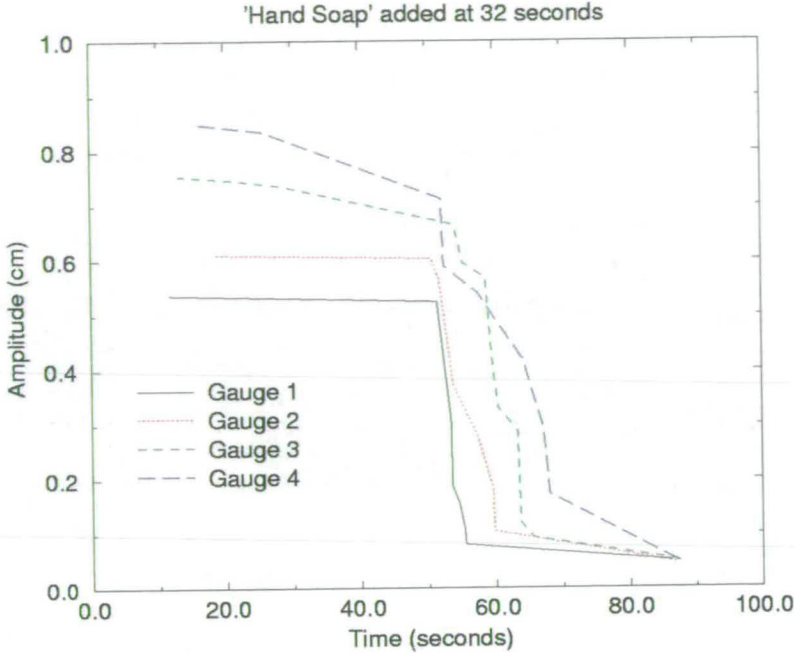


Figure 5.27: Damping of Maximum Wave Amplitude

appeared. If we had managed to take a number of runs and average them, this random fluctuation would not be present.

- The picture is very different if we analyse the growth of maximum wave amplitude once the effect of the film diminishes, figure 5.28. Despite the gauges being located 80cm apart, the waves build at virtually the same rate until reaching their maximum value. This is similar to the experimental findings of Kawai [42] who found that the growth rate and frequency of the initial wavelets are independent of fetch and also the theory of Phillips [71] presented earlier.
- The speed at which the film advances can be easily calculated from figure 5.27. The sudden drop-off in wave amplitude indicated when the film actually reached each wave gauge, table 5.2.

Growth of Maximum Wave Amplitude

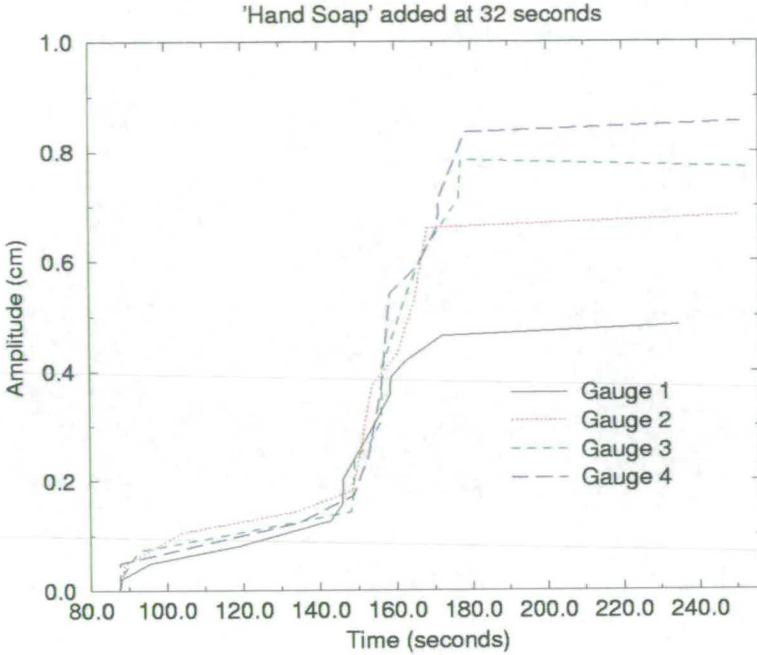


Figure 5.28: Growth of Maximum Wave Amplitude

Gauge	1	2	3	4
Time (s)	56	60	64	68

Table 5.2: Elapsed Time for Film to Reach Gauges

The gauges in this experiment were located 80cm apart which indicates that the front edge of the film (and indeed the entire surface layer) was advancing at 20cm s^{-1} . This is in good agreement with the results obtained from the PIV measurements above and the theoretical calculation of surface drift velocity. The value calculated here is slightly greater than that indicated by the PIV measurements, figure 5.22. However, as can be seen, there is an exceptionally strong velocity gradient near the surface and PIV bias tends to favour the lower velocity components as noted earlier in section 3.3.8.

Fourier Transforming small sub-sections of the entire trace indicates how the frequency spectrum of the waves change as film spreads and diminishes. Locating

the maximum, or peak, frequency component, figures 5.29 5.30, we can observe certain features as the film enters and leaves the measurement zones:

- The shorter the fetch, the higher the peak frequency component. This is consistent with the the arguments given above.
- Before the film is added, the traces are virtually level, indicating that the waves are in a state of equilibrium.
- There is virtually no change in the spectral components of the waves nearest the intake before the film reaches the gauge. While further downwind, the effect of the film is noticeable long before it actually reaches the gauge. The loss of wavelets upwind, prevents the generation of the lower frequency waves, and thus the dominant frequency increases.
- As the effect of the film wears off, waves begin almost uniformly over the entire tank. Initially only high frequency waves are present until the lower frequency waves build and propagate downwind. Although it is expected that the dominant frequency of the initial wavelets should be the same at all gauges, the difference is probably due to the finite width of the running Fourier Transform routine.
- Once the effect of the film has completely passed, the dominant frequency falls back to its original value.

5.5 Effect of surface films in the surf zone

This study is to be extended in the near future to the study of surface films in the surf zone. The addition of a beach section to the wind-wave flume and the use of Laser Induced Fluorescence (LIF) will provide quantitative results relating to

Effect of film on Frequency Spectrum

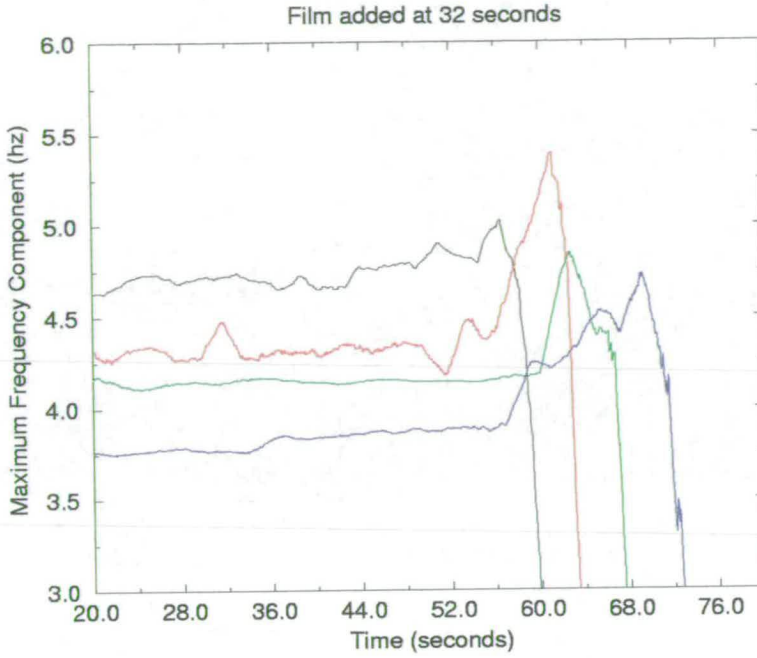


Figure 5.29: Peak spectral component as film enters measurement zones

Effect of film on Frequency Spectrum

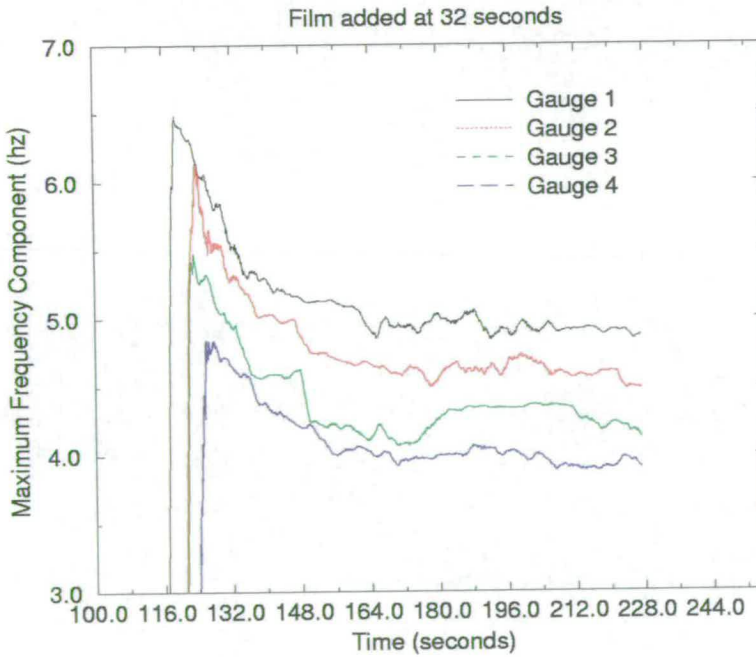


Figure 5.30: Peak spectral component as film leaves measurement zones

Chapter 5 — Results 1 - Effect of Surface Films on Wind Generated Waves

mixing rates of surface films into the water column under the presence of breaking waves.

Chapter 6

Results 2 - Effect of Surface Films on Small Paddle Generated Waves

6.1 Summary

A series of experiments was performed in the Mini-Tank facility (described in section 2.3) to observe and measure the effect of surface active films on small mechanically-generated waves. Measurements of wave damping by surface films and alteration to surface particle trajectories were found to be in good agreement with theoretical predictions. Additionally, experimental evidence verified the theory that the surface is compressed and dilated by wave motion.

6.2 DPIV Measurements of wave damping

In order to quantitatively measure the damping effect of a surfactant it was necessary to use a more controllable environment than the wind-wave facility. The Mini Tank, operating with the weir in place, was used to generate regular, 2-dimensional, waves of a similar frequency to those observed in the wind-wave tank. The weir provided a slight shear layer to mimic the wind-induced surface drift.

A similar PIV system to that used previously was used to measure the velocity field beneath the small paddle generated waves. The camera parameters are given in table 6.1. The camera was located 60cm from the weir with the paddle operating at 3.1Hz, as measured by a light gate and digital oscilloscope.

Camera	2 × Pulnix 9701
Vertical Resolution	484 pixels
Horizontal Resolution	768 pixels
Lens	Nikkor 50mm 1:1.4
f number	2
pixels/particle	2-3
Δt	0.0052631579s

Table 6.1: Experimental Parameters

Initially the shear profile was measured. This and all the results presented below were calculated by averaging the vectors obtained from 40 individual images. A single RMS value of both vertical and horizontal velocity was obtained for each vertical interrogation area (depth), averaged over all 80 horizontal interrogation areas (*i.e.* each point is the average of 320 independent values).

The shear profile, presented in figure 6.1, is essentially the same as the wind-induced drift, though it was not possible to generate quite such a strong velocity gradient at the surface. The little vertical component present, is simply the general tank turbulence which, as indicated, is constant with depth.

Images of the initially film-free water surface were acquired before a single drop of "Hand Soap"¹ was added to the tank, upstream of the measurement zone. The experiment was repeated a short time later with two drops of the same surfactant.

Figures 6.2 is a typical image with its related velocity vector map 6.3.

Measurement of the horizontal velocity profile, figure 6.4, reveals the expected

¹See Appendix A

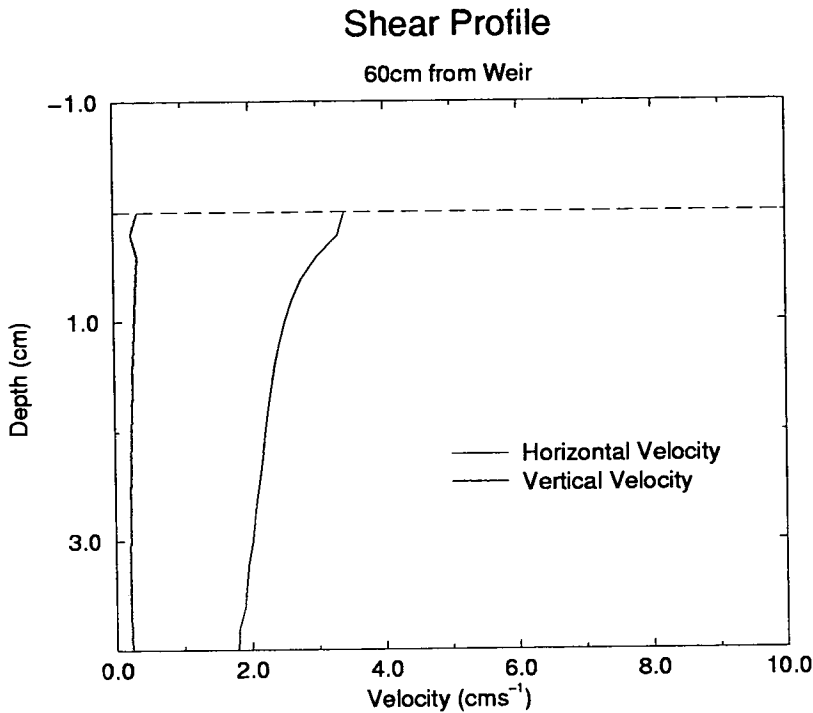


Figure 6.1: Shear Profile

exponential drop off with depth, modified slightly by the shear profile. The damping effect of the surfactant is seen to increase with concentration. The 40 images for each case were obtained in the shortest possible time. Noting from equation 5.3 that the maximum horizontal velocity is given by:

$$u_{max} = amplitude \times 2 \times \pi \times f \quad (6.1)$$

we obtain a value for u_{max} of around $18cms^{-1}$ for these 1cm high 3.1Hz waves. Remembering that the maximum horizontal velocity occurs at the peak of the wave (*i.e.* above the SWL), the results presented in the figure are in good agreement with the theory.

The exponential decrease with depth is also clearly evident in the vertical velocity profile, figure 6.5. The lower vertical velocity values are nearly identical

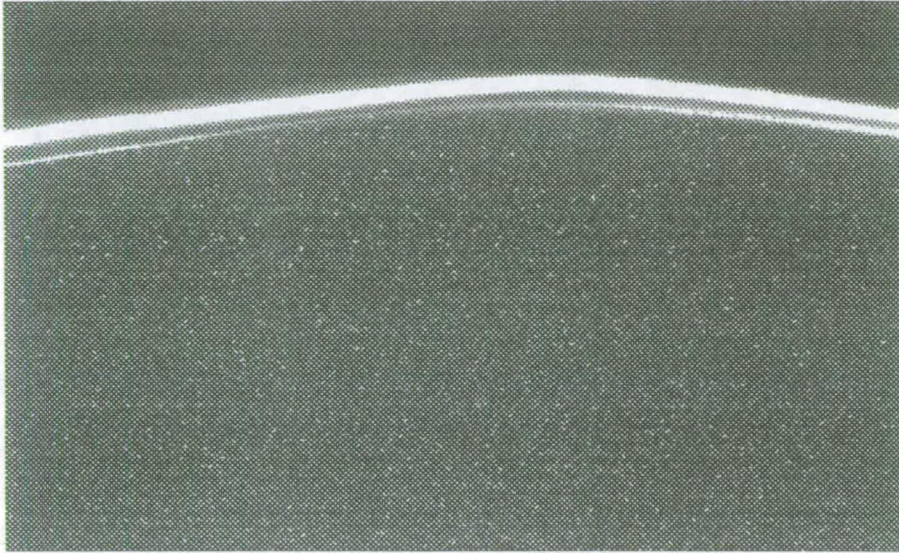


Figure 6.2: Typical PIV Image

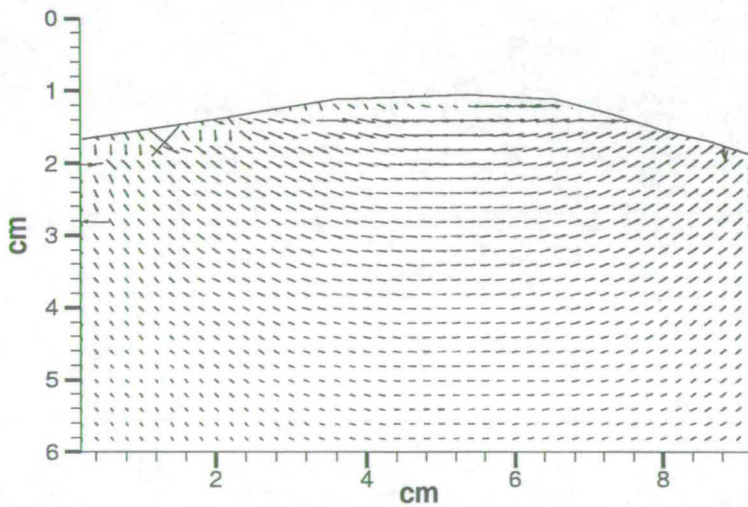


Figure 6.3: Typical Velocity Vector Map

to the horizontal ones once the shear component has been removed. What little difference remains is due to the averaging procedure. The images were all acquired

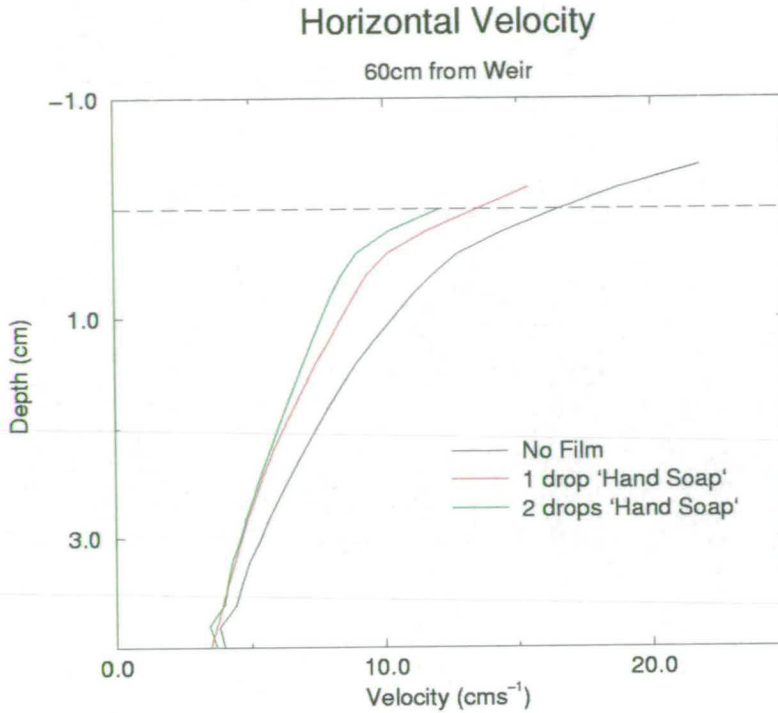


Figure 6.4: Damping of Horizontal Velocity by Film

with the crest of the wave close to the centre of the frame. This is the point at which the horizontal velocity is greatest and the vertical velocity least. Thus the calculated mean vertical velocity is biased towards lower values. However, it is the relative change in velocity which is important, and as clearly demonstrated in these experimental results, the presence of a surfactant does indeed lead to wave damping in capillary-gravity waves.

6.3 Surface particle trajectory measurements

Lucassen-Reynders and Lucassen [59] predicted that the presence of a surface active film would alter particle trajectories from circular to elliptical motion. Additionally, at the inextensible film limit, only vertical motion can be supported. To test these assumptions, a variant of the PIV technique was used in the Mini-Tank. The weir was removed and replaced with foam wedges to minimise surface

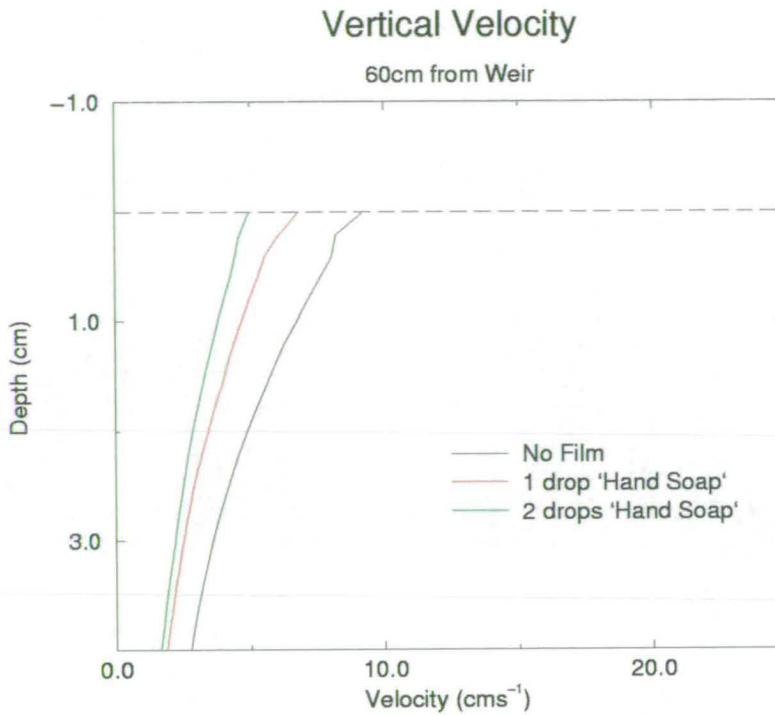


Figure 6.5: Damping of Vertical Velocity by Film

drift, which would disturb the trajectories. A higher resolution CCD camera which was capable of long exposure images was used in the same location as previous experiments. Apart from this, exactly the same equipment (e.g. laser, scanning beam system, etc.) was used as for conventional PIV experiments. The experimental parameters are given in table 6.2. Great care had to be taken to seed the fluid as it was essential to be able to distinguish individual particles. Also, as the films under study initially spread, they take with them most of the surface seeding particles, leaving the surface very sparsely seeded. This can to some extent be avoided by mixing the surface film with seeding particles prior to application.

The scanning beam system enabled multiple images of seeding particles to be captured to a single frame, figure 6.6. In the presence of a surfactant (Hand Soap) the surface particles do indeed move in elliptical paths. However those below the

Camera	Kodak ES1.0
Vertical Resolution	1024 pixels
Horizontal Resolution	1024 pixels
Lens	Nikkor 50mm 1:1.4
f number	4
pixels/particle	3-4
Δt	0.0078125s
Exposure	0.42s

Table 6.2: Experimental Parameters

surface continue to move with circular motion. A number of images were obtained and analysed with the ellipse fitting software described in section 4.4. The points were selected around the ellipse in accordance with the recommendations presented in section 4.4.5.

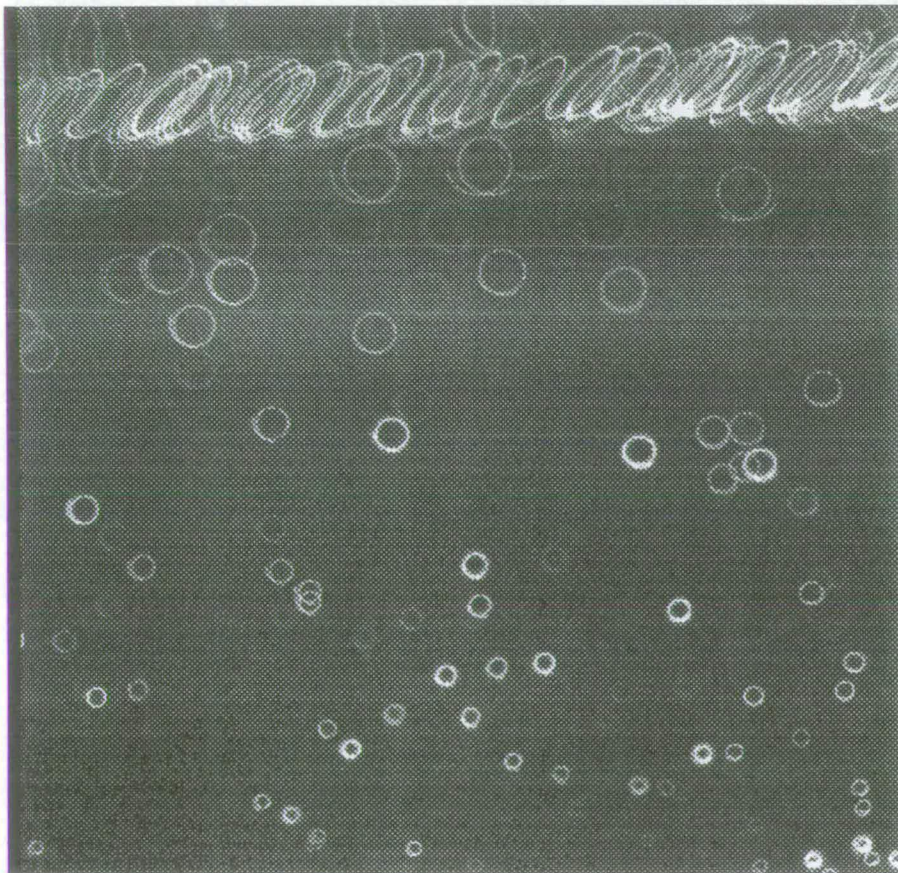


Figure 6.6: Surface and Sub-Surface Particle Trajectories - Hand Soap

Thirty images for three different concentrations of soap and one of mineral oil were analysed. The results are presented in table 6.3. The most important parameters are the ratio of the major to the minor axis ($r1:r2$) and the angle of the ellipse from the vertical. The ideal case of a clean surface, and a schematic representation of the mean ellipse for each case are presented for reference. Several points can be noted from the results:

- The angle of the ellipse from the vertical is dependent on film type and concentration
- As the film concentration increases so too does the ratio of the major to the minor axis of the ellipse. This indicates a phase shift between the horizontal and vertical velocity components, consistent with the theories presented earlier.
- Different films appear to behave in different manners. The calculated ratio for the mineral oil is similar to that of the 3rd soap case, though the angle of the ellipse is quite different. This must be related to the physical chemistry of the film.

The relatively high standard deviation in the results arises from the fact that the particle trajectories are not perfect ellipses. The variation of horizontal velocity with depth, due to the surface shear, leads to the ellipses being open-ended with particles not returning to their original starting position. Again with reference to equation 5.3, the magnitude of the velocity decreases with depth. Thus the particle moves at a slightly greater velocity at the peak than in the trough and in general will not return to its original location but drift slightly in the direction of propagation of the waves, figure 6.7.

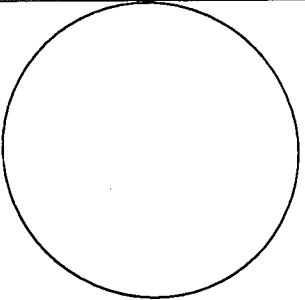
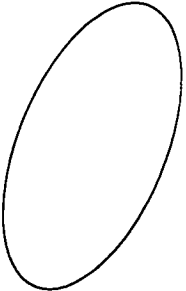
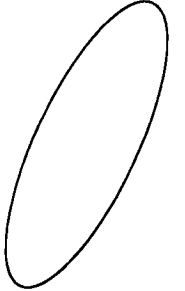
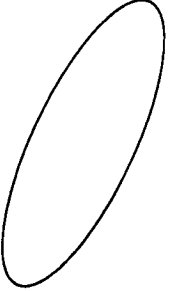
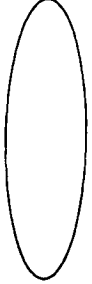
Surface	Clean	1 drop soap	2 drops soap	3 drops soap	Mineral Oil
Ratio r1:r2	1	1.837	3.136	3.317	3.471
Std deviation	-	0.131	0.336	0.285	0.454
Theta (rad)	-	0.410	0.459	0.497	0.028
Std deviation	-	0.08	0.026	0.059	0.040
Schematic					

Table 6.3: Ellipse Parameters for various conditions

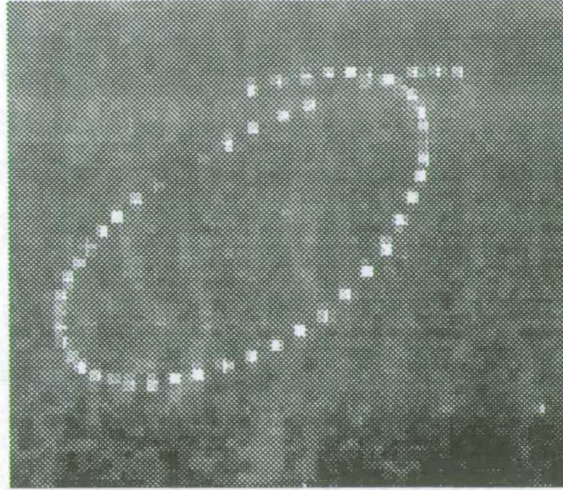


Figure 6.7: Particles often do not return to their original starting point

Figures 6.8 to 6.11 detail an actual image of the surface particle trajectories for each case. For comparison, *Cling Film* was also placed on the water surface to represent an inextensible film. Unfortunately, in the latter case it was very difficult to observe the motion due to reflected light from the cling film, figure 6.12.

In all cases, the particles were observed visually to be moving in a clockwise sense, which is consistent with a wave traveling from left to right. The method of image capture, that of multiple images on a single frame make it difficult to record this. The use of a high speed digital camera and multiple image capture may make it possible to record each particle image to a separate frame, from which the sense of rotation could be inferred.

The ellipse fitting routine was also used to calculate the maximum horizontal displacement of particles on and below the surface for a soap covered and inextensible film to verify the theoretical model of Dorrestein [74] presented in chapter 1.² A fitted exponential again indicates that the amplitude of the motion does

²Although these results represent maximum horizontal displacement and those of Dorrestein represent maximum horizontal velocity, the two are linearly related

indeed decrease exponentially with depth, figure 6.13.

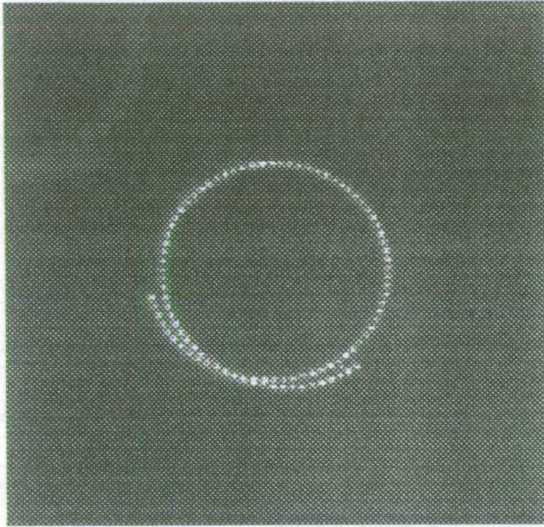


Figure 6.8: Clean Water - clockwise rotation

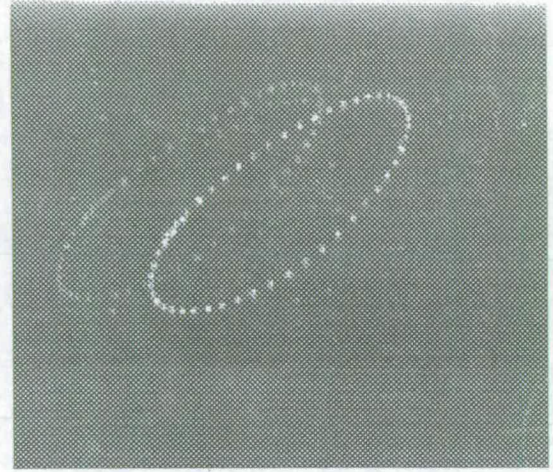


Figure 6.9: Soap - clockwise rotation

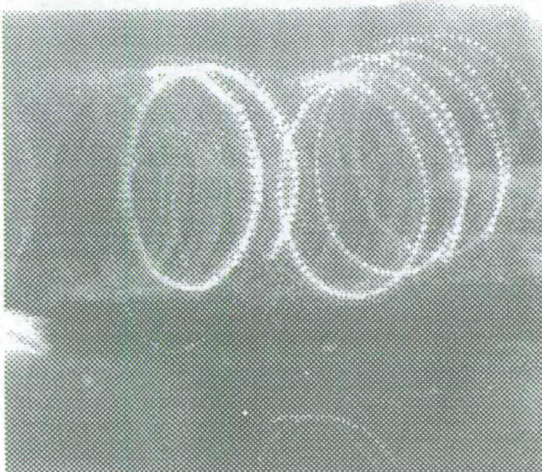


Figure 6.10: Light Oil

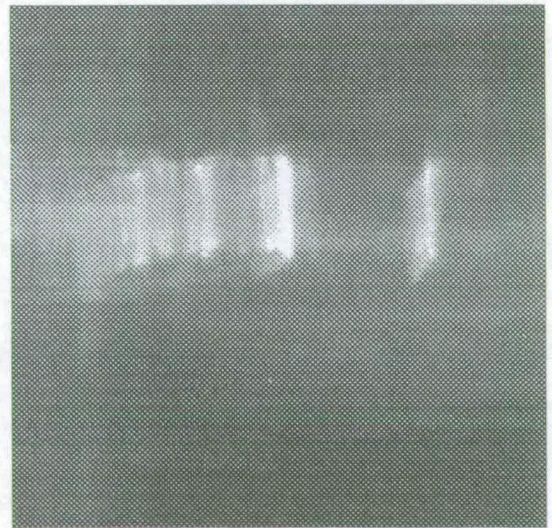


Figure 6.11: Cling film

6.4 Effect of wave motion on surface tension

In order to test the hypothesis that a surface is compressed and dilated by wave motion [28, 39], the camera was moved such that it could observe both the top

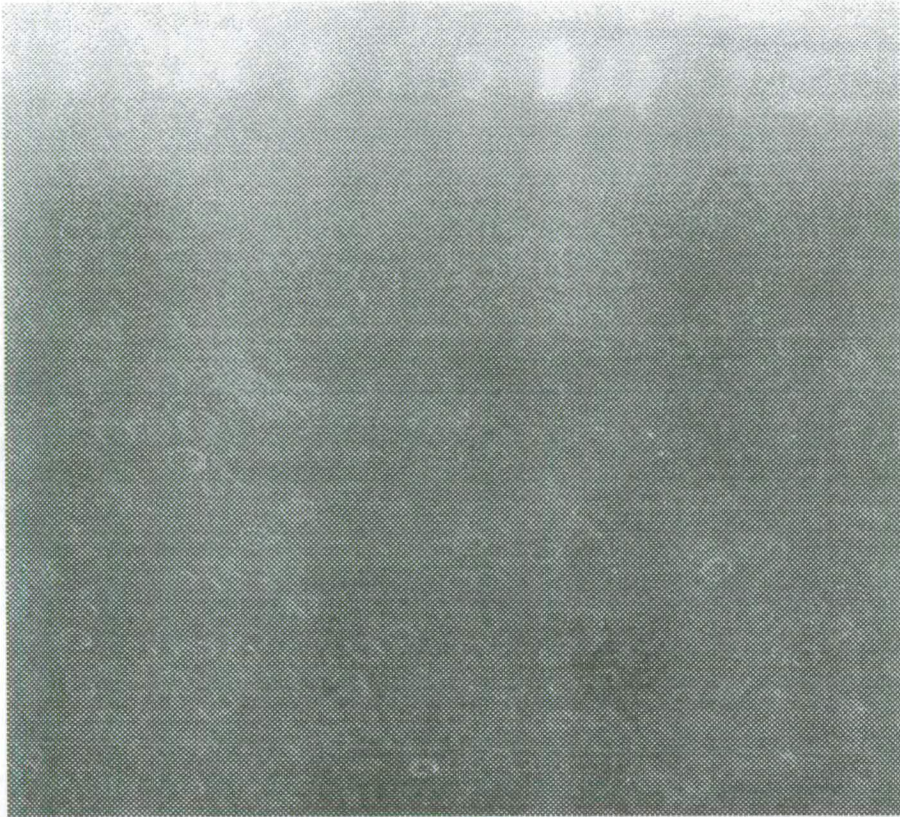


Figure 6.12: Surface and Sub-Surface Particle Trajectories - Inextensible Film

surface and side of the tank. Placing small drops of oil on the surface of the water it was possible to measure their size (of the order of 1-10mm) and the relative wave amplitude (of the order of 1cm), figures 6.14 and 6.15.

Figure 6.16 is the results of measuring the diameter of one particular oil drop in a series of these images. The amplitude of the wave has been offset to appear on the same graph. A sinusoid based on the frequency of the waves has been plotted through both sets of points (the dotted lines). There are three interesting features of this graph: Firstly, the drop does not compress quite sinusoidally. Secondly, there is a very slight phase shift between the response of the drop to the wave motion. Finally, these images verify the statement of Davies and Vose [10], "In general, the surface tends to contract at a wave crest and expand at a trough".

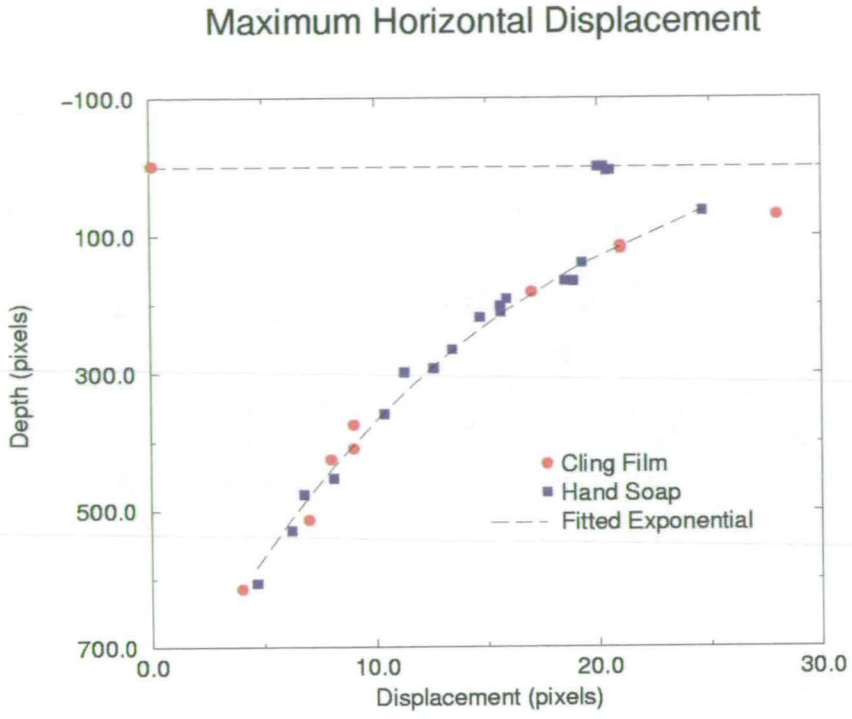


Figure 6.13: Maximum Horizontal Displacement

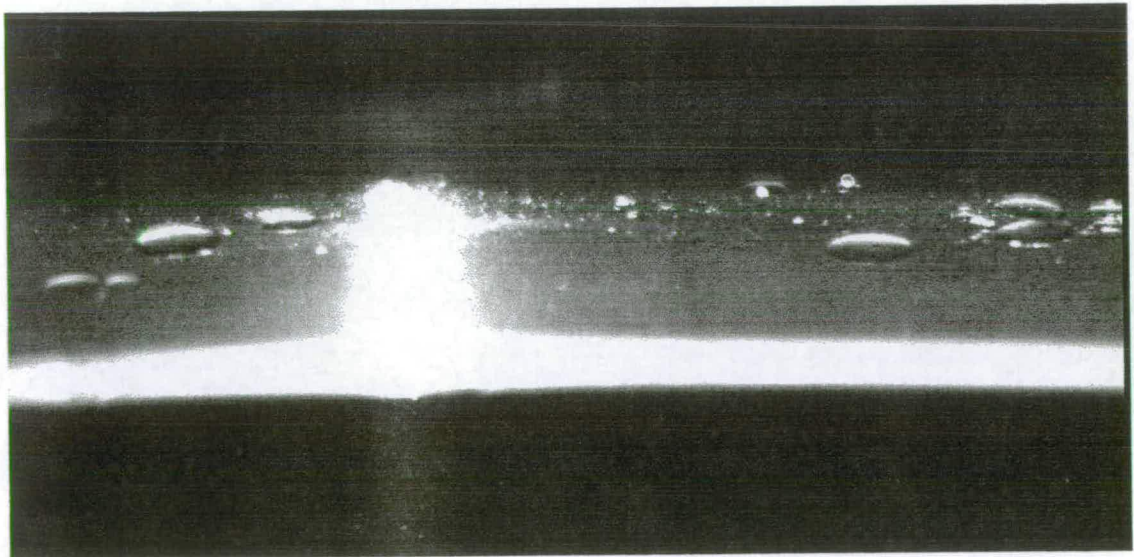


Figure 6.14: Oil drop at wave crest

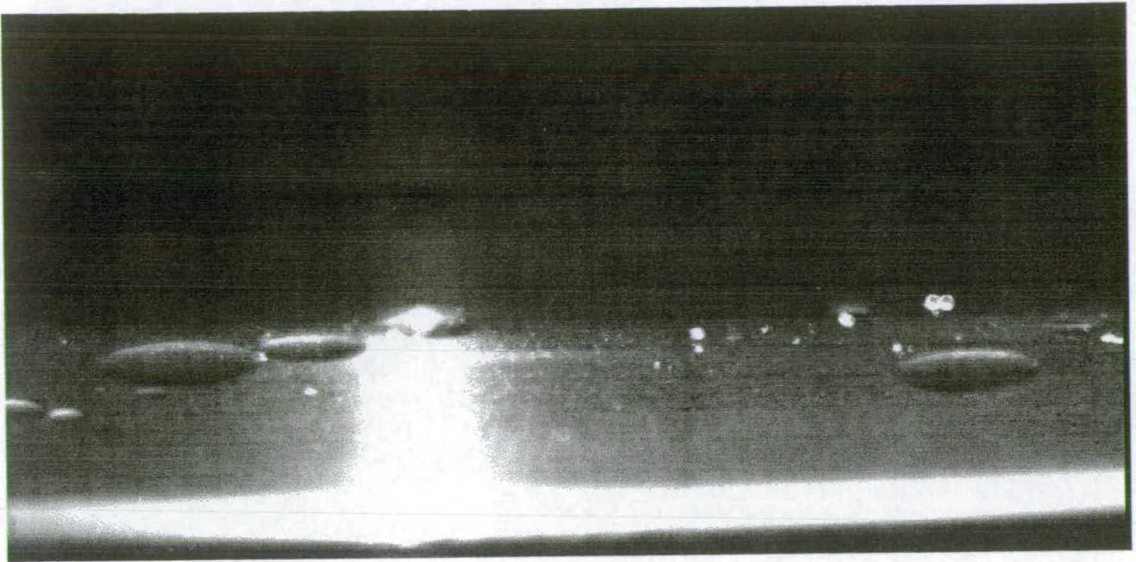


Figure 6.15: Oil drop at wave trough

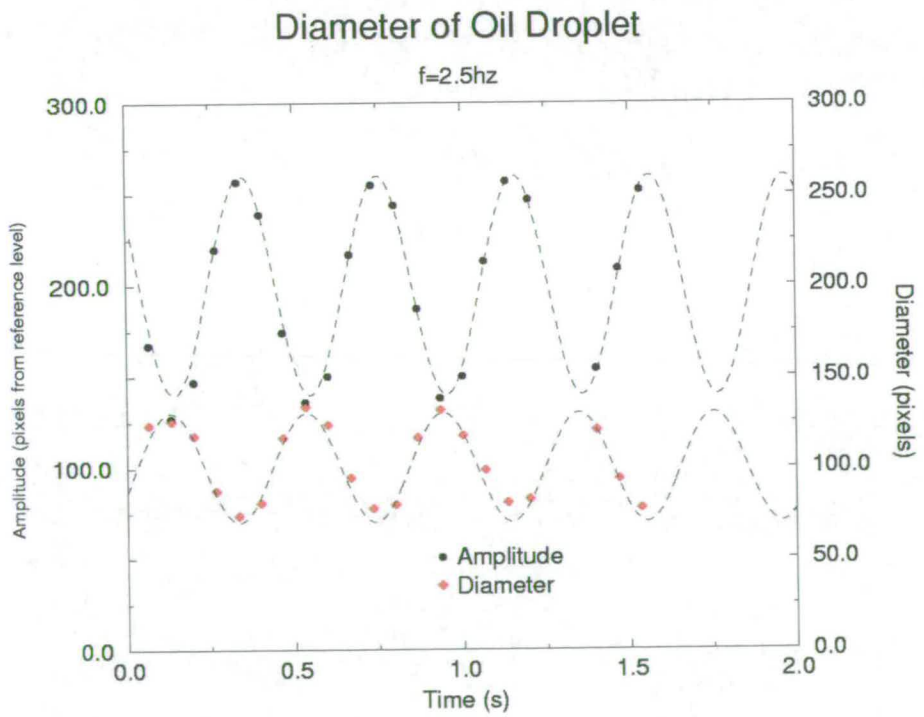


Figure 6.16: Change in oil drop diameter

Chapter 7

Conclusions

7.1 Summary of Main Results

- Two custom made facilities for the study of surface active films on the mechanics of waves were designed and constructed. The wind-wave flume provides a facility for the generation and quantitative observation of wind induced waves. The Mini tank provides a controlled environment for measurement of the damping effect of surface active films.
- A Particle tracking routine was implemented based on the Randomised Hough Transform to fit ellipses to the trajectories of surface particles.
- Many research establishments have made numerous wavegauge and LDA measurements of wind-waves. The author was able to demonstrate that a novel, 2 camera, crosscorrelation DPIV system was capable of reliably obtaining both surface and subsurface velocity profiles beneath wind-waves. These indicated the depth to which the wind-induced turbulence penetrated the bulk and that on average, the waves obeyed the theory of deep-wave propagation.
- The 2 camera system was also utilised to obtain subsurface velocity profiles beneath a contaminated surface with a wind induced surface shear.

Although there are many numerical models, based on the 1998 Euromech Conference¹ the author believes these to be the first actual full-field experimental results. Velocity profiles at various points downwind and the alteration of the profile with time (from before application to the fully damped case) are presented.

- DPIV measurements of surfactant covered, mechanically generated waves provided quantitative evidence that damping is not only confined to capillary waves. Additionally, measurements of surface particle trajectories in the presence of surface active films verified many published theoretical concepts. To the authors knowledge, images of these elliptical trajectories have not be obtained before, let alone measured.

7.2 Suggestions for Future Work

- **PIV and Particle Tracking**

The next logical step for the analysis routines described in this work is to bring them together and to automate more of the stages. The resolution advantages of a combined PIV-Particle Tracking routine have been discussed earlier. Apart from the additional programming required, there is no reason why the ellipse fitting routine could not also be fully automated. Each particle in the image would first need to be identified. The ellipse fitting routine would take 12 of these points at random to which an ellipse would be fitted. Points from different ellipses would generate random parameters while those from the same ellipse would generate similar parameters. Thus *all* the ellipses (and circles beneath the surface) present in a image could

¹See Appendix B

be identified. This would greatly speed up the process enabling far more films to be studied.

The mid term goal of PIV systems should be to bring the individual hardware components together. There are obvious benefits in having a single computer controlling illumination, image triggering and acquisition and input from external sensors such as wavegauges. This process is well underway as digital frame grabbing cards become available with additional inputs/outputs.

Obviously the final step for PIV is an affordable real-time system. The ability to obtain vector maps instantly would greatly aid the setting up of experiments and save considerable time.

- **Surface Films**

It is desirable to obtain elastic properties of the film from measurement of the ellipses. In this way, the film under investigation could be identified, possibly remotely. There are two ways of achieving this goal:

Firstly, as suggested at the 1998 Euromech 387 meeting² a list of surface active films for use in field and laboratory experiments should be agreed upon to enable results from different research establishments to be more easily compared. Now that all the necessary equipment has been designed and proven to give reliable results, a research program should be undertaken to characterise a variety of different surface active films, including the effects of film concentration and wave frequency. In this way, a database of film properties could be constructed from which the elastic properties could be

²See Appendix B

inferred from the elliptical geometry.

Another method would be to use the phase and amplitude information contained in the ellipse geometry to directly obtain the elastic parameters. This would be the reverse of the method used to generate the simulated images in figure 1.7. However the equations are non-linear and the necessary numerical calculations were beyond the scope of this particular study.

To prove that the observed shear is indeed wind-induced and not the inertial effect of the film spreading, further work should be undertaken to introduce the film at different locations within the tank, and to observe the time development of the shear profile.

Further work could be undertaken to investigate breaking waves. Mariners believed that the pouring of oils at sea prevented waves breaking on their ships. The PIV system has been well tested with breaking waves and this would seem an obvious extension of this work.

The experiment with the *Cling Film* needs to be refined to produce quantitative results. Many theoretical and computer models use the inextensible limit and the results could be easily compared. Such an experiment would require some method to overcome wrinkles in the film and the effect of the film itself being illuminated by the laser. The use of fluorescent seeding and a colour filter in the camera would help to remove the later effect.

Appendix A

Chemical Constituents of Chemical Films

The hand soap used in the experiments was **Dymaperl Amber** which is a 27% active solution of sodium lauryl(3 mole) ether sulphate based on a synthetic alcohol. A sample of drops were measured and found to be $22 \pm 2\mu l$. It is available from:

Dymachem Ltd
Malbern Ind Est
Greg Street
South Reddish
Stockport Cheshire
UK
Tel: 0161 476 3607
Fax: 0161 476 3608

The mineral oil used in the experiments was **3-in-1** oil which is available from:

E.R. Howard Ltd
Hull
UK

Appendix B

Papers Published & Conferences Attended

The following papers have been either published in journals or presented at conferences during the course of my Ph.D. studies.

Journals

- Arnott, A, Dewhurst, TP, Pullen, J, Greated, CA (1996) "Underwater CCD Cameras for PIV Flow Mapping" *Journal of Optical and Laser Technology* Vol. 29, No. 1, pp45-50

Conferences

- Pullen, J (1998) "Digital Particle Image Velocimetry applied to the study of Surface Active Films on the mechanics of capillary-gravity waves" *Euro-mech 387*, , Coventry, April 6-9, 1998
- Pullen, J (1997) "Effect of Surface Films on Capillary Waves" *Proc. 7th Int. Offshore and Polar Engineering Conference*, , Honolulu, USA, May 25-29, 1997
- Pullen, J (1996) "Effect of Surface Films on Kinematics of Capillary Waves"

Appendix B — Papers Published & Conferences Attended

ERCRAFTAC Special Interest Group on Wind over Wave Couplings, London, UK, June 26th, 1996

- Arnott, A, Dewhurst, TP, Pullen, J, Greated, CA (1996) "Underwater CCD Cameras for PIV Flow Mapping" *Underwater Optics: Light in the Sea I*, Kettering, UK, February 1995

Bibliography

- [1] R.J. Adrian. Scattering particle characteristics and their effect on pulsed laser measurements of fluid flow: speckle velocimetry versus particle image velocimetry. *Applied Optics*, 23(11):1690, 1984.
- [2] R.J. Adrian. Dynamic ranges of velocity and spatial resolution of particle image velocimetry. *Measurement Science Technology*, 8:1393–1398, 1997.
- [3] P. Bradshaw. Simple wind tunnel design. Technical Report GC98, National Physical Laboratory, 1968.
- [4] P. Bradshaw and R.C. Pankhurst. The design of low-speed wind tunnels. Technical Report 1039, National Physical Laboratory, 1962.
- [5] C.H. Brucker. Digital particle image velocimetry (dpiv) in a scanning light sheet: 3d starting flow around a short cylinder. *Experiments in Fluids*, 19:255–263, 1995.
- [6] R.W. Burling. *Wind Generation of waves on water*. PhD thesis, Imperial College London, 1955.
- [7] H. Capart, H.H. Liu, X. Van Crombrughe, and D.L. Young. Digital imaging characterization of the kinematics of water-sediment interaction. *Water, Air and Soil Pollution*, 99:173–177, 1997.

Bibliography

- [8] E.A. Cowen and S.G. Monismith. A hybrid digital particle tracking velocimetry technique. *Experiments in Fluids*, 22:199–211, 1997.
- [9] D.B. Creamer and J.A. Wright. Surface films and wind wave growth. *Journal of Geophysical Research*, 97(C4):5521–5529, 1992.
- [10] J.T. Davies and R.W. Vose. On the damping of capillary waves by surface films. *Proc. Royal Society London, Series A*, 286:218–234, 1965.
- [11] T.P. Dewhurst. *Multiple CCD Array Digital Particle Image Velocimetry*. PhD thesis, The University of Edinburgh, 1998.
- [12] T.P. Dewhurst. Private communication regarding PIV, 1998.
- [13] T.P. Dewhurst, M.L. Jackobsen, and C.A. Greated. Multiple camera DPIV for force and acceleration measurement in high speed flows. *In Proc. IMechE Optical Methods and Data Processing in Heat and Fluid Flows*, pages 251–258, 1996.
- [14] M. Donelan, M. Skafel, H. Graber, P. Liu, D. Schwab, and S. Venkatesh. On the growth rate of wind-generated waves. *Atmosphere-Ocean*, 30(3):457–478, 1992.
- [15] K. Dysthe and Y. Rabin. Damping of short waves by insoluble surface films. In F. Herr and J. Williams, editors, *ONRL Workshop proceedings. Role of surfactant films on the interfacial properties of the sea surface*, pages 187–213. U.S. Office of Naval Research, London, 1986.
- [16] K. Dysthe, G. Rovner, and Y. Rabin. Damping of capillary waves by polymeric monolayers. comparison with hydrodynamic theory. *Journal of Physical Chemistry*, 90:3894–3895, 1986.

Bibliography

- [17] A.J. Elliot, A.C. Dale, and R. Proctor. Modeling the movement of pollutants in the uk shelf seas. *Marine Pollution Bulletin*, 24(12):614–619, 1992.
- [18] S.A. Ermakov, S.G Salashin, and A.R. Panchenko. Film slicks on the sea surface and some mechanisms for their formation. *Dynamics of Atmospheres and Oceans*, 16:279–304, 1992.
- [19] A.M. Fincham and G.R. Spedding. Low cost, high resolution DPIV for measurement of turbulent flows. *Experiments in fluids*, 23:449–462, 1997.
- [20] C.M. Frank and J.Pullen. Final year project - optical measurement of capillary waves, 1996.
- [21] B. Franklin. Of the stilling of waves by means of oil. *Philosophical Transactions*, 64:445–460, 1774.
- [22] J.C. Gottifredi and G.J. Jameson. The suppression of wind-generated waves by a surface film. *Journal of Fluid Mechanics*, 32:609–618, 1968.
- [23] C. Gray. *The Development of Particle Image Velocimetry for Water wave studies*. PhD thesis, The University of Edinburgh, 1989.
- [24] C. Gray and C.A. Greated. A scanning beam system for two dimensional illumination of fluid flows. *Von Karmen Inst. of Fluid Mechanics Lecture Series*, pages 53–62, 1988-06.
- [25] C. Gray, C.A. Greated, D.R. McCluskey, and W.J Easson. An analysis of the scanning beam PIV illumination system. *Meas. Sci. Technology*, 2:717–724, 1991.
- [26] C.A. Greated. Fluid dynamics for physics students, 1993.

Bibliography

- [27] Y.G. Guezennec, R.S. Brodkey, N. Trigui, and J.C. Kent. Algorithms for fully automated three-dimensional particle tracking velocimetry. *Experiments in Fluids*, 17:209–219, 1994.
- [28] Y. Hardman. Surface tension of wisconsin lake waters. *Transactions of Wisconsin Academy of Sciences, Arts and Letters*, 33:395–404, 1941.
- [29] F. Hering, C. Leue, D. Wierzimok, and B. Jahne. Particle tracking velocimetry beneath water waves. part 1: visualization and tracking algorithms. *Experiments in fluids*, 23:472–482, 1997.
- [30] A. Hind. Private communication regarding fluorescent particles, 1997.
- [31] A. Hirsra, G.M Korenowski, L.M Logory, and C.D. Judd. Determination of surface viscosities by surfactant concentration and velocity field measurements for an insoluble field. *Langmuir. The ACS Journal of Surfaces and Colloids*, 13(14):3813–3822, 1997.
- [32] C-T. Ho and L-H. Chen. A fast ellipse/circle detector using geometric symmetry. *Pattern Recognition Letters*, 28(1):117–124, 1995.
- [33] P.V.C. Hough. Method and means for recognising complex patterns. Technical Report 3069654, U.S. Patent Office, 1962.
- [34] E.L. Houghton and N.B. Carruthers. *Aerodynamics for Engineering Students*. Edward Arnold, 1986.
- [35] H. Huang, D. Dabiri, and M Gharib. On errors of digital particle image velocimetry. *Measurement Science Technology*, 8:1417–1426, 1997.
- [36] H. Huhnerfuss and W. Alpers. The molecular structure of the system water/monomolecular surface film and its influence on water waves. In

Bibliography

- L. Frank and J. Williams, editors, *ONRL Workshop proceedings. Role of surfactant films on the interfacial properties of the sea surface*, pages 121–157. U.S. Office of Naval Research, London, 1986.
- [37] H. Huhnerfuss, W. Alpers, H. Dannhauer, M. Gade, P.A. Lange, V. Neumann, and V. Wismann. Natural and man-made sea slicks in the North Sea investigated by a helicopter-borne 5-frequency radar scatterometer. *Int. Journal of Remote Sensing*, 17(8):1567–1582, 1996.
- [38] H. Huhnerfuss and W.D. Garrett. Experimental sea slicks: Their practical application and utilization for basic studies of air-sea interaction. *Journal of Geophysical Research*, 86(C1):439–447, 1981.
- [39] H. Huhnerfuss, W. Walter, and G. Kruspe. On the variability of surface tension with mean wind speed. *Journal of Physical Oceanography*, 7:567–571, 1977.
- [40] B. Jahne, J. Klinke, and S. Waas. Imaging of short ocean wind waves: A critical review. *Journal of Optical Society of America*, 11(8):2197–2209, 1994.
- [41] K.K. Kahma and M. Donelan. A laboratory study of the minimum wind speed for wind wave generation. *Journal of fluid Mechanics*, 192:339–364, 1988.
- [42] S. Kawai. Generation of initial wavelets by instability of a coupled shear flow and their evolution to wind waves. *Journal of Fluid Mechanics*, 93:661–703, 1979.
- [43] R.D. Keane and R.J. Adrian. Optimization of particle image velocime-

Bibliography

- ters part 1: Double pulsed systems. *Measurement Science and Technology*, 1:1202–1215, 1990.
- [44] R.D. Keane and R.J. Adrian. Optimization of particle image velocimeters part 2: Multiple pulsed systems. *Measurement Science and Technology*, 2:963–974, 1991.
- [45] R.D. Keane and R.J. Adrian. Theory of crosscorrelation analysis of PIV images. *Applied Science Research*, 49:191–215, 1992.
- [46] R.D. Keane, R.J. Adrian, and Y. Zhang. Super-resolution particle image velocimetry. *Measurement Science Technology*, 6:754–768, 1995.
- [47] J. Kompenhans, M. Raffel, and C. Willert. *Introduction to DPIV*. Preliminary Copy, 1997.
- [48] B. Koyuncu. A laser quadrant detection technique for capillary wave measurement. *Optics and lasers in engineering*, 22:53–64, 1995.
- [49] H. Lamb. *Hydrodynamics*. Cambridge University Press, 1952.
- [50] L.D. Landau and E.M. Lifshitz. *Fluid Mechanics*. Pergamon Press, 1959.
- [51] P. Lange and H. Huhnerfuss. Drift response of monomolecular slicks to wind wave action. *Journal of Physical Oceanography*, 8:142–150, 1978.
- [52] N.J. Lawson, N.A. Halliwell, and J.M. Coupland. Particle image velocimetry: image labeling by use of adaptive optics to modify the point-spread function. *Applied Optics*, 33(19):4241–4247, 1994.
- [53] V.F. Leavers. *Shape detection in Computer vision using the Hough Transform*. Springer-Verlag, London, 1992.

Bibliography

- [54] C.G-Y. Lee, B.J Willoughby, H.S. Ghataure, D. Ramsden, and I.S. Robinson. A towed laser slope meter. *Electronic Engineering in Oceanography*, Conference Publication 394:148–151, 1994.
- [55] V.G. Levich. The damping of waves by surface-active materials. *Zhurnal Eksperimentalnoi i Teoreticheskoi Fiziki*, 10(11):1296–1304, 1940.
- [56] P.S. Liss. The chemistry of near-surface seawater. In L. Frank and J. Williams, editors, *ONRL Workshop proceedings. Role of surfactant films on the interfacial properties of the sea surface*, pages 111–120. U.S. Office of Naval Research, London, 1986.
- [57] S.C. Lubard, J.E. Krimmel, and L.R. Thebaud. Optical image and laser slope meter intercomparisons of high frequency waves. *Journal of Geophysical Research*, 85(C9):4996–5002, 1980.
- [58] J. Lucassen. Effect of surface-active material on damping of gravity waves: A reappraisal. *Journal of Colloid and Interface Science*, 85(1):52–58, 1982.
- [59] E.H. Lucassen-Reynders and J. Lucassen. Properties of capillary waves. *Advances in Colloid Interface Science*, 2:347–395, 1969.
- [60] J. Magnaudet and L. Thais. Orbital rotational motion and turbulence below laboratory wind water waves. *Journal of Geophysical Research*, 100(C1):757–771, 1995.
- [61] R.A. McLaughlin. Randomized Hough Transform: Improved ellipse detection with comparison. Technical Report TR97–01, Centre for intelligent information processing systems, UWA, Australia, 1997.
- [62] A. Melling. Tracer particles and seeding for particle image velocimetry. *Measurement Science Technology*, 8:1406–1416, 1997.

Bibliography

- [63] H. Mitsuyasu and T. Kusaba. Wind waves and wind-generated turbulence in the water. In Y. Toba and H. Mitsuyasu, editors, *The Ocean surface*, pages 389–394. D. Reidel Publishing Company, 1985.
- [64] I. Moore, I. Murphy, M. Rolfe, and J. Smithwick. Hydrodynamic/aerodynamic facility for ship science. Technical report, The University of Southampton, 1994.
- [65] I.G. Morrison. *The hydrodynamic performance of an Oscillating water column wave energy converter*. PhD thesis, The University of Edinburgh, 1995.
- [66] P.S. Nair and Jr A.T. Saunders. Hough Transform based ellipse detection algorithm. *Pattern Recognition Letters*, 17:777–784, 1996.
- [67] J. Nogueira, A. Lecuona, and P.A. Rodriguez. Data validation, false vectors correction and derived magnitudes calculation on PIV data. *Measurement Science Technology*, 8:1493–1501, 1997.
- [68] R. Onstott and C. Rufenach. Shipboard active and passive microwave measurement of ocean surface slicks off the southern Californian coast. *Journal of Geophysical Research*, 97(C4):5315–5323, 1992.
- [69] R.C. Pankhurst and D.W. Holder. *Wind-Tunnel Technique*. Pitman, London, 1965.
- [70] W.L. Peirson. Measurement of surface velocities and shear at a wavy air-water interface using particle image velocimetry. *Experiments in fluids*, 23:427–437, 1997.
- [71] O.M. Phillips. The equilibrium range in the spectrum of wind-generated waves. *Journal of Fluid Mechanics*, 4:426–434, 1958.

Bibliography

- [72] K. Prasad, R.J. Adrian, C.C. Landreth, and P.W. Offutt. Effect of resolution on the speed and accuracy of particle image velocimetry. *Experiments in fluids*, 13:105–116, 1992.
- [73] W.H. Press, S.A. Tevkolsky, W.T. Vetterling, and B.P. Flannery. *Numerical Recipes in C*. Cambridge University Press, Cambridge, 1994.
- [74] Dorrestein R. General linearised theory of the effect of surface films on water ripples. i. *Proc. Academy Science Amsterdam*, 54:260–272, 1951.
- [75] Lord Rayleigh. On the tension of water surfaces, clean and contaminated, investigated by the method of ripples. *Philosophical Magazine*, 30:386–400, 1890.
- [76] M. Schmidt. Experimental investigations on two-phase flow past a sphere using digital particle image velocimetry. *Experiments in Fluids*, 14:296–304, 1993.
- [77] J.C. Scott. The influence of surface-active contamination on the initiation of wind waves. *Journal of Fluid Mechanics*, 56:591–606, 1972.
- [78] J.C. Scott. The historical development of theories of wave-calming using oil. *History of Technology*, 3:163–186, 1978.
- [79] J.C. Scott. *Oil on troubled waters*. Multi Science Publishing Co, 1979.
- [80] J.C. Scott. The propagation of capillary-gravity waves on a clean water surface. *Journal of Fluid Mechanics*, 108:127–131, 1981.
- [81] J.C. Scott. The effect of organic films on water surface motions. In E.C. Monahan and G. MacNiocaill, editors, *Oceanic Whitecaps*, pages 159–165. D. Reidel Publishing Company, 1986.

Bibliography

- [82] J.C. Scott. Surface films in oceanography. In F. Herr and J. Williams, editors, *ONRL Workshop proceedings. Role of surfactant films on the interfacial properties of the sea surface*, pages 19–40. U.S. Office of Naval Research, London, 1986.
- [83] J.C. Scott and M. Bagg. The use of surface-marking films to detect ocean currents. *Int. J. Remote Sensing*, 12(5):827–829, 1991.
- [84] D.J. Skyner. *The Mechanics of Extreme Water Waves*. PhD thesis, The University of Edinburgh, 1992.
- [85] S.M. Soloff, R.J. Adrian, and Z-C. Liu. Distortion compensation for generalised stereoscopic particle image velocimetry. *Measurement Science Technology*, 8:1441–1454, 1997.
- [86] M. Stanislas and J.C. Monnier. Practical aspects of image recording in particle image velocimetry. *Measurement Science Technology*, 8:1427–1440, 1997.
- [87] S. Tang and O.H. Shemdin. Measurement of high frequency waves using a wave follower. *Journal of Geophysical Research*, 88(C14):9832–9840, 1983.
- [88] D.J. Tritton. *Physical Fluid Dynamics*. Oxford University Press, 1988.
- [89] K. van Gastel and P.A.E.M Janssen. On the growth of gravity capillary waves by wind. In Y. Toba and H. Mitsuyasu, editors, *The Ocean surface*, pages 71–75. D. Reidel Publishing Company, 1985.
- [90] J.F. Vesecky and R.G. Johnson. Acoustic and capillary wave sensing of the marine environment. In L. Frank and J. Williams, editors, *ONRL Workshop proceedings. Role of surfactant films on the interfacial properties of the sea surface*, pages 215–244. U.S. Office of Naval Research, London, 1986.

Bibliography

- [91] J. Wang and J. Wu. Wind-induced water turbulence. In Y. Toba and H. Mitsuyasu, editors, *The Ocean surface*, pages 401–406. D. Reidel Publishing Company, 1985.
- [92] J. Westerweel. *Digital particle image velocimetry - Theory and application*. Delft University Press, 1993.
- [93] J. Westerweel. Fundamentals of digital particle image velocimetry. *Measurement Science Technology*, 8:1379–1392, 1997.
- [94] J. Westerweel, D. Darbiri, and M. Gharib. The effect of a discrete window offset on the accuracy of crosscorrelation analysis of digital PIV recordings. *Experiments in Fluids*, 23:20–28, 1997.
- [95] J. Westerweel, A.A. Draad, J.G. Th. van der Hoeven, and J. van Oord. Measurement of fully-developed turbulent pipe flow with digital particle image velocimetry. *Experiments in Fluids*, 20:165–177, 1996.
- [96] C. Willert. Stereoscopic digital particle image velocimetry for application in wind tunnel flows. *Measurement Science Technology*, 8:1465–1479, 1997.
- [97] C.E. Willert. High resolution correlation peak detection. Technical Report ECE 251 C, UCSD, 1989.
- [98] C.E. Willert and M. Gharib. Digital particle velocimetry. *Experiments in Fluids*, 10:181–193, 1991.
- [99] Yeh and Cummings. Localised fluid flow measurement with a He-Ne laser spectrometer. *Applied Physics letters*, 4:176–178, 1964.
- [100] H.K. Yuen, J. Illingworth, and J. Kittler. Detecting partially occluded

Appendix B — Bibliography

ellipses using the Randomised Hough Transform. *Image and Vision Computing*, 7(1):31–37, 1989.